Effect of the microstructure and orientation of grains on the performance of perovskite ferroelectric ceramics

Jiangguli Peng

THESE DE DOCTORAT EN COTUTELLE

LE MANS UNIVERSITE

COMUE UNIVERSITE BRETAGNE LOIRE

ECOLE DOCTORALE N° 596

Matière, Molécules, Matériaux

Spécialité : « *Physique* »

Jiangguli PENG

«Effect of the microstructure and orientation of grains on the performance of perovskite ferroelectric ceramics»

Thèse présentée et soutenue à : Institut de Céramiques de Shanghai, Académie des Sciecnes de Chine
Et en Visio Conférence : Institut des Molécules et Matériaux du Mans , Le Mans Université
Date: 27 May 2020
Unité de recherche : Institut des Molécules et Matériaux du Mans
Thèse N: (2020LEMA1013)

Rapporteurs avant soutenance :

Malgorzata MAKOWSKA-JANUSIK, Professeure, Institut de Physique, Université Jan Dlugosz à Czestochowa, Pologne

Jiwei ZHAI, Professeur, École de sciences et l'ingénierie des matériaux, Tongji Université, Shanghai, Chine

Sylvain MARINEL, Professeur, Laboratoire de CRISMAT, Caen-Normandie Université, France

Composition du Jury:

Président :

Examinateurs : **Malgorzata MAKOWSKA-JANUSIK**, Professeure, Université Jan Dlugosz à Czestochowa, Pologne

Jiwei ZHAI, Professeur, Tongji Université, Shanghai, Chine

Sylvain MARINEL, Professeur, Laboratoire CRISMAT, Caen-Normandie Université, France

Haosu LUO, Professeur, Institut de céramique de Shanghai, Académie des sciences, Chine

Jiangtao ZENG, Professeur, Institut de céramique de Shanghai, Académie des sciences, Chine

Co-Dir. de thèse : **Guorong LI**, Professeur, Institut de céramique de Shanghai, Académie des sciences, Chine

Dir. de thèse : **Abdel Hadi KASSIBA**, Professeur, Institut des Molécules et Matériaux du Mans, Le Mans Université, France

Titre: Effet de la microstructure et de l'orientation des grains sur les performance des céramiques ferroélectriques pérovskite

Mots clés: Céramiques Texturées, Propriétés piézoélectriques, Nanodomaines, Dopage « Soft-Hard », Relaxation diélectrique

Résumé: Les matériaux ferroélectriques sont largement utilisés dans d'importantes technologies incluant les transducteurs, actionneurs, capteurs... Parmi les structures ferroélectriques les plus exploitées, celles à base de $Pb(Zr,Ti)O_3$ (PZT) offrent de bonnes performances dans des dispositifs opérationnels. Malgré cet aboutissement en terme de valorisation, la compréhension fondamentale des caractéristiques physiques des systèmes basés sur les céramiques PZT continue de susciter l'intérêt d'une large communauté scientifique. Cependant, un intérêt croissant porte sur la mise en œuvre de structures ferroélectriques exemptes d'éléments chimiques nocifs pour l'environnement dont la teneur en plomb. Dans ce cadre, les systèmes à base de $BiFeO_3$-$BaTiO_3$ (BF-BT) ont suscité beaucoup d'intérêt en tant que matériaux ferroélectriques sans plomb. Ce travail de thèse porte sur des études systématiques portant sur les céramiques à base de PZT et celles à base de BF-BT.

Trois contributions ont été développées doant la première dédiée à l'analyse des microstructures, des phases cristallines et des propriétés ferroélectriques dans les systèmes PZT dopés. Les travaux ont montré le rôle du dopage Soft-Hard sur les propriétés structurales, morphologiques et électriques des matériaux dopés accepteurs. Dans une deuxième partie, l'interaction des microstructures et des propriétés électriques a été étudiée dans les systèmes BF-BT. L'optimisation des conditions de fabrication à travers la composition chimique et le traitement thermique contribue aux propriétés piézoélectriques améliorées dans ces systèmes sans plomb. Pour la troisième partie des travaux, des études expérimentales de fabrication, texturation et les caractérisations des propriétés ferroélectriques et électromécaniques ont été corrélées avec l'organisation structurale et morphologique des céramiques texturées.

Title: Effect of the microstructure and orientation of grains on the performance of perovskite ferroelectric ceramics

Keywords: Textured ceramics, Piezoelectric properties, Nanodomains, Soft-hard doping, Dielectric relaxation

Abstract: Ferroelectric materials have been widely applied in transducers, high-pressure generators, actuators, sensors... In this context, the ferroelectric materials are generally regarded as being related to an important class of smart materials. Among the most popular ferroelectric materials, those based on $Pb(Zr,Ti)O_3$ (PZT) structures show the best performances in operating devices. Despite such achievements, the fundamental understanding of the physical characteristics continues to arouse the interest of a wide scientific community. On the other hand, in view of the environmental-friendly requirement, more attention have been paid by the researchers to lead-free ferroelectric materials. Thus, $BiFeO_3$-$BaTiO_3$ (BF-BT) systems have attracted a great deal of interest as promising candidate for lead-free ferroelectric materials. In this dissertation, PZT-based and BF-BT-based ceramics were investigated systematically.

Three contributions have been developed with the first dealing with the analysis of microstructures, crystalline phases and electric properties in doped PZT systems. It was revealed the involvement of softening-hardening features and the relation between defect dipoles and electric properties in acceptor doped materials. In a second part, the interplay of microstructures and electric properties was studied in BF-BT systems, providing the relevant analysis of the optimized performance such as the enhanced piezoelectric properties of lead-free systems. In the third contribution, experimental methods of synthesis and texturing BF-BT systems by BT templates ad the characterization of ferroelectric and electromechanical properties have been correlated with the structural and morphological organization of textured ceramics.

Acknowledgement

My heartfelt thanks and respect to my supervisors of **Prof. Guorong Li** and **Prof. Abdelhadi Kassiba**, who imparted me the opportunity to study in their group and led me into the piezoelectric field and related interdisciplinary field. I am grateful for their outstanding scientific supervision, kindly support and enthusiastic encouragement in the past years, which consistently inspired my work and improved my working discipline. It has been an honor to become their Ph.D student.

My deep appreciation to **Prof. Jiangtao Zeng**, who gave me consistent scientific guidance, productive assistance and encouragement, which indeed improved my work.

I would like to acknowledge Prof. Liaoying Zheng, Prof. Ronghua Zeng, Prof. Malgorzata Makowska-Janusik, Prof. Jiwei Zhai, Prof. Sylvain Marinel, Prof. Haosu Luo, Associate Prof. Zhenyong Man, Associate Prof. Kunyu Zhao, Associate Prof. Tian Tian, Mr. Xuezheng Ruan, Mr. Caiming Zhong, Ms. Xue Shi, Mr. Wenbin Liu, Ms. Dan Wang. Ms. Honglan Zhou, Mr. Qiuhua Shao, Mr. Sheng Ye for kindly assistance during my scientific study.

I sincerely appreciate Wei Zhao, Yibo Zhou, Xiaoming Chen, Kunqi Xu, HuizhuYu, Zhengping Ding, Zhanchuan Cao, Dan Zhang, Qiwei Lou, Qianying Sun, Jian Zou, Xiao Luo, Jing Shang, Weiwei Li, Zhuo Yu, Wei Li, Xiang Xia, Yusi Huang, Bingjie Teng, Chunbo Li, Xi Chen, Haoxian Chen, Aihua Liang, Dingwei Liu, et al.

Many thanks to my warm-hearted friends Liyang Zheng, Yuzhu Long, XiaoyangYu, Chen Li, Haoran Wang, Karolina Ordon, Drisya, and Halim Wafae who gave me kindly help during my study in France.

My warm thanks to the administrative officers in the department of graduate student, I acknowledge Zhiwei Zhou, Caifei Lu, Xinhong Lu, Xueying Zhao, Peishuai Zhang et al.

Lastly, I sincerely appreciate my **parents** and **brother** for their selfless love and great confidence in me through all these years. A special thanks to my dear husband, **Can Lu**, for all the support in the past and his love for life.

List of publications

[1] Jiangguli Peng, Wenbin Liu, Jiaotao Zeng, Liaoying Zheng, Guorong Li, Anthony Rousseau, Alain Gibaud, Abdelhadi Kassiba. Large electromechanical strain at high temperatures of novel <001> textured $BiFeGaO_3$-$BaTiO_3$ based ceramics. ***Journal of Materials Science & Technology***, 2020, 48: 92-99.

[2] Jiangguli Peng, Jiaotao Zeng, Liaoying Zheng, Guorong Li, Nader Yaacoub, Mohamed Tabellout, Alain Gibaud, Abdelhadi Kassiba. The interplay of phases, structural disorder and dielectric behavior in Al doped $BiFeO_3$-$BaTiO_3$ ceramics. ***Journal of Alloys and Compounds***, 2019, 796: 221-228.

[3] Jiangguli Peng, Jiaotao Zeng, Guorong Li, Liaoying Zheng, Xuezheng Ruan, Xiang Huang, Dan Xhang. Softening-hardening transition of electrical properties for Fe^{3+}-doped $(Pb_{0.94}Sr_{0.05}La_{0.01})(Zr_{0.53}Ti_{0.47})O_3$ piezoelectric ceramics. ***Ceramics International***, 2017, 43: 13233-13239.

[4] Xiang Huang, Jiangguli Peng, Jiangtao Zeng, Liaoying Zheng, Guorong Li, Tomoaki Karaki. The high piezoelectric properties and high temperature stability in Mn doped $Pb(Mg_{0.5}W_{0.5})O_3$-$Pb(Zr,Ti)O_3$ ceramics, ***Ceramics International***, 2019, 45: 6523-6527.

[5] Zhuo Yu, Jiangtao Zeng, Liaoying Zheng, Jiangguli Peng, Guorong Li. Effects of $Ba(Zr_{0.25}Ti_{0.75})O_3$ substituent on ferroelectric properties in the $BiFeO_3$-$PbTiO_3$ high temperature ceramics. ***Ceramics International***, 2018, 44: S65-S68.

[6] Zhuo Yu, Jiangtao Zeng, Abdelhadi Kassiba, Liaoying Zheng, Jiangguli Peng, Guorong Li. Enhanced electrical properties of $BiFeO_3$–$PbTiO_3$ based ceramics with suitable raw material. ***Journal of Materials Science: Materials in Electronics***, 2019, 30: 14500-14507.

Prize and awards

[1] Excellence grant program **EIFFEL** for the annual scholarship for scientific research (2018-2019), Le Mans, France.

[2] The prize for the Outstanding Communist Party Member from University of

Chinese Academy of Sciences (09/2017), China.

[3] The prize for the Merit Student from University of Chinese Academy of Sciences (06/2017), China.

Participation in the conferences

Oral communications:

[1] The structures and properties of the ultra-high temperature-dependent behavior in textured $BiFeGaO_3$-$BaTiO_3$ piezoelectric ceramics. The 9th China-Japan Symposium on Ferroelectric Materials and Their Applications. Chengdu, Sep.14th-18th, 2017.

[2] Synthesis of $BaTiO_3$ templates and piezoelectric properties of textured $BiFeGaO_3$-$BaTiO_3$. Advanced materials graduate academic forum, Dec. 1rt, Shanghai, China.

[3] The interplay of phases, structural disorder and dielectric behavior in Al doped $BiFeO_3$-$BaTiO_3$ ceramics. The 5th Conference of the Serbian Society for Ceramic Materials, Jun. 8th-10th, Belgrade, Serbia, 2019.

Posters:

[1] Synthesis and piezoelectric properties of textured $BiFeGaO_3$-$BaTiO_3$ piezoelectric ceramics. The 10th China International Conference on High-Perforence Ceramics. Nanchang, Nov. 5th-7th, 2017.

[2] The interplay of phases, structural disorder and dielectric behavior in Al doped $BiFeO_3$-$BaTiO_3$ ceramics. JED 2019 Nantes. Jun. 23rd, Nantes, France, 2019.

Abstract

Ferroelectric materials have been widely applied in transducers, high-pressure generators, actuators, sensors... In light of this, the ferroelectric materials are generally regarded as being related to an important class of smart materials.

Among the most popular ferroelectric materials, those based on PZT structures show the best performances in workable devices. From fundamental understanding of physical features in PZT based systems, even many mechanisms have been exhaustively validated, actual studies are still under consideration by a wide scientific community. For instance, the softening-hardening doping processes, the relevance and behavior of defect dipoles impacting dielectric responses as well as their incidence on the piezoelectric properties remain essential concerns in material sciences area. On the other hand, in view of the environmental-friendly requirement, more attention have been paid by the researchers to lead-free ferroelectric materials. $BiFeO_3$-$BaTiO_3$ (BF-BT) systems have attracted a great deal of interest as promising candidate for promising lead-free ferroelectric materials. Due to intrinsic confinements stemming from grain structures of ferroelectric systems, piezoelectric properties cannot be improved substantially even by doping processes. The synthesis of single crystals for can be relevant to enhance the ferroelectric properties but this route is limited for the development at wide scale because of its rigorous synthesis condition and its high cost. Thus, the realization of textured ferroelectric materials offers an alternative approach to achieve highly performant ferroelectric systems. The mechanism is based on the ferroelectric domains being forced to align along a defined direction. Beyond an easy processing, the domain texturing approach is reproducible and lead to reliable properties as it may be achieved by using single crystals.

In this dissertation, PZT-based and BF-BT-based ceramics were investigated systematically. The first contribution was dealing with the analysis of microstructures, crystalline phases and electric properties in PZT systems. It was revealed the involvement of softening-hardening features and the relation between defect dipoles and electric properties in acceptor doped materials. In a second part, the interplay of

microstructures and electric properties was studied in BF-BT systems, providing the relevant analysis of the optimized performance such as the enhanced piezoelectric properties of lead-free systems. In the third contribution, experimental investigations and deep analysis were devoted to the effects of the microstructures, the structuration of the grains by the templated grain growth method in textured BF-BT ceramics and the electrical properties. The main achieved results are hereafter highlighted:

(1) The correlation between the microstructures and the involved properties were investigated in soft $(Pb_{0.94}Sr_{0.05}La_{0.01})(Zr_{0.53}Ti_{0.47})O_3$ (PSLZT) ceramics fabricated by the conventional solid-state reaction and using Fe^{3+} doping to form $PSL(ZT)_{1-x}$-Fe_x system. The variation of the doping rate modulates the ferroelectric features and the electromechanical behavior. With low Fe^{3+} contents below 0.010 wt.%, the samples showed apparent characteristics of soft materials. The remnant polarization of samples is about 35.7 $\mu C/cm^2$ with the piezoelectric constant and the strain of 412 pC/N and 0.22% (25 kV/cm) respectively. With increasing the Fe^{3+} content, the amount of oxygen vacancies increased to keep charge conservation. After aging, defect dipoles were formed as a result of the short-range migration of oxygen vacancies. Ferroelectric domains were pinned by these defect dipoles under suitable electric fields. Thus, the obtained ceramics exhibit the features of hard materials with the low piezoelectric constants and mechanical quality factors Q_m achieving values as high as 500. The microstructures and piezoelectric performances of samples were also affected by the sintering process. By increasing temperatures, the soft-feature sample (x = 0.005) showed more porous grains inducing a low density and a decrease of the piezoelectric coefficient. Moreover, comparative investigations, based on the poled and unpoled samples, point out the influence of defect dipoles on ferroelectric properties of soft and hard samples. It was found that polarization of defect dipoles P_D was aligned along the spontaneous polarization P_S. However, this pinning effect of domains have tendency to be degraded in hard ceramics.

(2) $BiFeAlO_3$-$BaTiO_3$ ceramics with Al doping the B site were systematically investigated with a particular focus on their microstructures and electric properties, in order to optimize the ferroelectric performance. It was found that the distortion of the

rhombohedral phase reached the highest content of doping elements; i.e. x = 0.030. The highest spontaneous and remnant polarization were achieved in this system with the values 36.8 μC/cm^2 and 31.5 μC/cm^2, respectively. The large distortion and high content of the rhombohedral phase played an essential role in the improvement of ferroelectric behavior. ^{57}Fe Mössbauer investigations show an increase of the disorder of Fe^{3+} with higher Al doping ratios, which contribute to pronounced features of a diffuse phase transition. With higher Al doping above 0.045, the samples exhibited two distinct dielectric relaxation behaviors, which were analyzed explained by the "Brick-wall" model.

(3) Textured $BiFeGaO_3$-$BaTiO_3$ (BFG-BT) ceramics were studied for their microstructures and ferroelectric performance via the reactive templated grain growth method. The BFG-BT textured sample exhibited superior high-temperature ferroelectric properties based on the analysis of strain and dielectric properties at different temperatures. The piezoelectric coefficient of the textured sample reached 685 pm/V at 180 ℃. XRD investigations showed a stable ferroelectric structure of textured samples and no phase transition is observed from the ferroelectric phase (*P*4mm and *R*3c) to the paraelectric phase (cubic). The oriented rhombohedral phase and the high-density of nanodomains were revealed to play essential roles in upgrading strains of the textured products. In addition, the low energy barrier induced by the nanodomains reduced the coercive field and ensured an easy switching of domains in the external electric field. The <001> orientation of grains lowers the angles between the external electric field and the spontaneous polarization and strains in neighboring grains leading to enhanced ferroelectric performances in textured samples.

Keywords: Textured ceramics, Piezoelectric properties, Nanodomains, Soft-hard doping, Dielectric relaxation

Résumé

Les matériaux ferroélectriques sont largement utilisés dans d'importante technologies incluant les transducteurs, actionneurs, capteurs... Dans ce contexte, les matériaux ferroélectriques constituent une classe importante de matériaux fonctionnels.

Parmi les structures ferroélectriques les plus exploitées, ceux à base de $Pb(Zr,Ti)O_3$ abrégé (PZT) offrent de bonnes performances dans des dispositifs opérationnels. Malgré cet aboutissement en terme de valorisation, la compréhension fondamentale des caractéristiques physiques des systèmes basés sur le PZT continue de susciter l'intérêt d'une large communauté scientifique. Par exemple, les processus de dopage « Soft-Hard » du PZT qui génèrent des défauts dipolaires contribuant aux réponses diélectriques et piézoélectriques, continuent de faire l'objet de développements dans le domaine des sciences des matériaux. Cependant, un intérêt croissant porte sur la mise en œuvre de structures ferroélectriques exemptes d'éléments chimiques nocifs pour l'environnement dont la teneur en plomb. Dans ce cadre, les systèmes à base de $BiFeO_3$-$BaTiO_3$ (BF-BT) ont suscité beaucoup d'intérêt en tant que matériaux ferroélectriques sans plomb. En raison de leurs microstructures formées de grains ferroélectriques, les propriétés piézoélectriques ne peuvent pas être améliorées sensiblement même par des processus de dopage. La synthèse de monocristaux est une voie pertinente pour améliorer les propriétés ferroélectriques mais son intérêt est limité pour un développement à grande échelle en raison des conditions drastiques requises pour la synthèse cristalline et le coût élevé de telles structures. Ainsi, la réalisation de matériaux ferroélectriques texturés offre une approche alternative pour réaliser des systèmes à hautes performances ferroélectriques. Le mécanisme est basé sur le fait que les domaines ferroélectriques sont forcés de s'aligner le long d'une direction définie. Au-delà d'une mise en œuvre facile, la méthode de texturation de domaines est reproductible et conduit à des propriétés optimisées.

Ce travail de thèse porte sur des études systématiques portant sur les céramiques à base de PZT et de BF-BT. La première contribution est dédiée à l'analyse des microstructures, des phases cristallines et des propriétés ferroélectriques dans les

systèmes PZT. Les travaux ont montré le rôle du dopage Soft-Hard sur les propriétés structurales, morphologiques et électriques des matériaux dopés accepteurs. Dans une deuxième partie, l'interaction des microstructures et des propriétés électriques a été étudiée dans les systèmes BF-BT. L'optimisation des conditions de fabrication à travers la composition chimique et le traitement thermique fournissant contribuent aux propriétés piézoélectriques améliorées dans ces systèmes sans plomb. Pour troisième partie des travaux, elle porte sur la texturation par des agents texturants à base de lamelles nanométriques de $BaTiO_3$ et les propriétés des céramiques BF-BT. Des études expérimentales de fabrication, texturation et les caractérisations des propriétés ferroélectriques et électromécaniques ont été corrélées avec l'organisation structurale et morphologique des céramiques texturées. Les principaux résultats sont mis en relief ci-dessous:

(1) La corrélation entre la microstructure et les propriétés ferroélectriques a été étudiée dans des céramiques «soft» $(Pb_{0.94}Sr_{0.05}La_{0.01})(Zr_{0.53}Ti_{0.47})O_3$ (PSLZT) fabriquées par une réaction à l'état solide conventionnelle en utilisant un dopage Fe^{3+} pour former un système $PSL(ZT)_{1-x}$-Fe_x. La variation du taux de dopage module les caractéristiques ferroélectriques et le comportement électromécanique. Avec de faibles teneurs en Fe^{3+} inférieures (0, 010% en poids), les échantillons ont montré des caractéristiques s'apparentant celles des matériaux « soft ». La polarisation résiduelle des échantillons est d'environ 35,7 $\mu C/cm^2$ avec la constante piézoélectrique et la déformation de 412 pC/N et 0,22% (25 kV/cm) respectivement. Avec l'augmentation de la teneur en Fe^{3+}, la quantité de lacunes d'oxygène augmente et les domaines ferroélectriques subissent un accrochage (pinning) sous des champs électriques appropriés. Ainsi, les céramiques obtenues présentent les caractéristiques de matériaux «Hard» avec de faibles constantes piézoélectriques et des facteurs de qualité mécanique Q_m de l'ordre de 500. Les microstructures et les performances piézoélectriques des échantillons ont également été affectées par le processus de frittage. En augmentant les températures, l'échantillon «soft» (x = 0, 005) a montré des grains plus poreux conduisant à une faible densité et une diminution du coefficient piézoélectrique. De plus, des études comparatives, sur des échantillons

alignés électriquement ou non, soulignent l'influence des défauts dipolaires sur les propriétés ferroélectriques des échantillons « Soft-Hard ». La polarisation des défauts dipolaires est alignée (pinning) le long de la polarisation spontanée pour les céramiques à dopage « soft ». Cependant, cet effet de « pinning » des domaines a tendance à se dégrader dans les céramiques à dopage « hard ».

(2) Les céramiques $BiFeAlO_3$-$BaTiO_3$ dopées par Al au site B ont été systématiquement étudiées avec un focus particulier sur leurs microstructures et les propriétés électriques, afin d'optimiser les performances ferroélectriques. Il a été constaté que la distorsion de la phase rhomboédrique est la plus élevée pour une forte teneur Al de l'ordre de x = 0,030. La polarisation spontanée et résiduelle la plus élevée a été obtenue dans ce système avec les valeurs de 36,8 $\mu C/cm^2$ et 31,5 $\mu C/cm^2$, respectivement. La grande distorsion et la fraction élevée de la phase rhomboédrique ont joué un rôle essentiel dans l'amélioration du comportement ferroélectrique. Les études par la spectroscopie Mössbauer du ^{57}Fe montrent une augmentation du désordre des ions Fe^{3+} avec des rapports de dopage Al plus élevés; effets qui contribuent aux caractéristiques prononcées d'une transition de phase diffuse. Avec un dopage Al supérieur à 0,045, les échantillons présentent deux comportements de relaxation diélectrique distincts, qui ont été analysés par le modèle « Brick-wall ».

(3) Les céramiques texturées $BiFeGaO_3$-$BaTiO_3$ (BFG-BT) ont été étudiées et leurs performances ferroélectriques corrélées avec l'organisation et la microstructure. L'échantillon texturé BFG-BT présente des propriétés ferroélectriques améliorées suggérées par l'analyse des propriétés de déformation et diélectriques à différentes températures. Le coefficient piézoélectrique de l'échantillon texturé atteint 685 pm/V à 180 °C. Les études par diffraction XRD ont montré une structure ferroélectrique stable pour les échantillons texturés sans aucune transition structurale de la phase ferroélectrique ($P4mm$ et $R3c$) à la phase paraélectrique (cubique). La phase rhomboédrique orientée et la haute densité de nano-domaines jouent un rôle essentiel dans l'amélioration des contraintes des matériaux texturés. De plus, la barrière de faible énergie induite par les nanodomaines réduit le champ coercitif et assure un alignement aisé des domaines sous un champ électrique externe. L'orientation <001> des grains

abaisse la désorientation entre le champ électrique externe et la polarisation spontanée ainsi que les contraintes dans les grains voisins avec comme conséquence une amélioration des performances ferroélectriques dans les échantillons texturés.

Mots clés: Céramiques texturées, Propriétés piézoélectriques, Nanodomaines, Dopage soft-hard, Relaxation diélectrique

Contents

General Introduction

Ferroelectric materials combine the interactions between applied electric fields, induced polarizations and the mechanical strains. The energetic cocnerns are based on the interpay between electrical and mechanical excitation-reaction processes. To date, ferroelectric materials have played essential roles in a wide range of devices required for key industrial needs. However, due to the rapid and continuous developments of technologies, diverse innovative fields are being more demanding in terms of efficient piezoelectric coefficients and under extreme working conditions (temperature, pressures, atmosphere,..). It is noteworthy that a relevant solution used to enhance ferroelectric properties lies in the doping process, which adjusts phase structures of materials and reduce the energy barriers for domains switching [1, 2]. In addition, adjusting orientation of grains as it can be realized in textured media ensures an effective way to promote ferroelectric properties by privilegied specific orientation within the host doped materials [3-5].

Till now, the lead-based materials have already taken the dominating proportion among all the commercial ferroelectric ceramics. Here are some various lead-based systems, including $Pb(Mn_{1/3}Nb_{2/3})O_3$-$Pb(Zr,Ti)O_3$ (PMN-PZT), $Pb(Zn_{1/3}Nb_{2/3})O_3$-$Pb(Zr,Ti)O_3$ (PZN-PZT), $Pb(Ni_{1/3}Nb_{2/3})O_3$-$Pb(Zr,Ti)O_3$ (PNN-PZT). It was reported that PMN-PT relaxor ferroelectrics exhibited high piezoelectric constants reaching values up to 1500 pC/N [6, 7]. However, the Curie temperature (T_C) of PMN-PT was low and then limits the application in the high-temperature range. On the contrary, $Pb(Zr_{1-x}Ti_x)O_3$ (PZT) piezoelectric ceramics revealed piezoelectric constants d_{33} at 750 pC/N, and Curie temperature in the range from 180-320 ℃ [8]. PZT is regarded as one of the most widely applied lead-based materials. In addition to the superior performance, PZT ceramics also possess diverse advantages, such as the easy synthesis, low cost, variable compositions [8]. Nevertheless, there still maintain many scientific issues in PZT-based piezoelectric ceramics to be investigated profoundly, such as softening-hardening doping features, and role of defect dipoles on the polarizations.

In view of the environment-friendly issues, undoubtedly tremendous efforts have been devoted to lead-free systems with examples of (K,Na)NbO_3 (KNN), $BiFeO_3$-$BaTiO_3$ (BF-BT), (Bi,Na)TiO_3 (BNT) and so far [6, 9-14]. Since these systems do not contain the toxic Pb element and can meet the sustainable economic development, they are considered to be promising alternatives to the conventional counterparts [15, 16]. But in fact, lead-free materials cannot completely replace traditional lead-based PZT, due to their inadequate stabilities and insufficient properties. Therefore, several approaches were developed to improve the piezoelectric performances via improving synthesis routes, sintering and doping processes, etc. On the other hand, it was reported that textured $(K_{0.5}Na_{0.5})NbO_3$ reached high piezoelectric constants at 416 pC/N with the contribution from the orientation of grains. Lee, et al. also reported lead-free $_{0.67}Bi_{1.05}(Fe_{1-x}Ga_x)O_3$-$_{0.33}BaTiO_3$ materials synthesis by the solid state method. The phase of this system was close to the morphotropic phase boundary (MPB) with a high piezoelectric constant 402 pC/N, and a high Curie temperature 454 ℃ [6, 7]. Thus, properties of lead-free ferroelectric ceramics can be enhances by several strategies. For some lead-free systems, doping may induce relaxation characteristics in addition to the variation in phase structures. Meanwhile, the long-range structures of ferroelectrics are lost and transform into short-range polar nanoregions (PNRs) [17], which ultimately results in the alteration of ferroelectric properties. In the light of this situation, it is extremely essential to integrate phase structures and the orientation of grains with ferroelectric properties, and to investigate the inner mechanism for the promoted ferroelectric behaviors.

This dissertation highlights investigations on the relation between structure and performance by adjusting the phase structures of PZT and BF-BT systems by doping elements. It also emphasizes textured lead-free BF-BT materials realized by the orientation of grains and promoting the ferroelectric properties.

In the first chapter of the dissertation, a brief review on the main classes of ferroelectric materials, their dielectric features and current developments.

In the second chapter, exhaustive description of the synthetis protocols was provided. The operating principles of diverse characterisations facilities and the relevant models

correlating dielectric and piezoelectric parameters were discussed in details.

In the third chapter, a set of PSL$(ZT)_{1-x}$-Fe_x ceramics with different compositions wassuccessfully prepared by a conventional solid-state reactive method. The conversion of materials from “soft” features to “hard” features was also realized through adjusting the La/Fe ratio. The influences of annealing temperature on the microstructures, phase structures, and the performances in dielectric, ferroelectric and piezoelectric were analyzed in details. Moreover, the polarization and the strain of soft and hard PSL$(ZT)_{1-x}$-Fe_x systems were investigated in non-poled and poled configuratoions. The pinning effect induced by dipole defects P_D was analyzed over spontaneous polarization P_s in hard materials with the assistance of “dipole defects” models.

In the fourth chapter, the conventional solid-state reactive method was also employed to synthesize $BiFe_{1-x}Al_xO_3$-$BaTiO_3$ (BFA-BT) ceramics. By introducing Al^{3+} into the system, the comprehensive performance was optimized and the relevant one was selected among all the counterparts. Phase structures and the lattice distorsions were analyzed with respect to the enhanced polarization. Mössbauer results were analyzed at the atomic scale through the disorder of B sites caused by Al^{3+} subsituions to Fe^{3+} in different systems.

In the fifth chapter, textured lead-free $BiFeGaO_3$-$BaTiO_3$ (BFG-BT) ceramics were synthesized by the reactive templated grain growth method. Compared with the untextured materials, the textured ones revealed substantially enhanced ferroelectric properties. The microstructure analysis points out the emergence of nanodomains in textured systems which contribute to reduce the energy barriers for domain switchin contributing then to the low coercive field. The ratio of rhombohedral phases and the grains orientation along <001> were responsible for the high spontaneous polarization.

The general conclusion highlights the main achieved new and original contributions on ferroelectric systems based on new compositions and performant functional lead-free ceramics. The perspectives are discussed notably from the expected future practical applications of the considerd systems offering performances and working stability at high temperatures.

Chapter 1 Overview on ferroelectric materials: structures and properties

1.1 Development and applications of piezoelectric, ferroelectric materials

The piezoelectric effect is involved in several classes of functional materials and consists in the energy conversion between a mechanical stress and an electrical activity. The manifestation of this effect in crystalline materials requires non-centro-symmetric structures. Depending on the role played by the mechanical stress or the electrical voltage in the process of excitation↔reaction (mechanical↔electrical), the piezoelectric effect is classified into two categories, direct piezoelectric effect and inverse piezoelectric effect.

In a similar context, ferroelectric materials are also non-centro-symmetric structures possessing polarization which exist even in the absence of an external electrical field but can be switched under an applied voltag. For a typical ferroelectric material, its spontaneous polarization can be altered if the temperature is increased above characteristic value T_C, i.e. the Curie temperature. In the twenty point groups of piezoelectric materials, only ten of them can form the polarization under the external electric field, m, mm2, 4mm, 3m, 6mm, 1, 2, 3, 4, 6. Thus, ferroelectric materials belong to a subclass of piezoelectric materials.

1.1.1 Piezoelectric materials

The piezoelectric materials can be realized from organic or inorganic structures possessing the symmetry requirement for the involvment of piezoresponses. One of the popular and represnetative piezoelectric organic material, polyvinylidene fluoride (PVDF) is worthy of interest as it was the most investigated due to its essential role in multifunctional soft materials [18, 19]. For the inorganic piezoelectric materials, the well known structures with the ABO_3 formulae can be divided into perovskite, bismuth-layered and tungsten-bronze structures. On the other hand, depending on the

needed applications, piezoelectric materials can be tailored as single crystals, ceramics or thin films. The piezoelectric performance of single crystals is usually higher than the ceramic counterparts. But the limitation from using single crystals depends on their drastic synthesis conditions. From another side, piezoelectric thin films are well adapted for integrated microdevices [20]. There are also popular pervskite piezoelectric materials, such as $Pb(Mg,Nb)O_3$-$PbTiO_3$ (PMN-PT), $Pb(Yb,Nb)O_3$-$PbTiO_3$ (PYN-PT), $Pb(Zr,Ti)O_3$ and so forth [4, 21-23]. When processed as ceramics, they may exhibit high piezoelectric constant d_{33} in the order of 500 pC/N [24] while single crystals show the high d_{33} at 2000 pC/N [15].

For the relevant applications of piezoelectric materials, the efforts deal with the improvment of excellent temperature-stability, high-output displacement and sensitivity to ensure the essential components as filters, resonators, piezoelectric transducers, actuators, sensors...

1.1.2 Ferroelectric materials

Ferroelectric domains

The microstructures of perovskite ferroelectric materials are organized in domains with defined macroscopic polarization when the sample temperature remains below a critical value that is the Curie temperature. Indeed, when the sample temperature decreases from high values, with a cubic paraelectric phase, to low temperatures leading to a structural phase transition with the frmation of a polar ferroelectric phase. In this state, the non-centro-symmetric structure leads to the formations of ferroelectric domains with defined aligned polarization. These ferroelectric domains can be divided into 180 ° domain and non-180 ° domain from the degrees of their polarization alignment. Switching the 180 ° domains decreases the electrical energies of the ferroelectric material and didn’t cause any displacement under external electric fields. Switching the non-180 ° domains reduces the mechanical energies of ferroelectric materials and induces a displacement under the applied electric field. Thus, ferroelctric domains as involved for the well known $BaTiO_3$ ceramic shows 90 ° domains in a tetragonal state. When the phase of this ceramic transform into the

rhombohedral phase, there exists 71 ° and 109 ° domains. In Fig. 1.1, Zhai et al. reported the 90 ° domains of textured $KNaNbO_3$–based ceramics with the observation of TEM [25]. This phases is formed by a coexistence of a rhombohedral and orthorhombic structure.

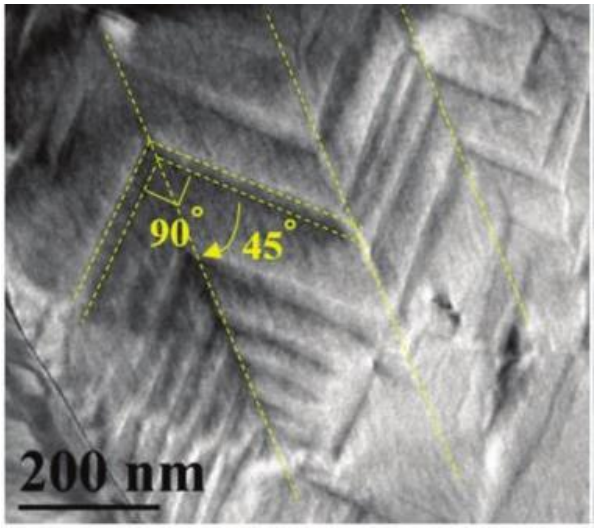

Figure 1.1 90 °domains of KNN piezoelectric materials [25].

Ferroelectric properties

The ferroelectric materials are marked by the particular polarization-electric field (*P*-*E*) hysteresis loop, which is an important feature of ferroelectric properties. Fig. 1.2 shows the hysteresis loop of classic ferroelectric materials. The polarization of the materials changes with switching of domains under external electric fields as it may be applied in ferroelectric memories. From Fig.1.2, we may notice the polarization OD representing the saturated polarization P_s while the polarization of OC stands for remnant polarization P_r and situates the level of the ferroelectric performance. The electric field OE is defined as the coercive field E_c, indicating the degree of domains switching. As the polarization inside ferroelectric domains exhibits variable orientation, the overall value in the material is null. After poling under an electric field and at high temperatures, the microscopic dipoles will realign with the direction of the electric field. When the external electric field is removed, most of spontaneous polarization will retain the poled direction, exhibiting the remnant polarization P_r.

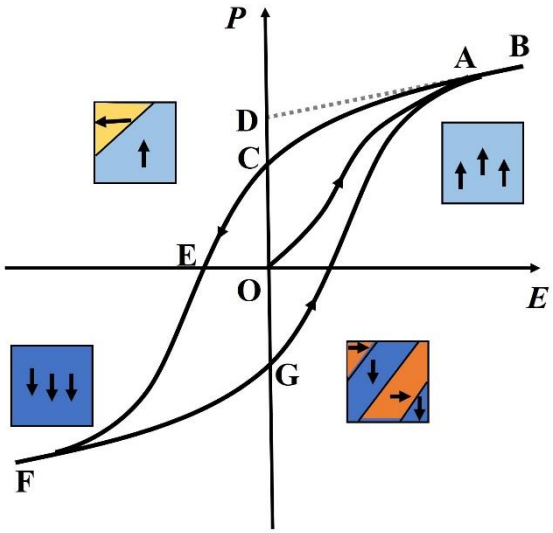

Figure 1.2 Polarization-electric field (*P*-*E*) hysteresis loop and switching of ferroelectric domains in classic ferroelectric materials.

Ferroelectrics and anti-ferroelectrics

Among all kinds of ferroelectric ceramics, perovskite ferroelectric ceramics are widely applied. Fig. 1.3 illustrates the unit cell of ABO_3 perovskite structure, where ions at the A site or B site can be substituted by the ions with different valence and radius. For example, by doping process, the Curie temperature (T_C) of $BaTiO_3$ can be augmented from 120 ℃ to 490 ℃ via substituting Ba^{2+} by Pb^{2+}. Moreover, T_C of $BaTiO_3$ is lowered when Ba^{2+} is replaced by Sr^{2+} or Ti^{4+} substituted by Zr^{4+} or Sn^{4+}. $BaTiO_3$ ceramics with a low doping ratios have an important influence on dielectric and piezoelectric parameters.

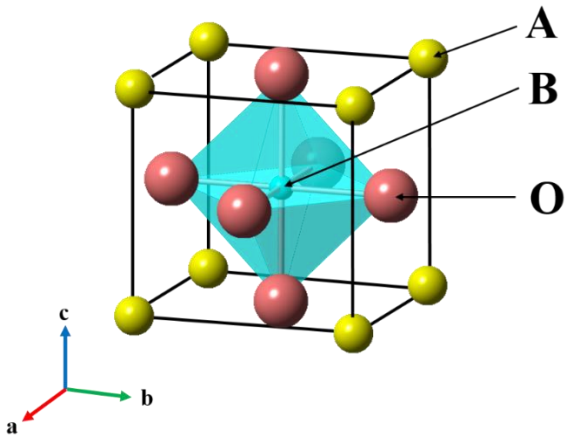

Figure 1.3 Unit of lattices in ABO_3 perovskite ferroelectrics.

In anti-ferroelectric materials, neighbouring dipoles align in anti-parallel directions

and then not polarization is involved in the anti-ferroelectric state. Electrical properties of ferroelectrics and anti-ferroelectrics have some similarities and differences. The smilarites are related to dielectric contants which change significantly from an anti-ferroelectric phase or a ferroelectric phase to the paraelectric phase. Both of them possess electrical susceptibilities which follow the Curie-Weiss law in the paraelectric phase. The main difference between ferro- and anti-ferroelectric materials lies in the absence of a spontaneous polarization in the anti-ferroelectric state. However, some anti-ferroelectric state can transform into a ferroelectric state under an external electric field leading to drastic increase of the polarization. In this case, the P-E curve exhibit the characteristic double hysteresis loops [26].

1.1.3 Morphotropic phase boundary

It is feasible to enhance the piezoelectric performance through synthesizing components close to the morphotropic phase boundary (MPB). Earlier, a physical mechanism was used to elucidate the piezoelectric performance enhancement by MPB. Indeed, when MPB is involved, the coexistence of two phases contribute to the the polarization anisotropy, which is considered as the origin of the amended piezoelectric behavior [25]. Recent reports identified that a monoclinic phase, located at the interface between the tetragonal phase and the orthorhombic phase, plays an essential role in the enhancement of the piezoelectric responses. The monoclinic phase acted as a bridge that reduced energies of phase transition among tetragonal-monoclinic-orthorhombic phases. Furthermore, Landau free energy model was also used to analyze the thermodynamics of MPB, in Fig. 1.4 [7]. The free energy of the MPB composition is isotropic, being independent on the polarization direction. The absence of the polarization anisotropy suppresses any energy barrier for the polarization rotation from a tetragonal state to a rhombohedral state. Thus, the triple-point-type MPB has very high piezoelectric and dielectric parameters as reported in several contribuions [7, 25, 27, 28].

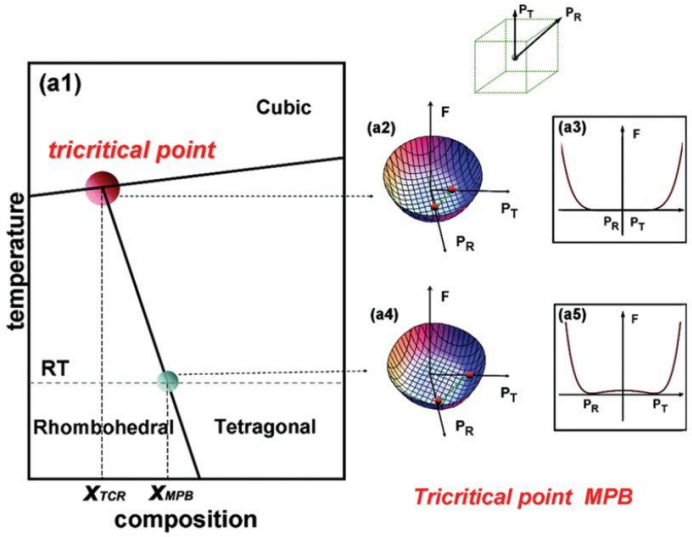

Figure 1.4 Mechanism of high performances surrounding MPB-Landau free energies [7].

For the lead-free compound $KNaNbO_3$-based ceramics, former reports underline the piezoelectric performance by tuning the polymorphic phase transition. Zhu et al. performed an adjustement of the temperature of phase transition in lead-free $KNaNbSbO_3$-$BiFeO_3$-$Bi_{0.5}Na_{0.5}ZrO_3$ [2]. By ion doping they succeed to shift the rhombohedral-tetragonal (R-T) tansition temperature to higher values. Conversely, the temperature of the tetragonal-orthorhombic transition was also shifted to lower values. The piezoelectric constant d_{33} about 550 pC/N was optimized at room temperature [2]. However, some drawbacks remain non-resolved for practical applications. Among the limitations, we notice gradient R-T boundaries, low stabilities, complex compositions, and narrow temperature's range for the sintering process.

1.2 Role of defects in ferroelectric ceramics

Defects can be intrinsically fromed in ferroelectric ceramics and consist in oxygen vacancies and cation vacancies. Oxygen vacancies play a crucial role in electrical properties of functional materials including the dielectric relaxation behaviors or the pinning effects of ferroelectric domains. As example, a small quantity of cation vacancies can generally enhances the distortion of the crystalline strcuture and improves piezoelectric responses [29]. Based on this statement, several investigations were delaing with various doping elements introduced in the host lattice in order to

optimize the piezoelectric properties [30, 31].

1.2.1 Dopant effects and formation of defects

Substituting low valence ions by high valence ions can induce cation vacancies in the materials, which has been defined as donor doping or soft doping. Generally, as for PZT systems, Pb^{2+} at the A site is substituted by La^{3+}, Bi^{3+}. Also, Zr^{4+} and Ti^{4+} at the B site are substituted by Nb^{5+}, Ta^{5+}, Sb^{5+}, W^{6+}, Te^{6+}, respectively. These substitutions form cation vacancies, for example, lead vacancies. The following formula illustrates the evolution process of the defects, based on La^{3+} substituting Pb^{2+}:

$$La_2O_3 \xrightarrow{2PbO} 2La_{Pb}^{\cdot} + V_{Pb}'' + 3O_O^{\times} \quad \ldots(1.1)$$

The doping by high valence La^{3+} increases the content of lead vacancies and enhances the distortion of the host perovskite lattice. Cation vacancies also reduce the energy barrier between different ferroelectric domains. This effect enhances the mobility of domains, and softens the piezoelectric materials. It contributes also to improve the piezoelectric responses, and enlarges the strains induced by domains switching. In summary, in spite of increasing mechanical losses and dielectric losses, donor doping enhances dielectric constants, the remnant polarization, electromechanical coupling coefficients and piezoelectric constants [32-35].

On the orther hand, oxygen vacancies would be produced in the crystals if higher valence ions is substituted by ions with lower valence. This kind of phenomenon is called acceptor doping or hard doping. The positive charges could be non-compensated when Pb^{2+} at the A-site is substituted by Li^{+}, Na^{+}, K^{+}, and so forth, or Ti^{4+} at the B site is replaced by Fe^{3+}, Mg^{2+}, Al^{3+}, Ni^{2+} and Cr^{3+}. In theses cases, oxygen vacancies are ultimately produced to ensure the electric neutrality. As the example of PZT doped by Fe^{3+} ion, the following equation traduces the defect formations:

$$Fe_2O_3 \xrightarrow{ZrO_2/TiO_2} 2Fe_{Zr,Ti}' + V_O^{\cdot\cdot} + 3O_O^{\times} \quad \ldots(1.2)$$

Fe^{3+} ions doping modifies the content of oxygen vacancies in the materials. This contribute to modulate the piezoelectric properties and improve the practical application of the materials in workable technologies. The oxygen vacancies caused by the acceptor doping tend to limit the mobility of domains and suppress their switching under an applied exterior electric field compromising then the piezoelectric responses as well as decreasing the hysteresis of the strain. The main advantages from the acceptor doping include increasing mechanical quality factors, the high coercive field, low dielectric constants and losses. It contributes also to decrease the electromechanical coupling coefficient and then lowering the piezoelectric constants [36, 37].

1.2.2 Model of defect dipoles

In recent years, several sets of investigations have pointed out differences between the effects of cation vacancies created by donor doping and those induced by oxygen vacancies caused by acceptor doping. The last defects have tendency to associate with doping ions leading to the formation of defect dipoles. The pinning effect of ferroelectric domains by defect dipoles is much stronger than that of isolated oxygen vacancies. On the contrary, lead vacancy cannot induce pinning effect of domains, because it is hard to couple with substituted ions to form defect dipoles, due to the low recombination energy about 0.04 eV.

Few decades ago, Robel et al. proposed the “boundary effect” to interpret the pinning effects by defect dipoles [36]. They authors considered that the change of features in aging ferroelectric ceramics depend on defect dipoles which pin the domain walls, affecting the switching of domains and polarizations. As a consequence, the samples would exhibit double polarization-electric field (*P-E*) hysteresis loops. But this approach cannot be adapted to single crystals formed by single domains with regard to the double hysteresis loops remain observed after aging the single crystals. Later, Ren et al. raised “volume effect” for defect dipoles, that is, the symmetry-conforming theory [38]. Fig. 1.5 depicts the symmetry-conforming property for point defects in the perovskite $BaTiO_3$ ferroelectric materials [38]. The crystal contains O^{2-} vacancies and

D^{3+} acceptor impurity ions occupying B^{4+}. In Fig. 1.5(a), this combination of defects satisfies the requirement for the charge neutrality. In the cubic paraelectric phase, there is an equal probability of finding an O^{2-} vacancy in the neighbouring equivalent sites (1, 2, 3, 4) of the defect D^{3+}. When the temperature decreases down to the formaton of the ferroelectric phase, the polar tetragonal symmetry makes the sites 1, 2, 3, 4 no longer equivalent with respect to the defect D^{3+} (site 1 and 2 are equivalent but 3 and 4 are not). It follows that the defect probabilities should be $p_1^V = p_2^V \neq p_3^V \neq p_4^V$ in accordnace with the polar tetragonal symmetry of the lattice shown in Fig. 1.5(b). These non-centrosymmetric distributions of charged defects form the defect dipoles P_D. Electron paramagnetic resonance (EPR) experiments and theoretical modelling suggest that defect dipoles P_D tend to align along the spontaneous polarization direction P_s.

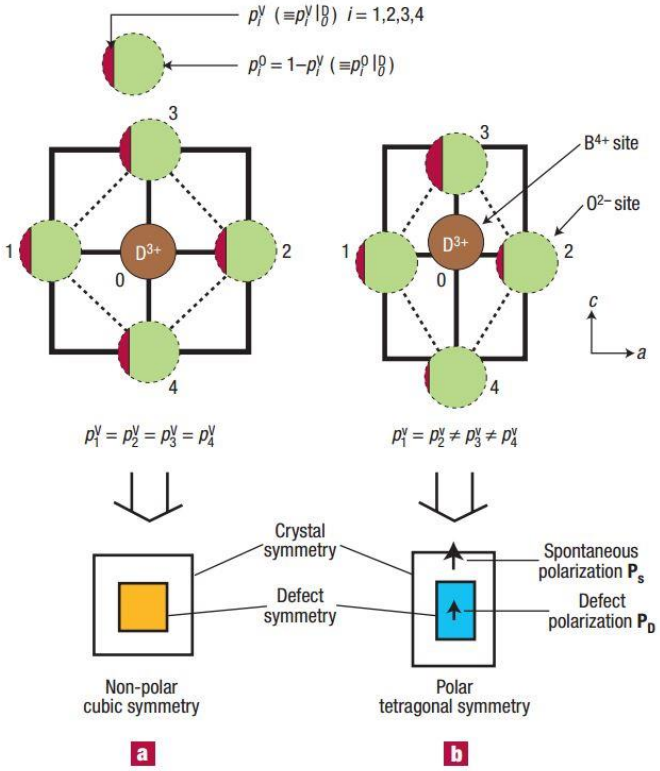

Figure 1.5 Symmetry-conforming property of point defects in the perovskite structure, (a) non-polar cubic paraelectric state, (b) polar tetragonal ferroelectric state [38].

Defect dipoles caused by acceptor doping are induced by the migration of oxygen vacancies in order to minimize the Gibbs free energies of the whole system. Since a

time delay is generally required for the migration of oxygen vacancies, defect dipoles tends to arrange randomly when piezoelectric materials undergo a transition from the high-temperature paraelectric phase to the low-temperature ferroelectric phase. That is, the transport speed of oxygen vacancies cannot match with the structural transition kinetics. Therefore, a cubic symmetry appears with respect to the arrangement of defect dipoles, which is an unstable state. Nevertheless, it can be expected that oxygen vacancies can be arranged along defined paths by applying a specific temperature to accelerate their migration. As a result, an alignment between defect dipoles and the spontaneous polarization direction can be realized. The evolution of defect dipoles is thus a chronic process, which is correlated to the fatigue and aging features in ferroelectric materials [38].

Defect dipoles have been demonstrated experimentally notably by Robertson et al. who observed that defect dipoles in PZT and $BaTiO_3$ arranged along the spontaneous polarization by using EPR [39]. In the Fig. 1.6 (a), they found that defect dipoles could align when samples were poled in the electric field of -450V at the temperature of 110 ℃. But this phenomenon cannot be detected in $SrTiO_3$ or other materials in their paraelectric phase shown in Fig. 1.6 (b). In addition, the arrangement adopted by defects dipoles depend on the annealing method of ferroelectric materials, see for instance the work of Keeble et al. [40]. The authors report on newly grown Fe-doped $PbTiO_3$ monocrystals which exhibit two crystalline sites for Fe^{3+} centers inferred from EPR analysis indicating two distinct arrangement modes of defect dipoles. Furthermore, after a thermal treatment at 400 ℃ in vacuum, only one kind of Fe^{3+} centers remains observed and implies a unique arrangement pattern for the involved defect dipoles.

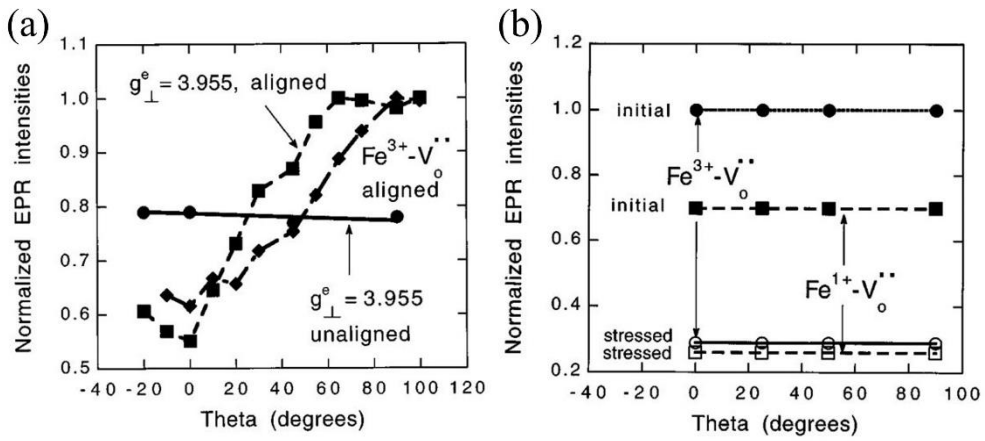

Figure 1.6 Defect dipoles alignment along the applied electric field for various temperatures as determined by EPR in (a) Fe-$BaTiO_3$ ceramics, (b) Fe-$SrTiO_3$ ceramics [39].

The double P-E hysteresis loop could be marked by the contribution of defect dipoles in aging samples as illustarted in Fig. 1.7 in the aged Mn-doped $BaTiO_3$ single crystal [31]. When the electric field is applied, the polarization increases with raising the electric field. However, when the electric field decreases to zero, the polarization does not show a remanent contribution due to the defect dipoles being aligned along the spontaneous polarization direction in aging samples. The total polarization is vanishing for aging ferroelectric materials. When the electric field is applied, switiching of defect dipoles requires more delay to aling along the electric field and then remain along the original oriantation state. With decreasing the electric field to zero, defect dipoles force the spontaneous polarization to align along the original state. The total polarization is close to zero again in the absence of the electric field. Thus, the above analysis account for the double polarization-electric field hysteresis loop in aged samples.

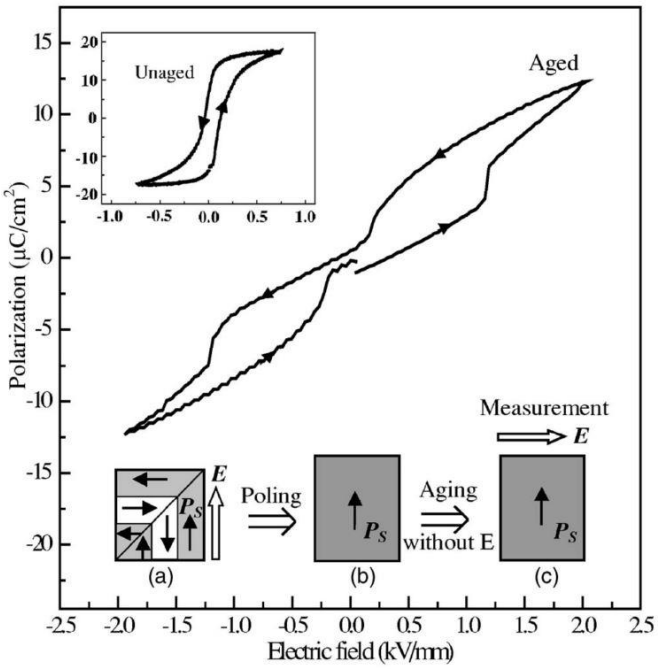

Figure 1.7 Double polairization-electric field (*P-E*) hysteresis loop of the aged Mn-doped $BaTiO_3$ single crystal [31].

The offset polarization-electric field hysteresis loop could also appear in some acceptor-doping systems. As seen in Fig. 1.8, an internal bias electric field is induced inside the material, which has been defined as the bias electric field E_i [41, 42]. It could be calculated by the following definition [43]:

$$E_i=(E_1+E_2)/2 \quad \ldots(1.3)$$

Where E_1 and E_2 are the peak field of forward and backward domain switching processes in the *P-E* loop, respectively. The derivative of the polarization to the field, dP/dE, was obtained by using each P-E loop. In order to simply the calculation, some authors use the bias electric field as E_i induced by the non-symmetric center in the P-E loop [44]. The formation of the bias electric field E_i is relative to the defect dipoles. After aging or poling efficiently, inner defect dipoles are prone to align along the spontaneous polarization, leading thus to the formation of an internal electric field. When positive electric field is applied along to the E_i, the bias electric field contributed to the polarization and strain. On the contrary, the bias electric field would prevent the rotation of domains if a converse electric filed is given, resulting in the

low polarization and strain. On this basis, the applied exterior electric filed results in the offset hysteresis loop. Zeng et al. reported that the bias electric field E_i was larger with the increasing poling electric field in PZT ceramics, indicating that the amount of aligned defect dipoles became higher [44]. It was testified that E_i correlates to the alignment of defect dipoles. The occurance of E_i enhances the stability of ferroelectric domains, resulting in the high mechanical quality factor of materials [45].

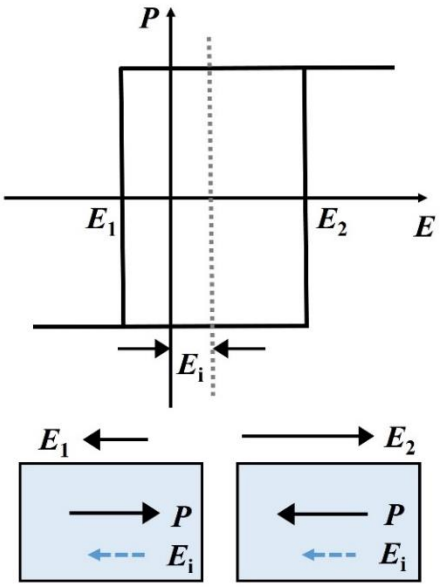

Figure 1.8 Offset polarization-electric field (*P*-*E*) hysteresis loop.

1.3 Diffused transition in ferroelectric ceramics

Several reports have shown that the dielectric spectra of some ferroelectric materials exhibit broad features when the sample temperature varies around a given critical value that is the transition temperature. The broadening of dielectric peak around the crticial temeprature is intimately related to diffused nature of the phase transition [46, 47]. This behavior can manifest on the dielectric function broadening with different strengths depending on the materials features. Structural or composition disorder are among the parameters which perturbe the long range order of the underlying structures and induse a diffused phase transition.

1.3.1 Structural features of relaxor ferroelectrics

The relaxation processes are defined by the mechanisms involved in a macroscopic

system when transferring from one thermodynamic equilibrium state into new ones. This process is driven by the energy exchange between different microstructures. Whether in macroscopic or microscopic perspective, this transferring process always need a certain time delay to reach a new stable state. The dielectric behaviors in relaxor ferroelectrics show the features of a diffused phase transition and a frequency dispersion [48]. The characteristic peak which manifest for the ferroelectric-paraelectric transition tends to expend during the diffused phase transition. For the frequency dispersion, it means that the peak of dielectric constants and losses shifts to the higher temperature with increasing frequencies. It is worth noting that, the relaxation processes are not representative of the phase transition, but correlate with the changes inside special microstructures.

Polar nanoregions (PNRs) are one kind of the most typical structural features of PMN relaxor ferroelectric, which is correlated to dielectric, ferroelectric and piezoelectric properties. Li et al. pointed out the structural characteristics of relaxor ferroelectrics with different temperatures, as shown in Fig. 1.9 [48]. PNRs emerged in the paraelectric phase of materials below Burns temperature (T_B), which resulted in the polarization change. When the temperature decreases down to the depolarized temperature T_d, the PNRs with smaller sizes can rapidly grow to larger ones and their number is thus reduced. Further decreasing the temperature below T_d, the sample is filled with long-range ferroelectric domains, being indicative of classical ferroelectric materials. Due to the low size and high active feature, the ceramic exhibits excellent electric property at the temperature near T_d.

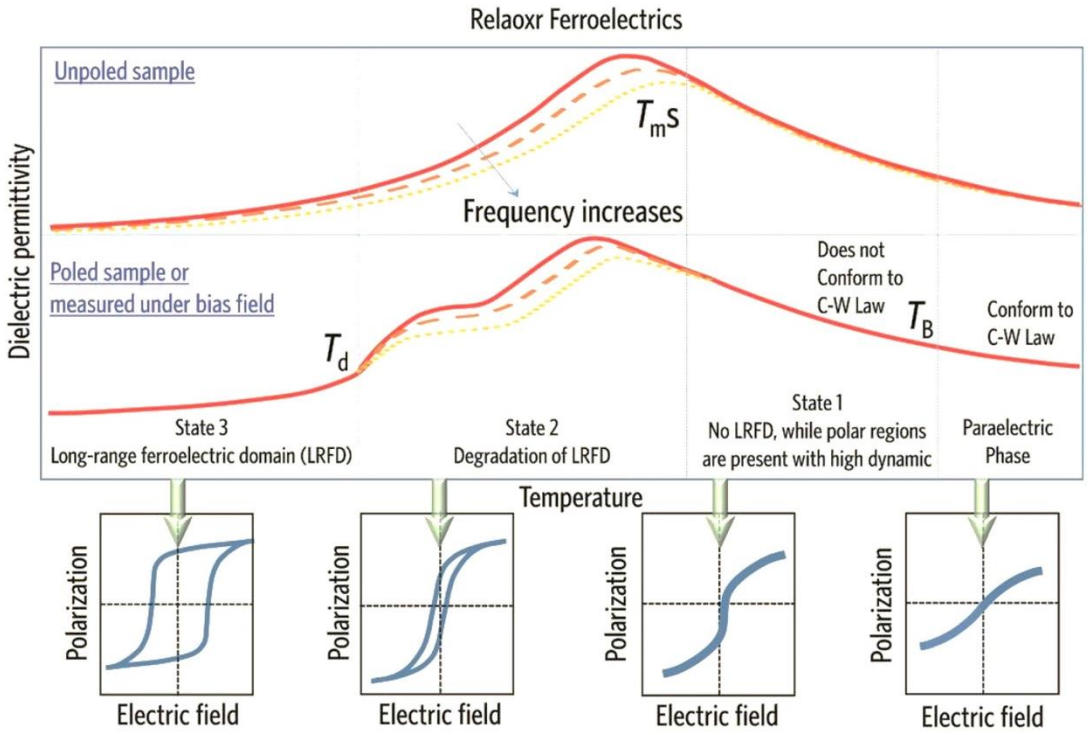

Figure 1.9 Characteristics of mictrostructural, maroscopic dielectric and ferroelectric properties in relaxor ferroelectrics [48].

1.3.2 Dielectric behaviors of relaxor ferroelectrics

In Fig. 1.10(a), the temperature dependence of dielectric constants of classical ferroelectrics obeys a Curie-Weiss law. The definition is as follows [49]:

$$\frac{1}{\varepsilon} = \frac{T-\theta}{C} \qquad \ldots(1.4)$$

Here, C is the Curie-Weiss constant, θ is Curie temperature. By contrast, dielectric constants of relaxor ferroelectrics exhibits strong deviation from Curie-Weiss law shown in Fig. 1.10(b), obeying the revised Curie-Weiss law. The equation is as follows [49]:

$$\frac{1}{\varepsilon} - \frac{1}{\varepsilon_m} = \frac{(T-T_m)^\gamma}{c} \qquad \ldots(1.5)$$

Where, ε_m means the maximum dielectric constant, T_m means the temperature at the maximum dielectric constant, C is the Curie-Weiss constant, γ means the diffused degree in the range of 1 to 2. As for classic ferroelectrics, γ is 1. As for relaxor

ferroelectrics, γ is more than 1. There is no structural phase transition or optical anisotropy across T_m in relaxor ferroelectrics.

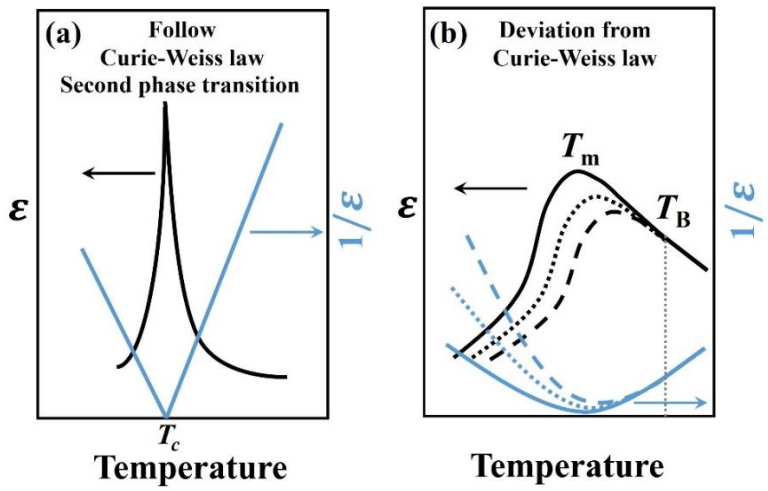

Figure 1.10 Dielectric properties of (a) classic ferroelectricities and (b) relaxor ferroelectricities.

Different possibilities for dielectric constants versus temperatures in relaxor ferroelectrics are shown in Fig. 1.11 [50]. In the range [T_B, T_m] the dielectric constants follow the revised Curie-Weiss law and exhibit a strong frequency dispersion. The nonergodic relaxor (NR) is formed below the freezing temperature (T_f). Fig. 1.11(b) shows the temperature dependence of dielectric constants of relaxor ferroelectrics with a diffused relaxor-to-ferroelectric phase transition. The ergodic relaxor is formed at the range [T_C, T_B]. The dielectric constants show a continuous variation across T_C and the ferroelectric phase is formed below T_C. Fig. 1.11(c) illustrates the dielectric properties of relaxor ferroelectrics with a sharp relaxor-to-ferroelectric phase transition. Different from Fig. 1.11(b), the dielectric constants in Fig. 1.11(c) change incontinously across T_C.

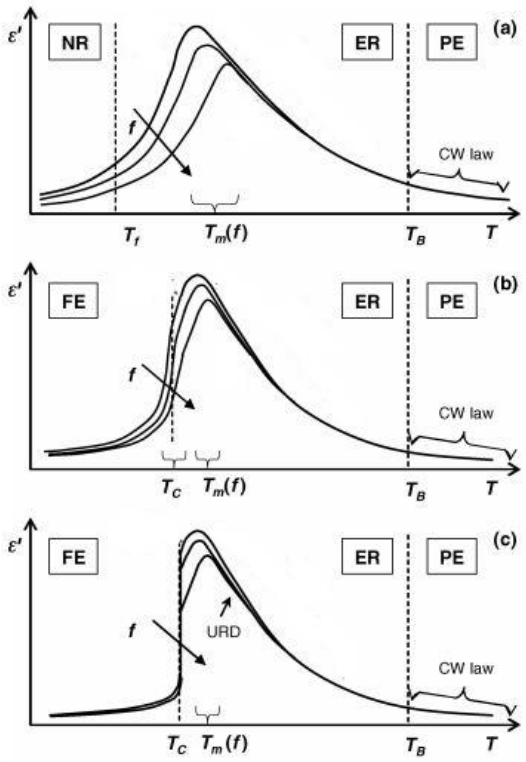

Figure 1.11 Different possibilities for the temperature evolution of dielectric properties in relaxor ferroelectricities, (a) canonical relaxor, (b) relaxor with a diffuse relaxor-to-ferroelectric phase, (c) relaxor with a sharp relaxor-to-ferroelectric phase [50].

1.4 Electric field-induced strain of ferroelectric ceramics

Inorganic ferroelectric materials are able to extend or shrink if a certain press or electric field is applied. The relation between the strain and the applied electric field is given below [25]:

$$S_{ij} = g_{kij}E_k + Q_{ijkl}E_kE_l + \cdots \quad \ldots(1.6)$$

Here i, j, k, l =1, 2, 3, g_{kij} represents the piezoelectric coefficient, Q_{ijkl} stands for the electrostrictive coefficient. Higher order effects are small and therefore were omitted. Fig. 1.12 shows the strain in classic ferroelectric ceramics, which is in the butterfly-pattern under the external electric field [51]. The AG range means the negative strain. GH，HC and HA parts show the positive strain. Electric field-induced strain in ferroelectric materials results from the inversive piezoelectric effect, electrostriction, switching of non-180° domains and so forth. If there is a phase

transition for ferroelectric materials under the electric field, it will also contribute to the strain.

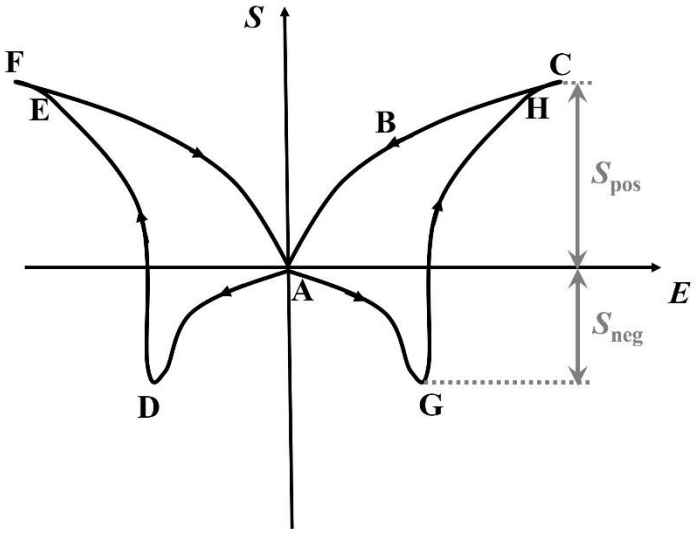

Figure 1.12 Bipolar strain-electric field (*S*-*E*) loop of classic ferroelectric materials.

1.4.1 Inverse piezoelectric effect

The inverse piezoelectric effect reflects the displacement induced by the distortion of lattices when positive and negative charge centers in the ferroelectric ceramics align with the applied electric field. The inverse piezoelectric effect exists with the direct piezoelectric effect together. The strain is proportional to the electric field for the inverse piezoelectric effect, the equation as follows [25]:

$$S = dE \qquad \ldots(1.7)$$

Where, d means the internal piezoelectric coefficient. As for classic ferroelectric materials, strain and the electric field meet the linear relation only in the low electric field, indicating the internal piezoelectric response. When the applied electric field is increased, switching of domains will induce the external piezoelectric response and broaden strain hysteresis may.

1.4.2 Electrostrictive effect

Electrostriction is a secondary coupling effect represented by a quadratic relation

between strain and electric field intensity. The strain from the electrostriction effect is traduced by the following equation [52]:

$$S_3 = Q_{33}{P_3}^2 = Q_{33}{\varepsilon_{33}}^2 E^2 \quad \ldots(1.8)$$

Where Q_{33} represents the electrostrictive coefficient, is not related to phase structures of ferroelectric materials, but closely related to the degree of cations arrangement within materials. In general, the electrostrictive coefficient appears larger in relaxor ferroelectrics compared to classical ferroelectric materials. As an example, PMN-PT relaxor ferroelectrics have large electrostrictive coefficients reaching 10^{-2} m^4/C^2 and then contributing to larger strains [53]. Ferroelectric materials with large electrostriction coefficients have fast responses to the applied electric field and show tiny hysteresis loops.

1.4.3 Electric field-induced phase transition

Crystal distortions occur when external electric field induces a phase transition in ferroelectric structures, which can further generate strains. This process is called the electric field-induced phase transition and can be classified into reversible and irreversible one. The reversible process represents the materials that can recover to their initial state even when the applied electric field is removed. The irreversible electric field-induced phase transition takes place in the beginning if an external electric field is applied. After an initial stage, since the phase of materials has already been altered, an additional electric field didnt cause further effects in the material. The reversible process occurs in relaxor ferroelectric-classical ferroelectric, ferroelectric-ferroelectric (such as rhombohedral-tetragonal, tetragonal-monoclinic), and antiferroelectric-ferroelectric electric field-induced phase transition. It has been found that reversible process can also be induced in textured KNN ferroelectric ceramics under an external electric field, shown in Fig. 1.13 [25]. In the poling process, the intermediate Monoclinic (M) phase serves as a bridge which facilitates the polarization rotation between the rhombohedral (R) $[111]_R$ and orthorhombic (O)

$[101]_O$ polar axes, leading to the enhanced piezoelectric responses [25]. This material show structural phase change from R-O phases to O phase under the electric field. As the "M" phase is unstable, it disappears under high electric fields. This electric field-induced phase transition makes the sample easier to be poled and then contributing to larger strains.

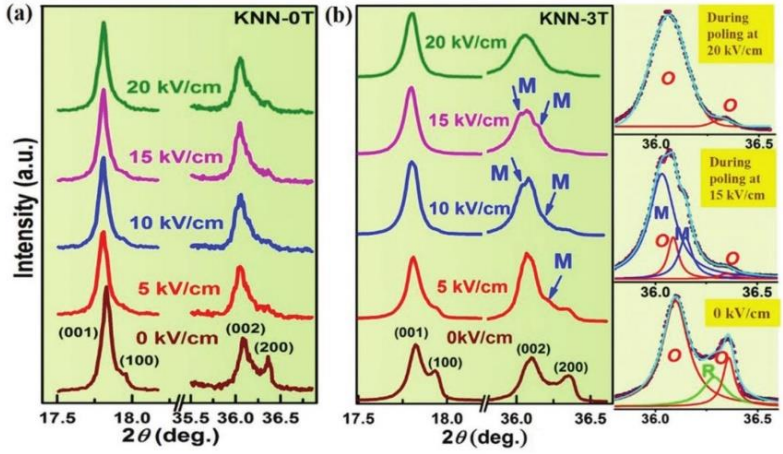

Figure 1.13 In situ synchrotron X-ray diffraction patterns of (a) untextured and (b) textured KNN ceramics under various electric fields [25].

Moreover, the strain value induced from the transformation of an anti-ferroelectric to a ferroelectric phase is tremendously higher than that caused by pure inverse piezoelectric effect or electrostrictive effect. Fig. 1.14 correlates the electric field-induced strain of $PbNbZrSnTiO_3$ ceramics, where the strain value achieves its maximum of 0.3% [54]. This kind of electric field-induced phase transition is usually accompanied with the emergence of memories. It means, the ferroelectric state can still be retained and it cannot recover to the initial anti-ferroelectric state even though the applied electric field is canceled. This special ferroelectric state can only be wiped off through applying an extra low electric field. The larger strain stemming from the anti-ferroelectric phase to the ferroelectric phase makes this kind of materials being promising to apply in actuators.

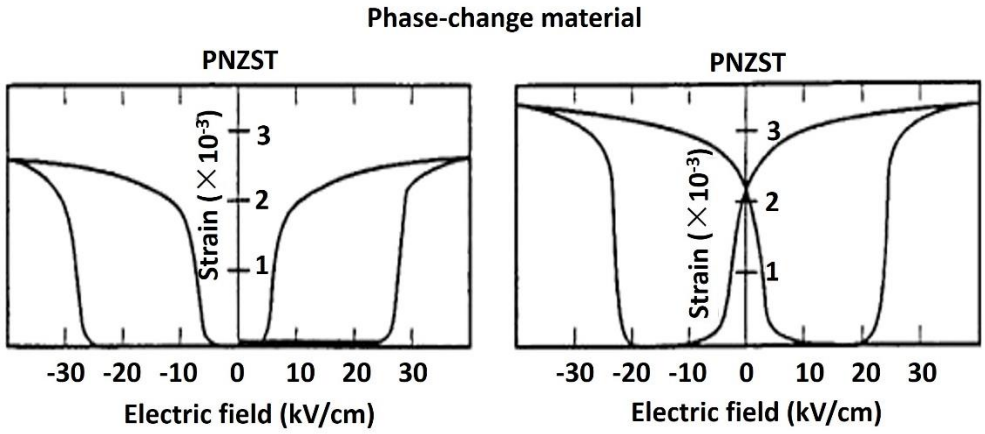

Figure 1.14 Electric field-induced strain of phase-change $PbNbZrSnTiO_3$ material [54].

1.4.4 Contribution of non-180 ° ferroelectric domains

Switching of non-180 ° domains could contribute to a large electric field-induced strain due to the exchange of non-equal crystallographic axes [38]. Such strain may be one or two orders of magnitude larger than the small linear strain stemming from the inverse piezoelectric effect. When the electric field is not high, some non-180 ° domains can recover to the initial state after removing the electric field, which are called the rotation of reversible non-180 ° domains. In contrast, some non-180 ° domains cannot recover to their initial state due to the large angle of the rotation, which are called as the irreversible non-180 ° domains. These two kinds of non-180 ° domains both increase the strain of materials. The former increases the hysteresis of strain, while the latter reduce is prone to reduce it. In the accepter-doping ferroelectric materials, inner defect dipoles could influence the rotation of ferroelectric, especially non-180 ° domains. Defect dipoles in the unpoled materials would pin the rotation of non-180 ° domains, resulting in the low electric field-induced strain. Defect dipoles in the poled materials are aligned with the electric field, which establish an internal bias electric field E_i, resulting in the offset bipolar strain and polarization. It was explained in Chapter 1.2.2.

1.5 Texturing of ferroelectric ceramics

Texturing is a process that makes the polycrystalline grains growing along a specific orientation. In textured ferroelectric ceramics, the introduced anisotropy by the

preferentiel orientation improve the ferroelectric performances as hereafter summarized.

1.5.1 Performances in texturation ferroelectric ceramics

In view of the rapid progress of the technology needs, piezoelectric performances are currently subject of improvments. The piezoelectric effect is highly correlated to the crystal structure where the anisotropy is involved and ensures optimized piezoelectric responses being privilegied along specific orientation. The use of single crystals is an effective way to upgrade the piezoelectric parameters but the critical conditions required for their synthesis limit their application. An alternative approach to compete with the performances of single crystals can be devoloped by using textured ceramics [55, 56].

In the 1970s, a first report was dedicated to the observation of the anisotropy in Al_2O_3 ceramics by using the electronic microscope technique. One decade later, Matsuzawa et al. reported the anisotropic growth of single crystals with the templated grain growth method. The process was performed by incorporating the crystal melt with "crystal seeds" to induce variation in growing velocity on different crystalline facets [57]. By introducing spiny α-Al_2O_3 grains, Brandon et al. prepared textured Al_2O_3 ceramics with the advantages of thermal and seismic resistances [58]. On the other hand, the template grain growth method (TGG) was also exploited to synthesize textured ceramics, which was applied as a patent by Messing et al. [59]. The authors have used this method to synthesize PMNT textured ceramics possessing superior d_{33} up to 1150 pC/N, i.e.1.2~1.5 folds higher than the normal counterparts [60]. Thus, texturing has been considered as an effective solution to enhance the behaviors of ferroelectric ceramics.

From then on, TGG have been improved by other groups and succed to realize several excellent textured ceramics, suh as $(Bi_{0.5}Na_{0.5})TiO_3$-$(Bi_{0.5}K_{0.5})TiO_3$, $Ca_2Bi_4Ti_4O_{15}$ and $Bi_4Ti_3O_{12}$ textured ceramics [61-63]. In 2004, Saito et al. prepared highly performant <001> $KNaNbO_3$ piezoelectric ceramics by using RTGG method together with doping, and exploiting the perovskite plate-like $NaNbO_3$ templates [64]. The modified

ceramic exhibits piezoelectric constant d_{33} at 412 pC/N, being almost equivalent to the PZT systems. By using the RTGG method, the synthesis of $Na_{0.5}Bi_{0.5}TiO_3$–$BaTiO_3$ as textured ceramics improve the piezoelectric constant d_{33} being twice higher that the use of the conventional solid-state method. The microstructure for the textured ceramics was also analyzed by using TEM and AFM. Yan et al. performed a work on Mn doped <001> $Pb(Mg_{1/3}Nb_{2/3})$-$PbZrO_3$-$PbTiO_3$ systems, which revealed the piezoelectric constant d_{33} at 750 pC/N [65]. A superior d_{33} value at 1000 pC/N was achieved in <001> $Pb(Mg_{1/3}Nb_{2/3})O_3$-$PbTiO_3$ textured ceramics [66]. It is worth noting that $BaTiO_3$ templates which were used in the ratio only limited at 1%, induce a high orientation of 98%. Recently, a d_{33} value of 824 pC/N and kp of 0.81 was determined on <001> $Pb(In_{1/2}Nb_{1/2})O_3$-$Pb(Mg_{1/3}Nb_{2/3})O_3$-$PbTiO_3$ ceramics with the use of $BaTiO_3$ templates. This important progress on piezoelectric properties underlines that textured ferroelectric ceramics offer a promising competitors to the performances of ferroelectric single crystals. However, a crucial drawback lies in the Curie temperature which remains relatively low. Yan et al. prepared $PbTiO_3$ textured ceramics [5] with a high Curie temperature of 364 ℃ but d_{33} was found to be less than 100 pC/N. The current achievement on textured ferroelectric ceramics suggests that this route is still far from practical application.

1.5.2 Characteristics of templates

The two basic requirements for templates in the TGG process consist in (1) platelets or spiny structures and (2) the pure phase of templates. Thus, anisotropic $BaTiO_3$ templates with pure phase can be obtained by optimizing the experimental parameters, such as annealing temperature, washing times, reactive time [67, 68].

$BaTiO_3$ templates are prepared by the topochemical reactive method. In this approach, Bi_2O_3 reacts with TiO_2 to form the precursor $Bi_4Ti_3O_{12}$ with Aurivillius perovskite structures. Fig. 1.15 illustrates the process from the precursor $Bi_4Ti_3O_{12}$ to the realization of $BaTiO_3$ templates [69]. In the first stage, the perovskite phase forms by nucleation on the precursor $Bi_4Ti_3O_{12}$ surface. The growing perovskite crystallites do not maintain epitaxy with the precursor phase, and slightly misalign from the

Aurivillius parent structure. This process is topotactic and is completed with a short time less than 30 min. In the second stage, the aligned crystallites from the first stage recrystallize and sinter to form dense perovskite-phase platelets. This process holds for a long duration about 2-6 hours. If the recrystallization is correctly achieved, the perovskite platelets may be single crystals. Alternatively if an initial misalignment occurs when forming the perovskite structures, the final platelets may be polycrystalline with the high anisotropy.

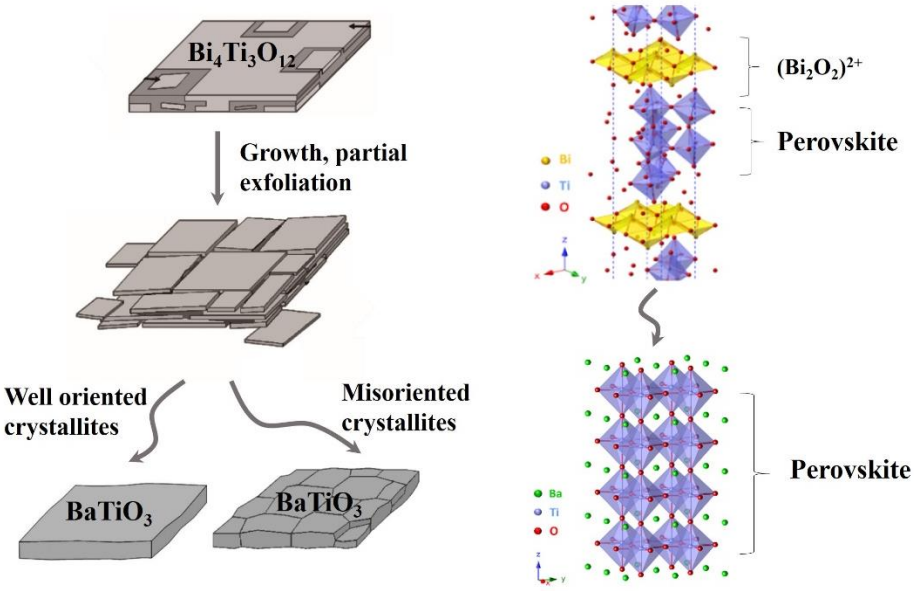

Figure 1.15 Schematic of preparing $BaTiO_3$ templates with the topochemical conversion reaction [69].

The ceramic powders are called matrix in the grain growth process. According to the correlation between templates and the matrix, the templates can be classified into two distinct kinds, similar-feature templates and different-feature templates. Similar-feature templates have the same components, phase and the similar lattice parameters as for the matrix. Similar-feature templates share the same composition and crystal structures with the matrix in the grain growth process. In this case, the grain growth obeys the Ostwald Ripening mechanism shown in Fig. 1.16, which means that the larger grain growth depends on the exhaustion of smaller matrix crystals. While for the different-feature templates, there is a difference in the composition between templates and the matrix, but their crystal structure is the same

or the lattice parameters are similar. The nucleation of the matrix can take place on the surface of templates as an epitaxial mechanism. With the matrix growth, its morphology tends to align with the templates in order to achieve the texturation. In general, textured ceramics prepared by similar-structures templates may show higher piezoelectric performances, although their application is limited. Note however, that the usual templates used for inorganic ferroelectric ceramics consist in $BaTiO_3$, $SrTiO_3$, or $NaNbO_3$ compounds. The precursors of $BaTiO_3$ templates are $Bi_4Ti_3O_{12}$, $BaBi_4Ti_4O_{15}$ [70, 71] while $SrBi_4Ti_4O_{15}$ is used for $SrTiO_3$ templates [72]. The precursors of $NaNbO_3$ templates are $Na_{0.5}Bi_{0.5}TiO_3$ and $Bi_{2.5}Na_{3.5}Nb_5O_{18}$ [73, 74].

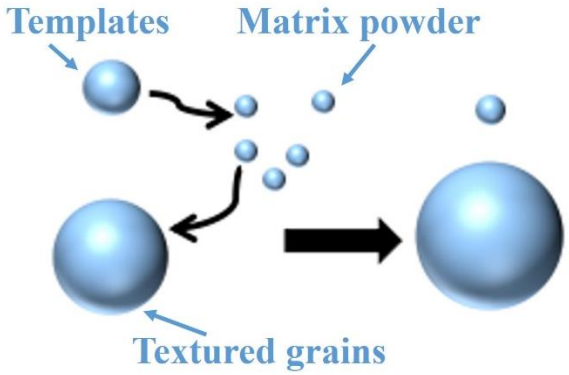

Figure 1.16 Model of Ostwald ripening

1.5.3 Reactive templated grain growth method

Fig. 1.17 is the schematic mechanism for the preparation of textured ceramics by the reactive templated grain growth method [75]. In prior to the synthesis, templates must be chosen in function of the nature of the ceramics. In the first step, the matrix density increases rapidly limiting the porosity and then reinforces the contact between the matrix and the templates. Meanwhile, the in-situ reaction between templates and matrix takes place to produce the solid solution. In the second stage, the templates grow rapidly by consuming matrix, where the growing velocity along the thickness is faster than that along the lengthwise direction. Cubic crystalline grains are finally obtained based on this routine. However, the growing velocity tends to be reduced when boundaries in templates intersect. The templates are grow further by gradually consuming the matrix. Ultimately, textured ceramics along the orientation of

templates are obtained by long-time sintering [75].

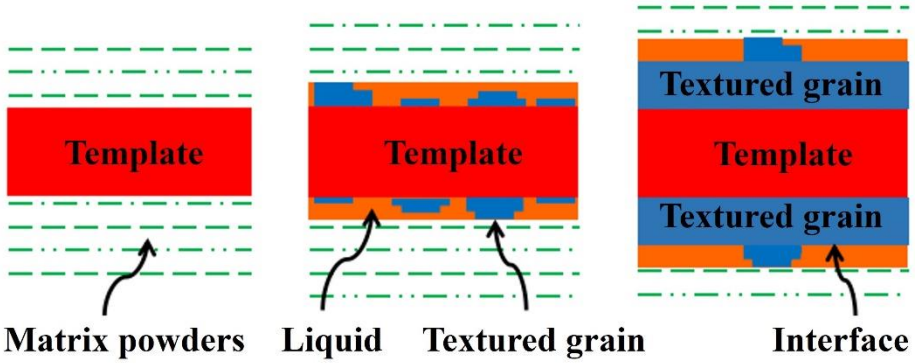

Figure 1.17 Schematic illustration of synthesizing textured ceramics with the reactive templated grain growth method.

1.6 Advances in ferroelectric ceramics

The ferroelectric ceramics can be classified into lead-contained and lead free species with respect to their compositions. In this section, an overview on the advances in the area ferroelectric ceramics is outlined on these two systems.

1.6.1 Advances in lead-based ferroelectric ceramics

$Pb(Zr_{1-x}Ti_x)O_3$ (PZT) ceramics are the most commonly applied ferroelectric materials. Among all the counterparts, $Pb(Zr_{1-x}Ti_x)O_3$ systems revealed for instance the best performance with the composition of $x \approx 0.48$ where the MPB occurred. Generally, ion substitution, binary and ternary combination are developed to promote the properties of PZT ceramics. Among all the doping systems, $(Pb,La)(Zr,Ti)O_3$, $(Pb,Sr)(Zr,Ti)O_3$, $(Pb,Ba)(Zr,Ti)O_3$, $Pb(Zr,Ti, Sn)O_3$ are relevant materials. Binary and ternary combination is also manifested to be an adequate solution to enhance piezoelectric properties of PZT based ceramics. Many reports were focused on the composite materials of $Pb(Mn_{1/3}Nb_{2/3})O_3$-$Pb(Zr,Ti)O_3$ (PMN-PZT), $Pb(Zn_{1/3}Nb_{2/3})O_3$–$Pb(Zr,Ti)O_3$ (PZN–PZT), $Pb(Ni_{1/3}Nb_{2/3})O_3$–$Pb(Zr,Ti)O_3$ (PNN–PZT). It was reported that PMN-PT relaxor ferroelectrics presented relatively high strain and piezoelectric constant, for doped samples with rare-earth element Sm that exhibited d_{33} at 1500 pC/N [28, 76]. Nevertheless, the low T_C and instability at high temperature suppressed its application under high temperature condition. Compared with lead-free $BaTiO_3$

ceramics, the lead-contained PZT ceramics show approximately double piezoelectric constants and exhibit a better high-temperature stability. The advantages of PZT also reflect the difficult depolarization at high temperatures. Therefore, PZT ceramics dominate in the field of piezoelectric ceramics.

1.6.2 Advances in lead-free ferroelectric ceramics

With the intensification of people's awareness in environment issues and to meet the requirement of sustainable development, a great interest has been devoted to lead-free ferroelectric ceramics. The common known lead-free ferroelectric ceramics include $KNaNbO_3$ (KNN), $BiNaTiO_3$ (BNT), $BaTiO_3$ (BT) and bismuth-layer lead-free systems. The former three systems have already showed relatively high ferroelectric properties. Different from lead-contained ferroelectric ceramics, the above-mentioned lead-free systems still possessing disadvantages, such as high coercive fields, low density and so forth. In order to address these limitations, many efforts have been done in addition to sintering optimization, ion-doping and modification of synthesis protocols [1, 2, 77]. Lead-free $0.96(Na_{0.52}K_{0.48})(Nb_{0.95}Sb_{0.05})O_3$-$0.04Bi_{0.5}(Na_{0.92}K_{0.18})_{0.5}ZrO_3$ product synthesized by Wang et al. show a high piezoelectric constant and high T_C, at 490 pC/N and 227 ℃, respectively [78]. On the other hand, based on a previously reported work in $Ba(Ti_{0.8}Zr_{0.2})O_3$-$(Ba_{0.7}Ca_{0.3})TiO_3$, lead-free materials on $_{0.67}Bi_{1.05}(Fe_{1-x}Ga_x)O_3$-$_{0.33}BaTiO_3$ were prepared by Lee and co-workers via the traditional solid-state method and appropriate annealing. In this work, the phases of the samples close to MPB exhibit d_{33} coefficient surpassing 400 pC/N and T_C over 300 ℃ [6, 7]. This result attracted the interest to the $BiFeGaO_3$-$BaTiO_3$ lead-free systems where Ga doping can be used to adjust the lattice structure. The obtained ceramics presented a tetragonal phase with a high c_T/a_T ratio and exhibited both high piezoelectric constant and T_C as well. Thus, lead-free ferroelectric ceramics are environment-friendly for concrete applications and can meet the concept of sustainable development. Therefore, it is of great societal and scientific significance to further exploit and investigate lead-free ferroelectric ceramics to achieve higher performances for innovative technologies.

Chapter 2 Experimental procedures and characterization techniques

2.1 Processing of PZT and $BiFeAlO_3$-$BaTiO_3$ ferroelectric materials

In this dissertation, PZT and $BiFeAlO_3$-$BaTiO_3$ ceramics were prepared by the conventional solid-state method. The steps of the synthetic route are provided in Fig. 2.1, and the used chemical components are presented in Tab. 2.1. The raw materials were precisely calculated according to the stoichiometric ratio. Then powders were treated with calcination, pressing, sintering in series to obtain high-density ceramics. After that, the microstructure and physico-chemical features were analyzed along with the involved mechanism leading to the observed properties.

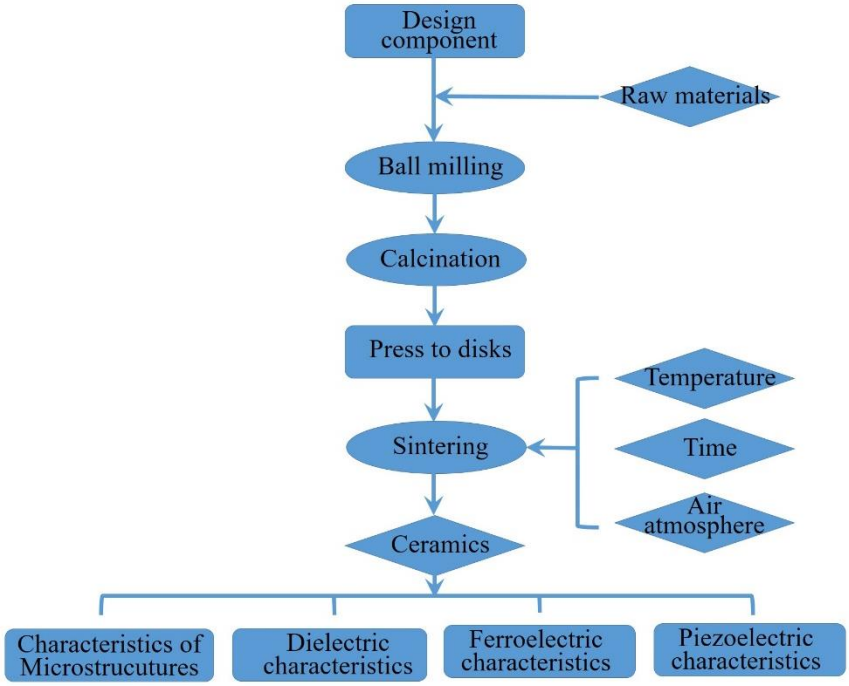

Figure 2.1 Synthetic process of preparing PZT and $BiFeAlO_3$-$BaTiO_3$ ceramics with the solid-state method.

Table 2.1 Chemical components for preparing PZT and $BiFeAlO_3$-$BaTiO_3$ ceramics.

Chemical components	Categories	Purity	Place of production
Pb_3O_4	A.R	99%	Sinopharm chemical reagent company
$SrCO_3$	A.R	99.95%	Aladdin chemical reagent company
La_2O_3	A.R	99.99%	Aladdin chemical reagent company
ZrO_2	A.R	99.84%	Tianjin oumi chemical reagent company
TiO_2	A.R	99.48%	Sinopharm chemical reagent company
Fe_2O_3	A.R	99.9 %	Aladdin chemical reagent company
Bi_2O_3	A.R	99.70%	Sinopharm chemical reagent company
Al_2O_3	A.R	99.5%	Sinopharm chemical reagent company
$BaCO_3$	A.R	99.8%	Sinopharm chemical reagent company
CH_3CH_2OH	A.R	-	Shanghai lingfeng chemical reagent company

For a completed synthesis route, detailed experimental parameters are provided below:

(1). Dry raw materials: All raw materials were thoroughly dried at 120 ℃ for 6 h to evaporate adsorbed water.

(2). Weight: All raw materials were carefully weighed according to the stoichiometric ratio.

(3). Ball milling: The mixtures were ball milled for 10 h at 350 r/min.

(4). Pressed into bulk: The obtained powders after milling were subsequently pressed into the bulk with Φ55 mm.

(5). Calcination: The resultant bulk was heated at the target temperature for 2 h with a partial solid-state reaction. The ramping rate was 4 ℃/min.

(6). Ball milling for the second time.

(7). Pressed into pellets: Powders were mixed with 8 wt.% PVA, and then were

pressed into disks with Φ12 mm.

(8). Remove organics: Disks were treated at 550 ℃ for 6 h to eliminate the residual PVA with a very slow heating rate (0.5 ℃/min).

(9). Sintering: The disks were sintered at a given temperature for 2 h to achieve high densities.

(10). Coated electrode: The ceramics after sintering were then purified and characterized for phases and microstructures. If electric measurements need to be performed, the ceramics had to be processed into uniform size with the thickness of 0.8 mm, which were subsequently ultrasonically cleaned and coated with Ag layer acting as electrodes.

(11). Silver electrode firing: An extra thermal treatment was necessary at 720 ℃ for 30 min to burn out the useless organics in silver electrodes.

(12). Poled: In order to obtain piezoelectric parameters such as mechanical quality factors Q_m, electromechanical coupling coefficient K_p, the ceramics had to be poled in the DC electric field. During the poled process, samples were placed in silicone for protection. The sample was poled at 100 ℃ for 30 min.

2.2 Processing of $BaTiO_3$ templates and textured $BiFeGaO_3$-$BaTiO_3$ ceramics

$BaTiO_3$ templates were first synthesized by three-step molten salt methods, which was then incorporated into the textured $BiFeGaO_3$-$BaTiO_3$ ceramics via tape casting. The exact synthetic route is provided in Fig. 2.2, and chemical components are presented in Tab. 2.2. In prior to the preparation of templates, the raw materials were precisely calculated referring to the stoichiometric ratio. The textured materials prepared by the reactive template grain growth method. After that, the microstructure and characteristic parameters were analyzed and compared to the untextured ceramics.

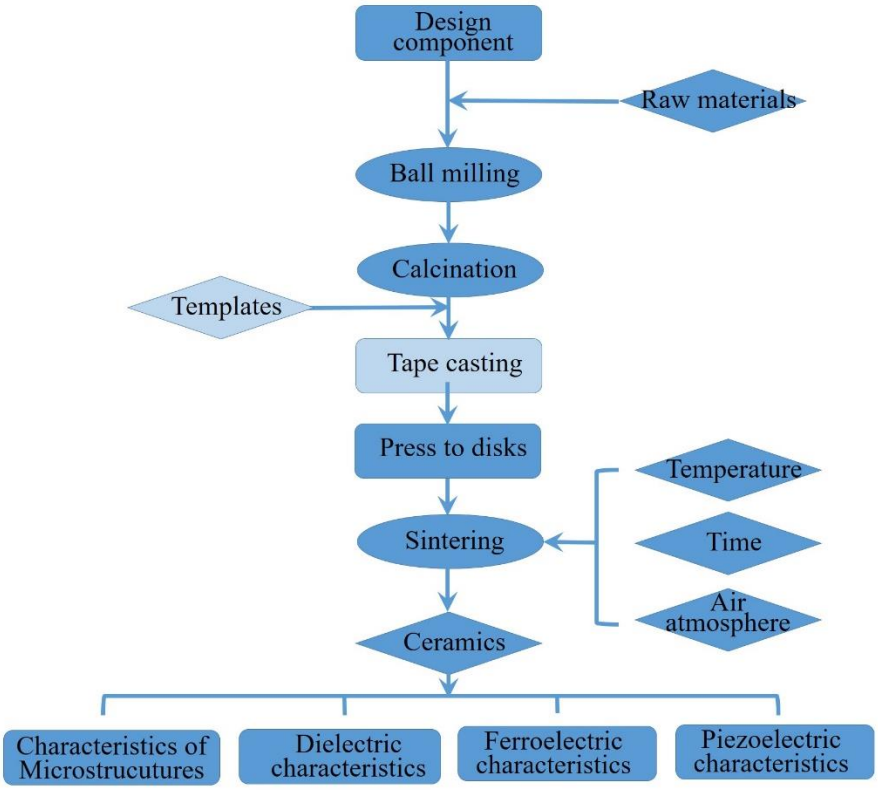

Figure 2.2 Process of synthesizing textured $BiFeGaO_3$-$BaTiO_3$ ceramics.

Table 2.2 Chemical components for preparing textured $BiFeGaO_3$-$BaTiO_3$ ceramics.

Chemical components	Categories	Purity	Place of production
Bi_2O_3	A.R	99.7%	Sinopharm chemical reagent company
$BaCO_3$	A.R	99.8%	Sinopharm chemical reagent company
Fe_2O_3	A.R	99.9%	Aladdin chemical reagent company
Ga_2O_3	A.R	99.48%	Sinopharm chemical reagent company
TiO_2	A.R	99.48%	Sinopharm chemical reagent company
PVA	A.R	-	Sinopharm chemical reagent company
Organic binder	-	-	Guangzhou Shenzhou optical-electric company
$CH_3CHOCH_2CH_3$	A.R	-	Shanghai lingfeng chemical reagent company

For the completed synthesis procedure, the different steps are as follows:

(1). First-step molten salt reaction: Stoichiometric Bi_2O_3 and TiO_2 were homogenized with NaCl/KCl in equivalent weight using an agate pestle and mortar. The reaction mixtures were then loaded into an oven to anneal at 1120 ℃ for 1 h. Sheet-like $Bi_4Ti_3O_{12}$ precursor was subsequently obtained through the following equation:

$$2Bi_2O_3 + 3TiO_2 \xrightarrow{NaCl+KCl} Bi_4Ti_3O_{12} \quad \ldots(2.1)$$

(2). Second-step molten salt reaction: Stoichiometric $Bi_4Ti_3O_{12}$ precursor and $BaCO_3$, TiO_2 reactants were mixed homogeneously with $BaCl_2$/KCl in equivalent weight prior to the reaction. The mixtures were then annealed at 1080 ℃ for 1 h to prepare $BaBi_4Ti_4O_{15}$ precursor, as detailed below:

$$Bi_4Ti_3O_{12} + BaCO_3 + TiO_2 \xrightarrow{BaCl_2+KCl} BaBi_4Ti_4O_{15} \quad \ldots(2.2)$$

(3). Third-step molten salt reaction: As-obtained powders were washed to isolate $BaBi_4Ti_4O_{15}$, which was subsequently homogenized with $BaCO_3$ and the reactants were heated to 950 ℃ for 3 h, with the incorporating of KCl in an equivalent weight. After the reaction, sheet-like $BaBi_4Ti_4O_{15}$ was transformed into $[001]_c$ oriented $BaTiO_3$ (BT) template that still retained sheet feature. The reaction equation is presented below:

$$BaBi_4Ti_4O_{15} + 3BaCO_3 \xrightarrow{KCl} 4BaTiO_3 + 3CO_2 + 2Bi_2O_3 \quad \ldots(2.3)$$

(4). Dry raw materials → weight → Ball milling → Pressed into bulk → Calcination → Ball milling in the second time. Routines in details refer to the Chapter 2.1.

(5). Tape casting: The obtained BFG-BT powders were homogenized with 5 wt.% $BaTiO_3$ with organic solution. The mixtures formed the belt with a thickness of 60 μm through the tape casting subsequently with the velocity of 0.5 m/min.

(6). Pressed into disks: When the film belt was dried, it was further cut, stacked and positioned at 75 ℃ for 30 min under 70 MPa. After these treatments, samples were stacked again and tailored into disks with Φ12 mm.

(7). Remove organics → Sintering → Coated electrodes → Silver electrode firing. Routines in details refer to the Chapter 2.1.

2.3 X-ray diffraction (XRD)

XRD (X-ray diffraction) technique can be used to characterize crystal structures of ferroelectric materials. In this dissertation, two kinds of XRD experiments were performed based on Rigaku D/max 2550 V and Empyrean-Panalytical. The former was used for analyzing normal phase structures, whereas the latter was utilized to refine crystal parameters. As for Empyrean-Panalytical, the wavelengths of Cu Kα1 and Cu Kα2 were 0.15406 and 0.15444 nm, respectively. The working voltage was 40 kV with the current of 30 mA, and the scanning range (2θ) was from 20-100 °at a rate of 1-4 °/min and step length of 0.02 °. When the incident X-ray with the wavelength λ irradiates the crystalline sample, the diffraction by the crystallographic planes (hkl) occurs according to the Bragg relation $2d_{hkl}\sin(\theta) = n.\lambda$. The XRD pattern is composed by the diffraction lines associated to the (hkl) planes of the crystalline structure as function of the angle θ between the incident direction and the crystallographic planes. Different programs are used for the refinement of the XRD patterns such as MAUD (Materials Analysis Using Diffraction) which is based on the well-known Rietveld method. The simulations of the diffraction patterns give the relevant structural parameters such as the space group, the unit cell parameters, the co-existence of phases, crystalline quality.

For the textured ceramics in this thesis, the degree of orientation of grains was determined from the XRD pattern by Lotgering method. The Lotgering factor f is defined as the fraction of textured areas. The formula is as follows [79]:

$$f_{h00} = \frac{P-P_0}{1-P_0}, P = \frac{\sum I(h00)}{\sum I(hkl)}, P_0 = \frac{\sum I_0(h00)}{\sum I_0(hkl)} \quad \ldots(2.4)$$

where I and I_0 are intensity of the diffraction lines (hkl) of textured and untextured specimens, respectively.

2.4 Scanning electron microscopy (SEM)

Scanning electronic microscopes (SEM) of KYKY-EM3200 and Carl Zeiss Auriga 60 were employed to measure the morphologies of the samples. An X-ray energy-dispersive spectrometer (EDS) mounted on the SEM was used to analyze the distribution of chemical elements. During the working process, all the electrons are first provided by an electron gun and then converge in a 1 μm cross point under the function of accelerating voltage. The electrons are subsequently focalized by moving through electromagnetic lenses and the resultant electron beam is then focused on the surface of the sample with diameter of 0.5-3 nm. By scanning the electron beam on the sample surface through a coil in the scanning apparatus, another coil is also sweeping simultaneously the screen. The secondary electronic information can be received by a detector which transformed the electronic information into visual spot with certain brightness. Based on this process, the surface features of the sample are proportionally presented in observable information such as surface state of the sample.

In addition to the conventional equipment, SEM can be also equipped with highly effective suspension system to avoid the disturbance from environment. The gun pipe is made of tungsten filament, and the accelerating potential used here is 30 kV. The magnifying power can be adjusted from 5 to 300000, and the SEM contains three kinds of working manners, including composite mode, morphology mode and shadow mode.

2.5 Transmission electron microscopy (TEM)

High-resolution transmission electron microscope (HR-TEM, JEOL ARM200F) with

the working voltage at 200 kV was employed to observe the morphology of domains. In a typical experiment, the electron gun launches electron beam which then passes through collecting lens and irradiates on the sample surface. The electron beam can pass through the sample and the information is then imaged on the screen with the assistance of objective lens. For the operation of selected area electron diffraction (SAED) characterization, selected gratings with differences in apertures are used to choose target area that are subsequently irradiated by parallel electron beam to acquire information on the lattices.

2.6 ^{57}Fe Mössbauer method

^{57}Fe Mössbauer spectroscopy is a versatile technique which provides precise information about chemical, structural and magnetic properties of a material. The technique is based on the γ-ray emission by a source and its absorption by the investigated sample and this process contribute to create the "Mössbauer effect". During a typical Mössbauer experiment, transitions are induced between the nuclear energy level of isotopes through the process of emission and absorption of γ rays. If emitting and absorbing nuclei are in identical sites with isotropic environment, the transition energies are then equivalent and a single line is able to be observed in Mössbauer spectrum shown in Fig. 2.3. However, in most cases, the environment of the nuclei in samples is different from the source. The hyperfine interactions between the nucleus and its environment will change the energy of the nuclear transition. To detect this phenomenon, it is necessary to change the energy of γ rays in the source. By the uses of the Doppler effect and an oscillating source, the energy of γ rays can be modulated precisely in the Mössbauer spectroscopy [80].

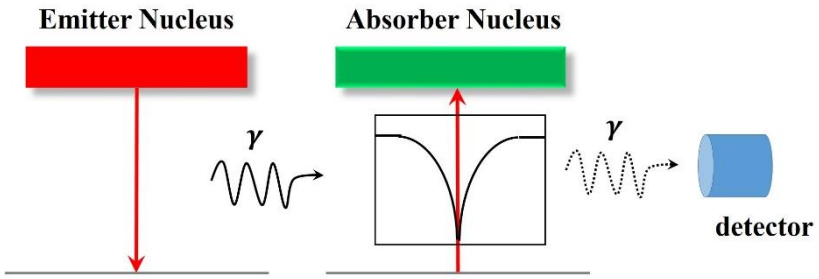

Figure 2.3 Mössbauer spectrum with a single absorption line [80].

Typically, there are three methods to modify energy levels in the absorbing nuclei by their environment: the Isomer Shift, Quadrupole Splitting and Magnetic Splitting. Based on these methods, hyperfine interactions between samples and their surrounding environment can be analyzed profoundly by the Mössbauer spectroscopy. In this dissertation, Mössbauer spectrum was used to analysis the structural disorder of Fe^{3+} at the B site in $BiFeAlO_3$-$BaTiO_3$ systems.

2.7 Ferroelectric measurements

The ferroelectric measurements were carried out by the ferroelectric analyzer (aixACCT TF-2000) equipped with exterior heating apparatus and laser accessories. The polarization-electric field (*P*-*E*) hysteresis loop can be measured by the Sawyer-Tower circuit by the ferroelectric analyzer. The schematic testing circuit for hysteresis loops is depicted in Fig. 2.4. During the test, an exterior potential U was applied on the specimen C_x which was located between two horizontal plates. The linear capacitor C_1 with the relative high capacitance was mounted in series with C_x. The polarization was thus proportional to electric filed and the measurements are made by using the oscilloscope included in the circuit. By using this method, the polarization was recorded versus the electric field.

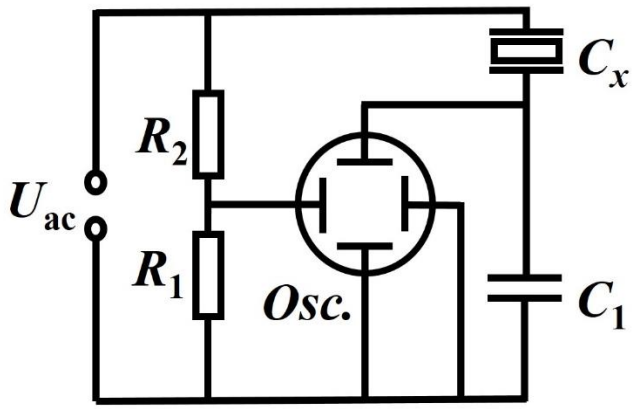

Figure 2.4 Measurement circuit of polarization-electric field (*P*-*E*) hysteresis loops.

The ferroelectric sample was pre-polarized by measuring a complete hysteresis. Then the excitation voltage was kept constant for the relaxation time at a particular voltage. The relaxed quasi-static polarization was determined by driving the capacitor into saturation and recording the current response. By integrating the current response the desired relaxed polarization was calculated as shown in Fig. 2.5. After cycling through a complete hysteresis once again to ensure the same initial condition, the excitation signal was stopped at the next voltage for the relaxation time. The relaxed polarization was determined again as described above. The whole procedure was repeated until a complete quasi static hysteresis loop was recorded.

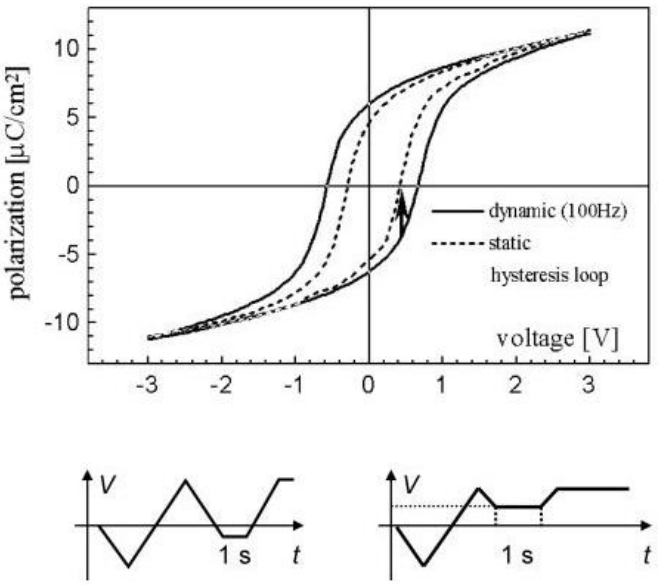

Figure 2.5 Typical polarization-electric field (*P*-*E*) hysteresis loop and the excitation signal before measurement.

The electric field-induced strain was acquired through controlling the displacement of the sample via the laser measurement with a precision down to at 0.01 nm. When a pulsed electric field was applied on the surfaces of the sample, the displacement of the specimen varied with the electric filed. It exhibited the bipolar strain when the bipolar electric field was applied. Generally, the bipolar strain of classic ferroelectric materials is symmetric about the Y-axis. In contrast, when the unipolar electric field was applied, it represented the unipolar strain.

2.8 Dielectric measurements

2.8.1 High-temperature dielectric system

The high-temperature dielectric system was used to estimate dielectric constants and losses of the prepared samples from room-temperature to 700 ℃. Such a system is built in Xi'an Jiaotong University and the main components include impedance analyzer, temperature controller, oven and the computer. The operating frequencies were focused on 0.1 k, 1 k, 10 k, 100 k and 1000 kHz. Upon characterization, the dielectric constant was then calculated by integrating the capacitance into the equation provided below:

$$\varepsilon_r = \frac{Ct}{\varepsilon_0 S} = \frac{4Ct}{\pi\varepsilon_0 d^2} \quad \ldots(2.5)$$

Where ε_0 represents permittivity of vacuum with the value of 8.854×10^{-12} F/m. *C* is the capacitance, *t* and *d* are the thickness and diameter of the sample, respectively. S indicates the area of the ceramic pellet. In a typical calculation process, the thickness and area of all samples were adjusted to the same for better comparison.

2.8.2 Novocontrol broad band dielectric impedance spectrometer

The dielectric characterization was carried out in a Novocontrol Broad Band Dielectric Impedance Spectrometer. This system can be used in a wide temperature

and frequency ranges to evaluate dielectric constants from impedance measurements. The temperature of the system was regulated by using liquid nitrogen, and it could be ranged from -150 ℃ to 300 ℃ and the frequency range can be from 10^{-2} to 10^{7} Hz. There are different analyzers in Novocontrol Broad Band Dielectric Impedance Spectrometer. Among them, the Alpha analyzer (Fig. 2.6) provides the basic functionality in order to operate all measurement interfaces. The setup is composed by the Alpha Analyzer mainframe, sample holder and Active Sample Cell ZGS. Active Sample Cell ZGS includes a sample cell with two parallel electrodes configuration for dielectric, conductivity and impedance measurements on materials. The system is a useful tool to analyze dielectric properties of ferroelectric ceramics.

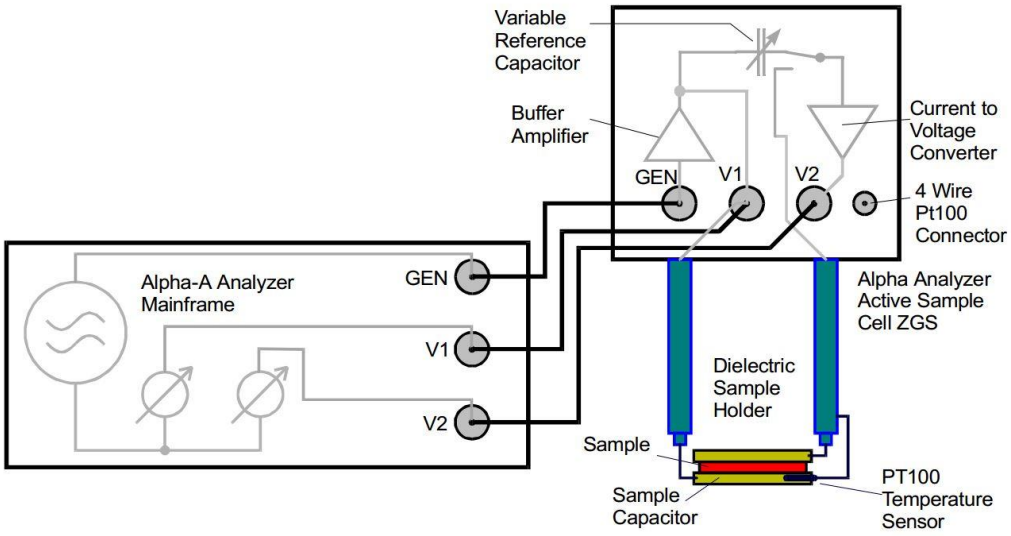

Figure 2.6 Setup of Alpha analyzer on the electric measurement.

2.9 Piezoelectric measurements

The spontaneous polarization of ferroelectric materials is isotropic before polarization and the total polarization is zero. However, after poled, ferroelectric materials exhibit finite polarization. Fig. 2.7 depicts the piezoelectric vibrator and the corresponding current curve as function of the frequency which exhibit maximum and minimum value at characteristic frequencies f_i. The schematic RLC equivalent circuit with resonance and anti-resonance frequencies is provided in Fig. 2.8 and may account for the frequency behavior of piezoelectric ceramics. The variation trend of the

impedance |Z| is consistent with that of the current with the involvement of a maximum and minimum in the curve. Based on this routine, a series of piezoelectric performances can be calculated with equivalent RLC circuits.

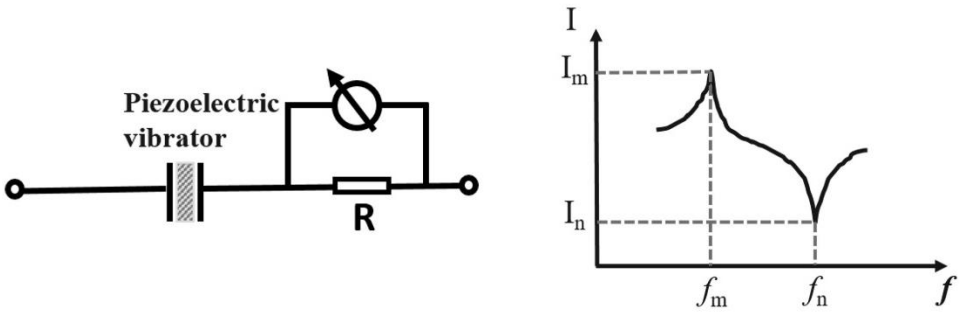

Figure 2.7 The current curve of the piezoelectric vibrator corresponding to frequencies.

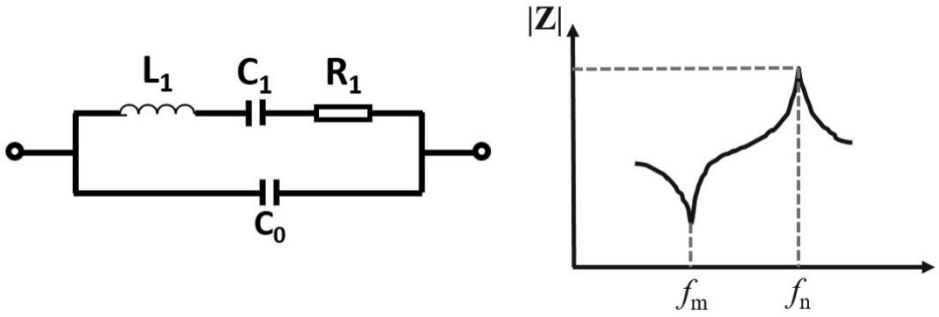

Figure 2.8 The impedance curve of the RLC circuit corresponding to frequencies.

2.9.1 Electromechanical coupling coefficient

Electromechanical coupling coefficient (*K)* measures the conversion between mechanical and electrical energies which can be defined as follows:

$$K = \frac{U_{12}}{\sqrt{U_1 U_2}} \qquad \ldots(2.6)$$

Where U_{12} means the mutual elastic-dielectric energy, U_1 means the density of elastic energies and U_2 is the density of dielectric energies. Vibration of piezoelectric ceramics depend on their shape as illustrated in Fig. 2.9 where different mechanical coupling factors are shape dependent and referred as k_p, k_t, k_{33} and k_{31}.

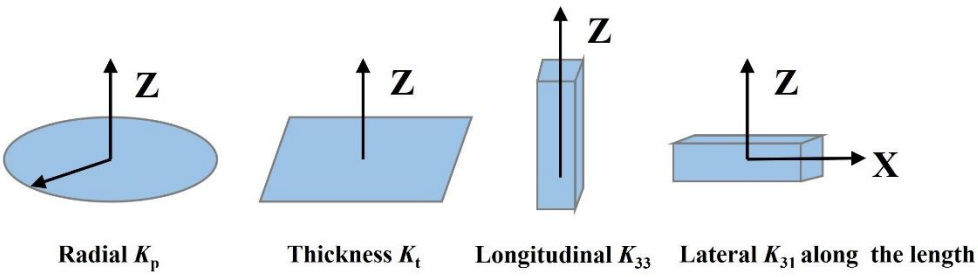

Figure 2.9 Different electromechanical coupling coefficients of piezoelectric ceramics.

In the present work, we will be concerned by k_p and k_t which characterize the considered piezoelectric performances. The calculation of k_p is as follows:

$$k_p = \sqrt{\frac{f_a - f_r}{f_r} \cdot \frac{\eta^2 - (1-\sigma^2)}{1+\sigma}} \quad \ldots(2.7)$$

Where f_a means the anti-resonance frequency. f_r means the resonance frequency. η is related to Poisson's ratio as σ following the relation :

$$\sigma = \frac{5.332 f_r - 1.867 f_{r1}}{0.6054 f_{r1} - 0.1910 f_r} \quad \ldots(2.8)$$

Where f_{r1} means third resonance frequency. The calculation of k_t is as follows:

$$k_t = \sqrt{\frac{\pi f_r}{2 f_a} \cdot tan[\frac{\pi(f_a - f_r)}{2 f_a}]} \quad \ldots(2.9)$$

2.9.2 Mechanical quality factor

Under the AC electric field, piezoelectric ceramics vibrate mechanically. In order to overcome the internal friction, vibrators dissipate part of energies through conduction and polarization relaxation. The mechanical quality factor Q_m characterizes the sharpness of the electromechanical resonance spectrum and is defined as follows:

$$Q_m = 2\pi \frac{W_m}{W_R} \quad \ldots(2.10)$$

Where W_m means the maximum of elastic energies and W_R represents the loss of

mechanical energies every period. Thus, higher Q_m corresponds to small energy loss. The relation between Q_m and the equivalent circuit sketched in Fig. 2.8 is as follows:

$$Q_m = \frac{2\pi f_s L_1}{R_1} = \frac{1}{2\pi f_s C_1 R_1} \quad \ldots(2.11)$$

Which can be also written as follows:

$$Q_m \approx \frac{1}{4\pi R_1 (C_0+C_1)(f_p-f_s)} \quad \ldots(2.12)$$

And

$$Q_m = \frac{{f_a}^2}{2\pi |Z_m| (C_0+C_1) f_r ({f_a}^2-{f_r}^2)} \quad \ldots(2.13)$$

Which may be also simplified as:

$$Q_m = \frac{\beta}{4\pi |Z_m| (C_0+C_1)(f_a-f_r)} \quad \ldots(2.14)$$

The different parameters introduced in the above definitions consist in R_1 which represents the equivalent resistance at resonance and $|Z_m|$ stands for the impedance in resonance. C_0 and C_1 are total and dynamic capacitance in resonance, respectively. β represents the revised coefficient of Bessel, f_p is the frequency of a parallel circuit, f_s means the frequency in series. f_r and f_a are already defined as the resonance frequency, anti-resonance frequency, respectively. If R_1 of the sample is small, there is a relationship about $f_p = f_a$, $f_s = f_r$.

2.9.2 Quasi-static piezoelectric constant

The piezoelectric constant represents the correlation between the mechanical strain and the electric field. The total polarization is zero before poling the ferroelectric ceramics. After poling, the samples exhibit finite values for the quasi-static piezoelectric constants. These parameters are anisotropic and referred in the

piezoelectric tensors as d_{33}, d_{31}=d_{32}, d_{15}=d_{24}.

The quasi-static method can be used to determine directly the piezoelectric constant d_{33}, as shown in Fig. 2.10. When applying a force F_3 on the sample, the charge Q_3 generated by the sample is measured. Compared the charges between the sample and a standard sample reference, the quasi-static piezoelectric constant of the sample is obtained. The equation is as follows:

$$d_{33} = \frac{Q_3}{F_3} = \frac{CV}{F_3} \quad \ldots(2.15)$$

C and V represent respectively the capacitance and voltage of sample.

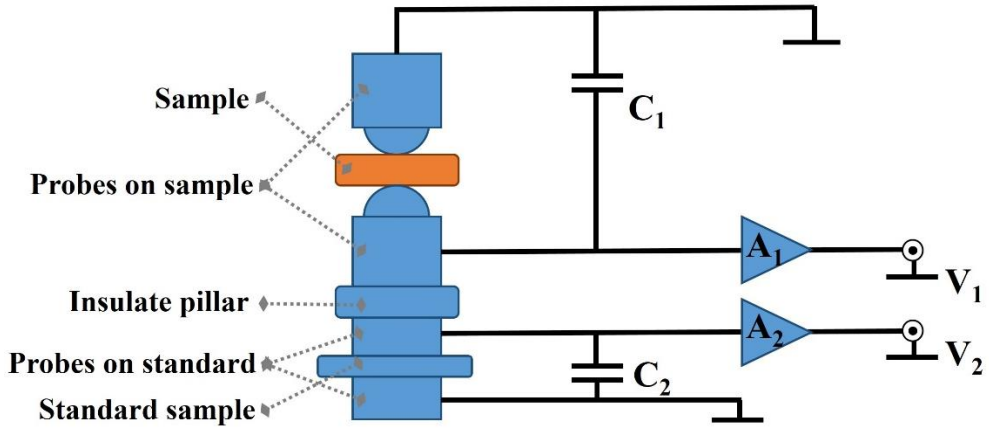

Figure 2.10 Setup of measuring quasi-static piezoelectric constant d_{33}.

The calculation of d_{31} is different from d_{33}. The calculation is as follows:

$$d_{31} = k_p \sqrt{\frac{1-\sigma}{2} \varepsilon_{33} s_{11}} \quad \ldots(2.16)$$

Where ε_{33} means the relative dielectric constant. s_{11} means the elastic compliance coefficient defined by:

$$s_{11} = \frac{\eta^2}{\pi^2 t^2 {f_r}^2 (1-\sigma^2)\rho} \quad \ldots(2.17)$$

Where t represents the thickness of the sample (unit:m) of and ρ its density (kg.m^{-3}).

Chapter 3 Soft and hard Iron (Fe) doped PSLZT (PSLZT-Fe) ferroelectrics

3.1 Introduction

From decades, lead zirconate titanate (PZT) based ceramics have been the most widely applied piezoelectric materials owing to their large scale production capability, high piezoelectric response and the advantages of tailoring their properties through their chemical compositions [81]. Beyond intrinsic features, metal doping of PZT based ceramics modulates their piezoelectric properties and ensures their involvement in different applicative devices.

Three kinds of doping ions in PZT based ceramics can be considered as function of their stable valences states. The donor doping, referred as “soft”, is realized by using ions with higher valence such as La^{3+}, Ta^{5+}, Nb^{5+} etc. For the acceptor doping “hard”, ions with lower valence state are used such as Fe^{3+}, Mg^{2+}, Al^{3+}, Sc^{3+} etc. The last doping mode referred as “equivalent” which uses ions such as Sr^{2+}, Ba^{2+} etc. preserves the same valence state. Donor doping favors cation vacancies such as lead vacancies in the host ceramics and then decrease the concentration of oxygen vacancies. Thus, the ceramics may exhibit large strains and strain hysteresis but a low mechanical quality factor. Oppositely, acceptor doping can increase oxygen vacancies of samples and the ceramics present the low strain and strain hysteresis but a high mechanical quality factor. For equivalent doping such as Sr^{2+}, improved dielectric permittivity and high electromechanical coupling factors can be induced due to the straining of the PZT lattice by substitution of Sr with a smaller size at the Pb site [82-84]. To optimize their electrical properties, some PZT ceramics are co-doped with donor and acceptor ions [83-85]. Jakes et al studied the defects in $Pb_{0.985}La_{0.01}(Zr_{0.5224}Ti_{0.4726}Fe_{0.005})O_{2.9975}$ ceramics and found that $(Fe'_{Zr,Ti} - V_O^{\cdot\cdot})^{\cdot}$ defect dipoles are involved in soft doped PZT ceramics [86]. Koduri et al studied the microstructure of $(PbLaSr)(ZrTiFe)O_3$ ceramics with different Sr concentrations [87]. They also investigated piezoelectric properties of Nb doped $(PbLaSr)(ZrTiFe)O_3$ [88].

Since La^{2+} is the most important donor dopant in A site and Fe^{3+} is the most important acceptor dopant in B site for PZT, it has been reported that (La, Fe) co-doped PZT ceramics exhibit enhanced performances compared to pure PZT. However, the effect of the La/Fe ratio on the electrical properties of (La, Fe) codoped PZT ceramics wasn't systematically investigated.

In this chapter, PSLZT-Fe ceramics with different compositions were realized by using different La/Fe ratios. The effects of doping concentrations on the morphological features and crystal structures of as-obtained ceramic samples were also analyzed in details. In this frame, the ferroelectric, piezoelectric and dielectric performances over the PSLZT-Fe samples were investigated, and the relevant mechanism was also analyzed. The results revealed that soft-hard doping can greatly impact the strain-electric field curves. Moreover, by tuning the annealing temperature, the effects on the piezoelectric properties of the PSLZT-Fe ceramics were clarified. The ferroelectric capabilities of the poled and unpoled samples were characterized. The origin of the pinning effects emerged in electric-field induced strain was discussed based on the "defect dipoles" model. This contributes to identify the role of defect dipoles on the upgraded performance of the soft-hard doping PSLZT-Fe samples.

3.2 Synthesis of PSLZT-Fe

Fe^{3+} doped $(Pb_{0.94}Sr_{0.05}La_{0.01})(Zr_{0.53}Ti_{0.47})O_3$ ($PSL(ZT)_{1-x}$-Fe_x, x = 0, 0.005, 0.010, 0.015 piezoelectric ceramics were prepared by the solid-state reaction method. Reagent-grade oxide powders (Pb_3O_4, $SrCO_3$, La_2O_3, ZrO_2, TiO_2 and Fe_2O_3) were chosen as raw materials for the synthesis of $PSL(ZT)_{1-x}$-Fe_x ceramics. For each composition, the oxides and carbonates were weighed accurately according to the stoichiometric ratio of $PSL(ZT)_{1-x}$-Fe_x ceramics. Powders were ball-milled and then were dried. Mixed powders were calcined for 4 h at 800 °C. Then the calcined powders were subsequently ball-milled and dried again to obtain homogeneous powders. The obtained powders were pressed into pellet disks. After burning out the binder for 3 h at 550 °C, the disks were sintered in air atmosphere at 1160 °C-1280 °C

for 2 h. After sintered, samples could be analyzed for phases, microstructures and so on. As for analysis of electric properties, specimens should be coated by silver paste on both sides at 720 °C for 0.5 h.

The crystal structures of samples were characterized by powders X-ray diffraction (XRD, Rigaku D/max 2550V) with a Cu Kα radiation. The morphologies of samples were analyzed by scanning electron microscopy (SEM, KYKY-EM3200) and EDS equipment. The dielectric properties (ε and tanδ) and piezoelectric properties (k_p and Q_m) were measured using an HP4294A precise impedance analyzer (Agilent Technologies Inc., Palo Alto, CA) according to IEEE standards [89]. The *P-E* hysteresis loops and *S-E* strain of samples were measured by a TF analyzer (Model 2000E, aixACCT Systems, Germany). Piezoelectric coefficient d_{33} was tested by piezo d_{33} meter (ZJ-3A, Institute of Acoustics, Chinese Academy of Sciences).

3.3 Microstructures and phases of PSLZT-Fe

3.3.1 Microstructures

Fig. 3.1 shows the SEM images of the fracture surface of $PSL(ZT)_{1-x}$-Fe_x samples sintered at 1160 ℃. Fig. 3.2 exihibits the grain sizes and relative densities of $PSL(ZT)_{1-x}$-Fe_x ceramics. The size of grains, ranging from 2 μm to 5 μm, increases when x is less than 0.010 and then decreases with the further increase of Fe^{3+} content. Fe^{3+} has the lower valence than Ti^{4+} and Zr^{4+}. The replacement of low valence in the B-site results in the excessive negative valence to maintain electric neutrality, which ultimately increases oxygen vacancies in the material. It is well known that the oxygen vacancies improved the distortion of lattices would ultimately improved the growth of grains during the sintering process. However, the average size of grains of $PSL(ZT)_{0.085}$-$Fe_{0.015}$ slightly decreases with high Fe^{3+} doping. It may be attributed to the changes of phase structures. Moreover, all $PSL(ZT)_{1-x}$-Fe_x samples shown high relative densities at more than 95% in Fig. 3.2, indicating the high densities of PZT systems.

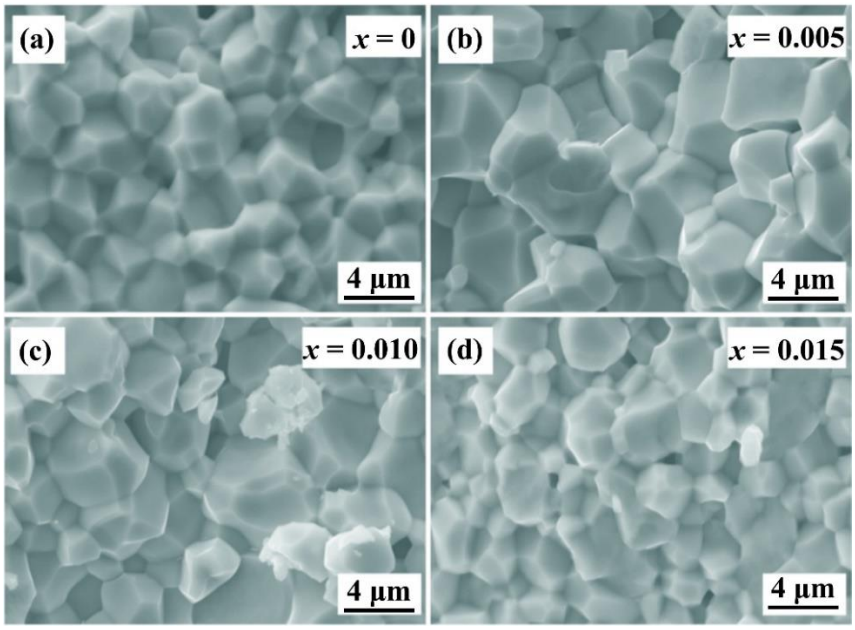

Figure 3.1 SEM images of the fracture surfaces of PSL(ZT)$_{1-x}$-Fe$_x$ ceramics, (a) x = 0, (b) x = 0.005, (c) x = 0.010, (d) x = 0.015.

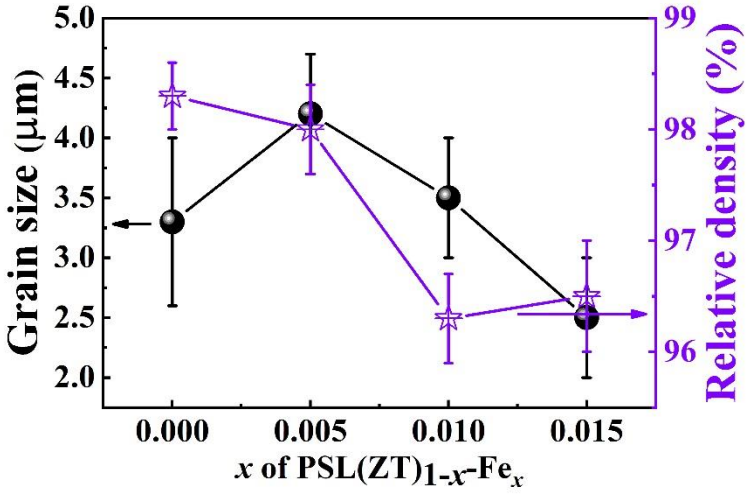

Figure 3.2 Grain sizes and relative densities of PSL(ZT)$_{1-x}$-Fe$_x$ ceramics.

Fig. 3.3(a)-(g) shows the SEM images of the fracture surface of PSL(ZT)$_{0.995}$-Fe$_{0.005}$ samples with different sintering temperatures. Fig. 3.3(h) shows the grain sizes and relative densities of PSL(ZT)$_{0.995}$-Fe$_{0.005}$ samples. It is found that the grain size of the sample increases with increasing sintering temperature. In general, high sintering temperatures provided the large driving force to stimulate the growth of grains, resulting to the large-size grains of samples. In Fig. 3.3(h), relative densities of samples decreased with increasing sintering temperatures. And relative densities of

$PSL(ZT)_{0.995}$-$Fe_{0.005}$ samples can stay over 96% with different temperatures.

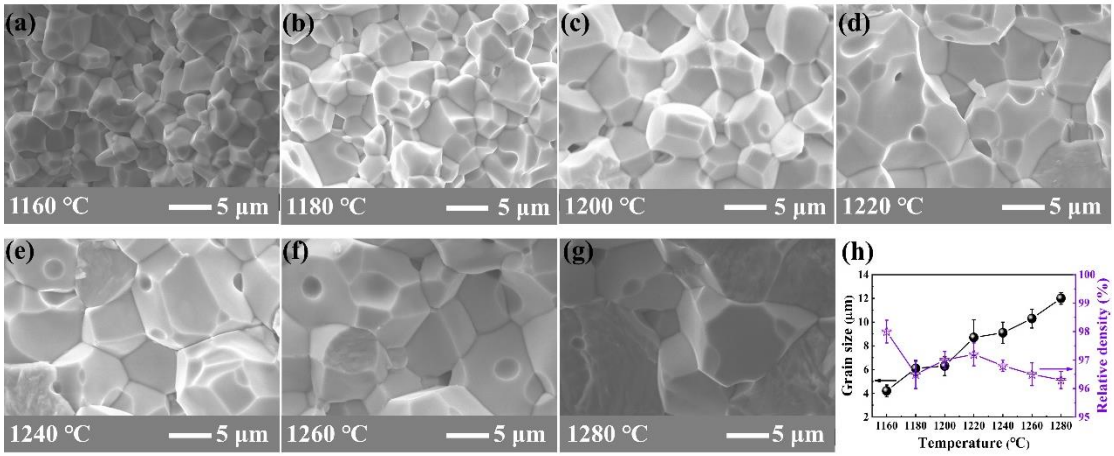

Figure 3.3 SEM images of the fracture surfaces of $PSL(ZT)_{0.995}$-$Fe_{0.005}$ ceramics with different sintering temperatures, (a)-(g) 1160 ℃-1280 ℃. (h) Grain sizes and relative densities of the sample.

Fig. 3.4(a)-(g) shows the SEM images of the fracture surface of $PSL(ZT)_{0.990}$-$Fe_{0.010}$ samples with different sintering temperatures. Fig. 3.4(h) shows grain sizes and relative densities of $PSL(ZT)_{0.990}$-$Fe_{0.010}$ samples. It is found that the grain size of the sample is small about 3 μm when sintered at 1160 ℃. The grain size increases abnormally when the sintering temperature was increased to 1180 ℃. From 1180 ℃ to 1280 ℃, the grain sizes remain similar. It is possible that the sintering temperature of 1160 ℃ is not enough for this high-doped system to improve the growth of grains. For the sintering temperature at 1180 ℃, a drastic increase of the grain size is observed and remains almost stationary for higher temperatures up to 1260 ℃. SEM images of this $PSL(ZT)_{0.990}$-$Fe_{0.010}$ composition exhibit the larger relative densities from 1180 ℃ to 1260 ℃, resulting in the highest relative density about 1240 ℃.

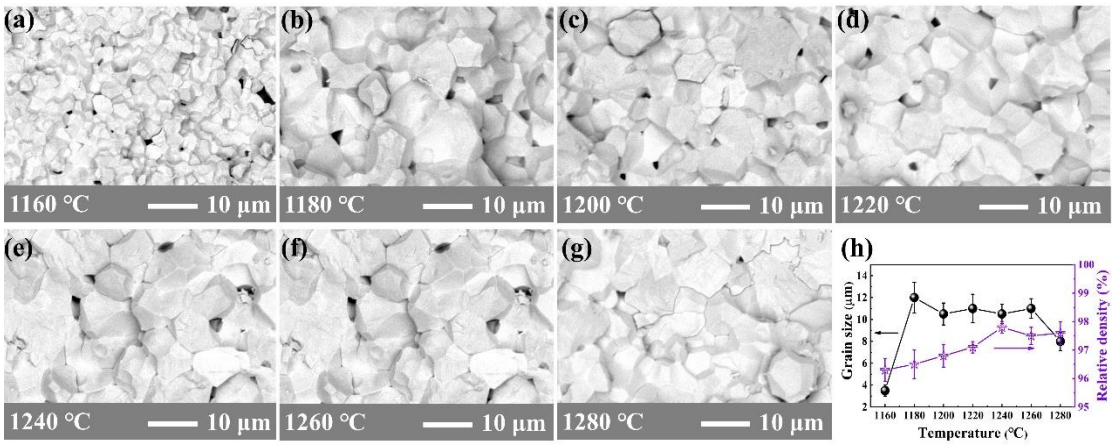

Figure 3.4 SEM images of the fracture surfaces of PSL(ZT)$_{0.990}$-Fe$_{0.010}$ ceramics with different sintering temperatures, (a)-(g) 1160 ℃-1280 ℃. (h) Grain sizes and relative densities of the sample.

3.3.2 Coexistence of phases

For PSL(ZT)$_{1-x}$-Fe$_x$ ceramics sintered of 1160 ℃, Fig 3.5 shows the XRD patterns with 2θ in the range from (a) 10° to 60° and (b) 43° to 45.5°. In order to limit the effects of internal stresses and privileged orientations in bulk ceramics on the XRD results, the samples were milled into powders before the XRD measurements. All the patterns show the pure perovskite structure for PSL(ZT)$_{1-x}$-Fe$_x$ ceramics. PSLZT-Fe$_0$ and PSL(ZT)$_{0.095}$-Fe$_{0.005}$ ceramics exhibit the tetragonal structure, for (111) peak is singlet whereas (200) peak is doublet according to the standard PZT PDF [8]. It can also be observed that the intensity of (200) (including (020)) peak is approximately twice high compared to (002) peak in PSLZT-Fe$_0$ and PSL(ZT)$_{0.095}$-Fe$_{0.005}$, which corresponded with the line splitting of the tetragonal phase [84]. However, with increasing the Fe^{3+} content, the 2θ diffraction peaks near 44 ° can be decomposed in three lorentzian peaks while only two peaks are required for PSLZT-Fe$_0$ and PSL(ZT)$_{0.095}$-Fe$_{0.005}$. It means that a coexistence of rhombohedral and tetragonal phases occurs in PSL(ZT)$_{0.090}$-Fe$_{0.010}$ and PSL(ZT)$_{0.085}$-Fe$_{0.015}$, while the tetragonal phase holds for PSLZT-Fe$_0$ and PSL(ZT)$_{0.095}$-Fe$_{0.005}$ ceramics [78]. The compositions with x = 0.010 and x = 0.015 lie in the morphotropic phase boundary (MPB) region which can be extend for higher Fe^{3+} content [1, 78, 91]. Previous reports showed that ceramics with MPB were involved for x = 0.45~0.5 in pure Pb(Zr_{1-x} Ti_x)O_3 [91], which

is in agreement with the Ti ratio (0.47) of PSL(ZT)$_{1-x}$-Fe$_x$ ceramics used in this work. Compared with the effect of MPB on the ferroelectric properties, the defect dipoles play a more important role on softening-hardening features of PSLZT-Fe samples, which would be discussed later. Moreover, since the radius of La^{3+} (1.032 Å) is similar to Pb^{2+} (1.190 Å) at the A site, while the radius of Fe^{3+} (0.645 Å) is similar to Zr^{4+} (0.720 Å) and Ti^{4+} (0.605 Å) at the B site. It was thus considerably feasible for La^{3+} and Fe^{3+} to enter the lattice of PZT during the solid-state reaction, with a relative low doping content of 1% for both in the PZT systems. There was no second phase of $LaFeO_3$ in materials evidenced by the XRD results. Thus, the solid solution effect of $LaFeO_3$ was not taken into account when analyzing the effect of Fe^{3+} doping.

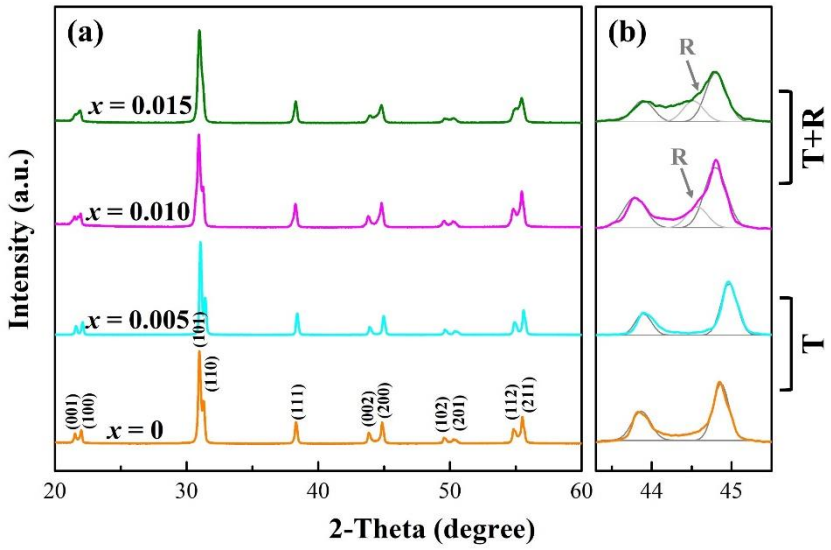

Figure 3.5 XRD patterns of PSL(ZT)$_{1-x}$-Fe$_x$ ceramics, (a) 2θ = 20 °-60 °, (b) 2θ = 43.3 °-45.5 °.

3.4 Ferroelectric properties of PSLZT-Fe

3.4.1 Polarization-electric field loops

Fig. 3.6 shows the polarization-electric field (*P*-*E*) hysteresis loops and current-electric curves for PSL(ZT)$_{1-x}$-Fe$_x$ ceramics. The undoped PSLZT ceramics show a well-saturated *P*-*E* loop at room temperature [92]. The peak of the current matches with the coercive field (E_c) which indicates that domain walls are switched [93]. As for materials such as PSLZT-Fe$_0$ and PSLZT-Fe$_{0.005}$, the intersections of with hysteresis the horizontal axis in in Fig. 3.6(a)-(b) are consistent with E_c because of the

easy rotation of domain walls (18 kV/cm, 18 kV/cm respectively). The situation is different for higher doping rates as shown in Fig. 3.6(c)-(d) and can be accounted for by the domain walls being not switched. The domain walls are pinned by oxygen defects as revealed by the narrow loops. The actual values of E_c in PSLZT-$Fe_{0.010}$ and PSLZT-$Fe_{0.015}$ are at the same high value 20 kV/cm which correlates with the high Fe^{3+}content. The remnant polarization (*P*r) decreases from 40 μC/cm^2 to 2.4 μC/cm^2 with increasing Fe^{3+} content from 0 to 0.015. It indicates that the softening-hardening transition appeared with the doping ratios of Fe^{3+}. The shapes of the hysteresis loops are attributed to the reversible movement of domain walls in materials as they are electrically or elastically pinned by defects [94]. The *P*-*E* loop of PSLZT at $x = 0.005$ is nearly the same as that of undoped ceramics although defect dipoles are involved in $x = 0.005$ doped ceramics. As x is 0.010 which is equal to La^{3+} content, the remnant polarization decreases sharply which is the typical feature of hard doped piezoelectric ceramics. With more Fe^{3+} content than La^{3+}, the material appears an antiferroelectric-like with a double hysteresis loop which indicates the parallel alignment of oxygen vacancies with spontaneous polarization [36, 94]. The results indicate that the ratio of La/Fe is crucial to the soft/hard behavior of PSLZT-Fe ceramics. It is well known that La doping can create lead vacancies which improve the rotation of domains, while Fe doping can create oxygen vacancies which pin the domains or domain walls. When La/Fe is more than 1, soft PZT ceramics are obtained [95, 96]. With La/Fe ≤ 1, ceramics exhibit the hard feature. The properties of PSLZT-Fe ceramics are determined by the competition between two kinds of vacancies.

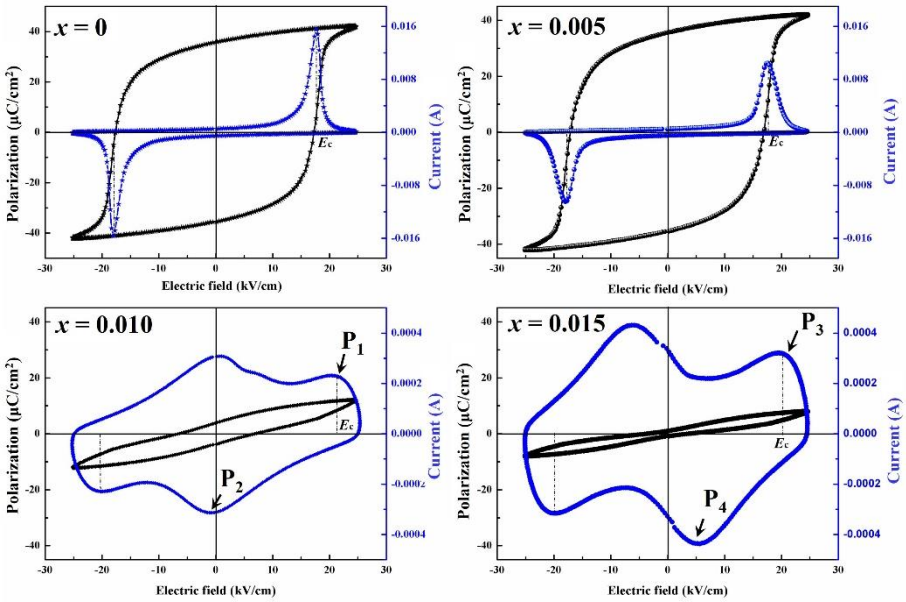

Figure 3.6 Polarization-electric field (*P-E*) hysteresis loops and current-electric field (*I-E*) loops of PSL(ZT)$_{1-x}$-Fe$_x$ (x = 0, 0.005, 0.010, 0.015) ceramics.

Figure 3.7 shows of domain switching of PSL(ZT)$_{1-x}$-Fe$_x$ samples under the electric field (x = 0.010, 0.015). The current-electric field (*I-E*) loops in the previous figure shows that two pairs of current peaks appear in the *I-E* loops for two high-doped samples (x = 0.010, 0.015). The current peaks P_1 and P_3 under the high electric field are related to the switching of ferroelectric domains. The current peaks P_2 and P_4 under the low electric field are related to the depolarization of the switched ferroelectric domains under the restoring force of defect dipoles. According to Ren's theory of defect dipoles, the oxygen vacancies in the acceptor-doped samples form the defect dipoles P_D after aging, and the direction of P_D and spontaneous polarization P_s remains consistent, keeping the ferroelectric domains stable [60]. For PSL(ZT)$_{1-x}$-Fe$_x$ ceramics, the current of the peaks P_1 and P_3 in the high-doped component (x = 0.010, 0.015) are significantly reduced compared to the low-doped component, which means that only a small portion of ferroelectric domains switched under the high electric field. Because switching of ferroelectric domains is pinned by defect dipoles, which makes the switching of ferroelectric domains difficult, as shown in Figure 3.7 (b) and (e). The peaks P_1 and P_3 current reveal the actual coercive field of high-doped samples (x = 0.010, 0.015), both of which are 20 kV/cm. When the applied electric field in the

two samples gradually decreases, the current gradually increases, which indicates that switched domains are not stable. When electric field was removed, ferroelectric domains began depolarization and gradually recovered to the initial state. In the sample of x = 0.010, P_2 appears in the negative electric field, indicating that ferroelectric domains have not fully recovered to the initial state when the electric field decrease to zero. Therefore, the sample has a certain remnant polarization at zero electric field, which is 7.5 μC/cm^2. Figure 3.7(c) also shows that few switched ferroelectric domains of the sample still occur in the initial state. For the sample of x = 0.015, the high concentration of defect dipoles in the sample has a stronger pinning effect on the ferroelectric domains. The polarization returns to the initial state, forming the current peak P_3. Therefore, the remnant polarization of the sample is close to zero without the electric field, about 2.4 μC/cm^2. The defect dipoles formed in the high-doped samples (x = 0.010, 0.015) have a pinning effect on switching of ferroelectric domains under the electric field, contributing to the double *P-E* loops.

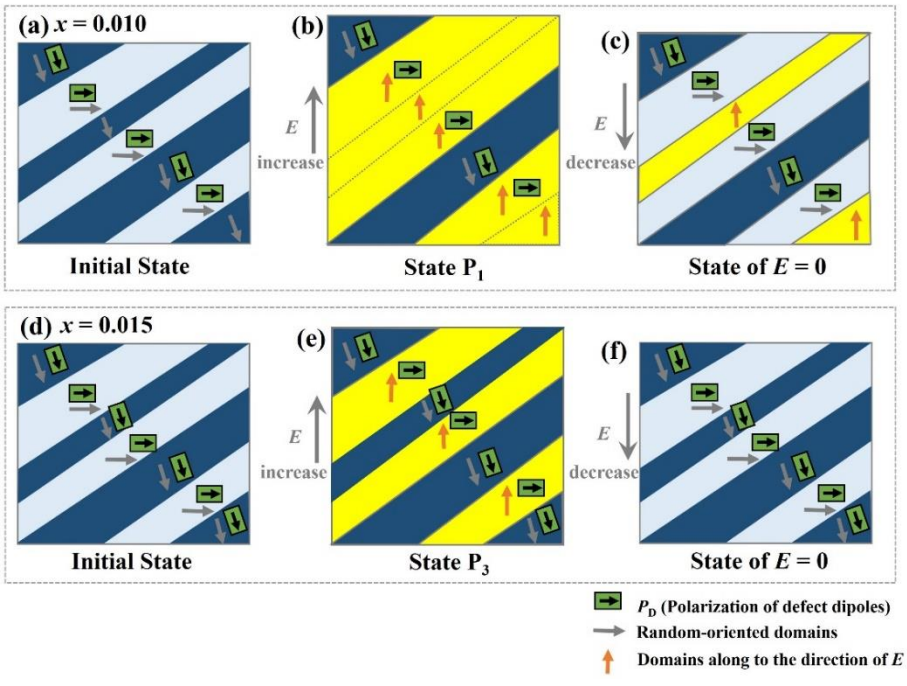

Figure 3.7 Model of domain switching of PSL(ZT)$_{1-x}$-Fe$_x$ samples under the electric field, (a) x = 0.010, (b) x = 0.015.

Fig. 3.8(a) and (b) shows the polarization-electric field (*P-E*) hysteresis loops and the

value of P_r and E_c of $PSL(ZT)_{0.995}$-$Fe_{0.005}$ ceramics with different sintering temperatures. The hysteresis loops of the same composition exhibit the well-saturated shape for the different sintering temperatures. With the increasing sintering temperature, remnant polarization of the sample decreased slightly and coercive electric-field keep a stationary value. Thus, the $PSL(ZT)_{0.995}$-$Fe_{0.005}$ composition exhibits enhanced ferroelectric properties at low sintering temperatures.

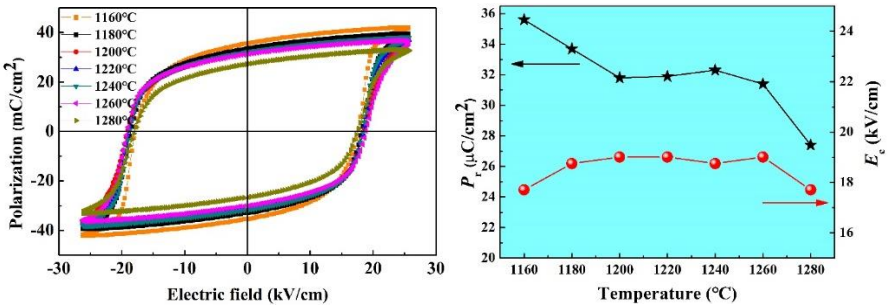

Figure 3.8 (a) Polarization-electric field (*P*-*E*) hysteresis loops, (b) values of P_r and E_c of $PSL(ZT)_{0.995}$-$Fe_{0.005}$ ceramics with different sintering temperatures.

Fig. 3.9(a) and (b) shows the polarization-electric field (*P*-*E*) hysteresis loops and the value of P_r and E_c of $PSL(ZT)_{0.990}$-$Fe_{0.010}$ ceramics with different sintering temperatures. The sample appears a double hysteresis loop at different temperatures. The results show that the sintering temperature did not play an important role in the pinning effects. With increasing the sintering temperature, remnant polarization remains constant first and then increases slightly. At the same time, the coercive electric field E_c is similar and exhibits a low value 4 kV/cm. As for highly doped ceramics, high sintering temperatures are helpful to improve the ferroelectric properties, especially from 1240 ℃ to 1260 ℃.

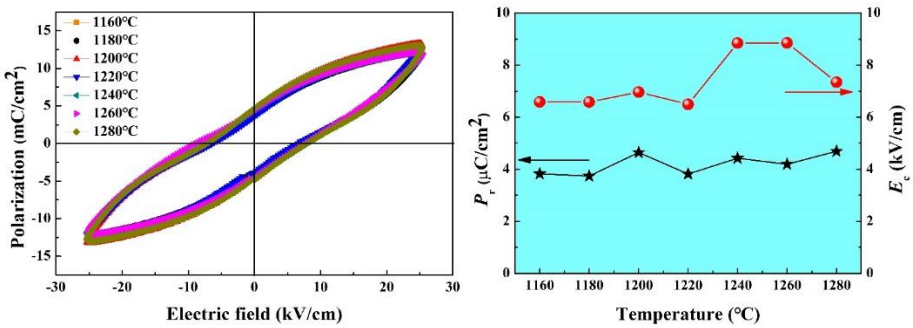

Figure 3.9 (a) Polarization-electric field (*P*-*E*) hysteresis loops, (b) values of P_r and E_c of $PSL(ZT)_{0.990}$-$Fe_{0.010}$ ceramics with different sintering temperatures.

3.4.2 Electric field-induced strain

The bipolar strain-electric field (*S*-*E*) curves shown in Fig. 3.10 are consistent with *P*-*E* loops (shown in Fig 3.6). It is shown that the *S*-*E* curves have the shape of archetypal butterflies with a quite large positive and negative for x = 0 or 0.005, which is accounted for by the easy rotation of domains walls under the applied electric field. The maximum strain of low-doped samples could reach 0.22%. However, negative *S*-*E* curves disappear with increasing Fe^{3+} content as in $PSL(ZT)_{0.090}$-$Fe_{0.010}$ and $PSL(ZT)_{0.085}$-$Fe_{0.015}$. Thus, the behavior is typical for hard-doping ceramic samples [97]. The high Fe^{3+} doping which form oxygen defects easily induces the pinning of domains and the non-negative bipolar strain.

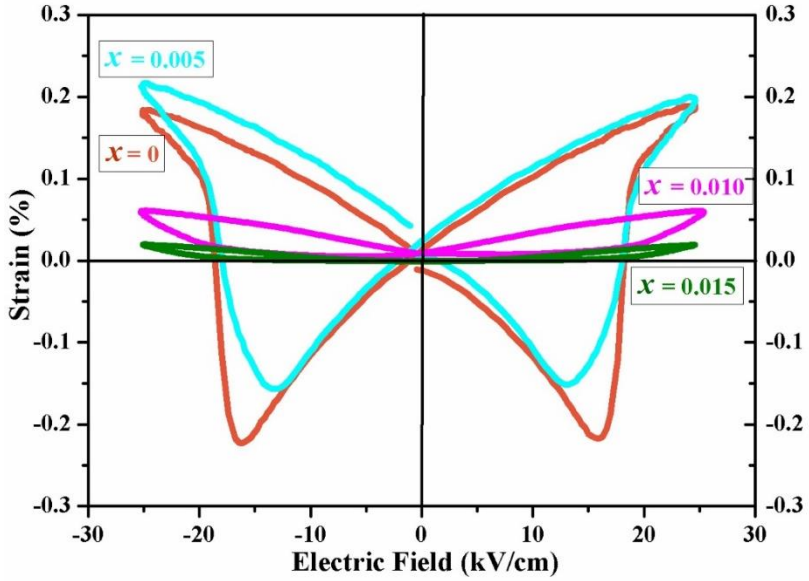

Figure 3.10 Bipolar strain-electric field (*S*-*E*) loops of $PSL(ZT)_{1-x}$-Fe_x (x = 0, 0.005, 0.010, 0.015) ceramics.

Fig. 3.11 shows unipolar strains induced by the electric field in $PSL(ZT)_{1-x}$-Fe_x samples and at room temperature. It is shown that the maximum strain decreases with increasing the Fe^{3+} content, as expected for a softening-hardening transition in piezoelectric materials. The maximum value of the unipolar strain changes from 0.19% to 0.09% rapidly when x decreases at 0.005 in $PSL(ZT)_{1-x}$-Fe_x. According to the piezoelectric equation [98]:

$$x_{ij} = S^E_{ijkl} X_{kl} + d_{nij} E_n \quad \ldots(3.1)$$

With i=j=3, the relation is simplified as:

$$x_{33} = S^E_{33} X + d_{33} E \quad \ldots(3.2)$$

x_{33} is radial strain, S^E_{33} is the partial elastic compliance constant, X the radial stress, and E the applied electric field, d_{33} is piezoelectric constant. It is known that both the converse piezoelectric effect in lattices (intrinsic effect) and the switching of domains (extrinsic effect) can contribute to the unipolar displacement [24]. $d_{33} \times E$ was regarded as the strain from inverse piezoelectric effect, and it does not include the contribution of domain switching. Thus, the strain stemming from domain switching results in the variation in the value of x_{33} and $d_{33} \times E$. As shown in Fig. 3.11, the value of strain is higher than that of $d_{33} \times E$ because of the extrinsic effect. In addition, the difference between x_{33} and $d_{33} \times E$ became smaller with increasing the Fe^{3+} content. It indicates that domain switching in high-doped samples was pinned by oxygen defects. When the extrinsic effect of domain switching is lowered by the pinning effect, it leads to the softening-hardening transition in $PSL(ZT)_{1-x}$-Fe_x ceramics.

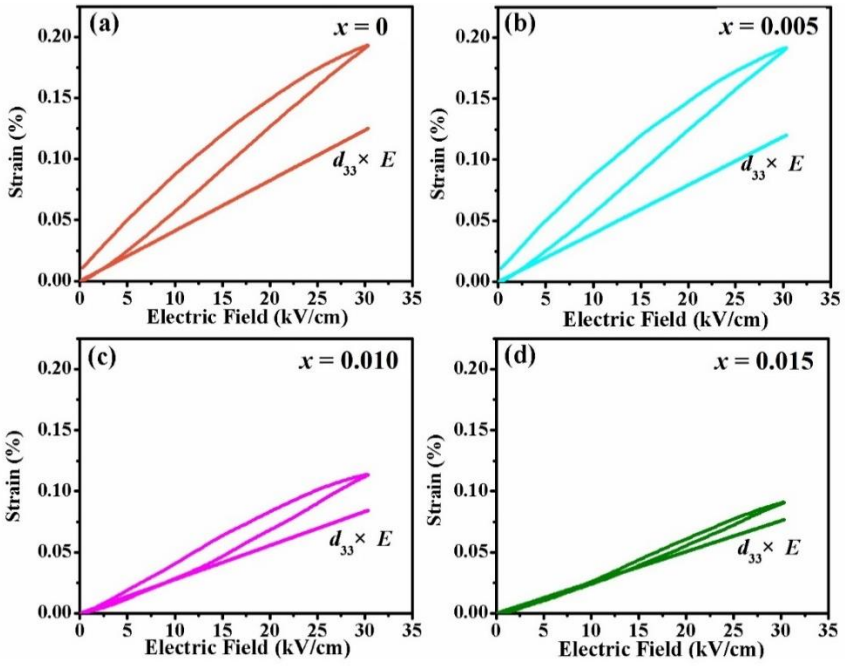

Figure 3.11 Unipolar strain-electric field (*S*-*E*) loops and values of $d_{33} \times E$ in $PSL(ZT)_{1-x}$-Fe_x ceramics, (a) x = 0, (b) x = 0.005, (c) x = 0.010, (d) x = 0.015.

Fig. 3.12 shows the bipolar strain of $PSL(ZT)_{0.995}$-$Fe_{0.005}$ ceramics with different sintering temperatures. The bipolar strain of samples exhibit the highest value when the sample was sintered at 1160 ℃. With increasing sintering temperature from 1180 ℃, the value of bipolar strain did not decrease sharply, indicating that the sintering temperatures have little influence on the electric-field induced strain.

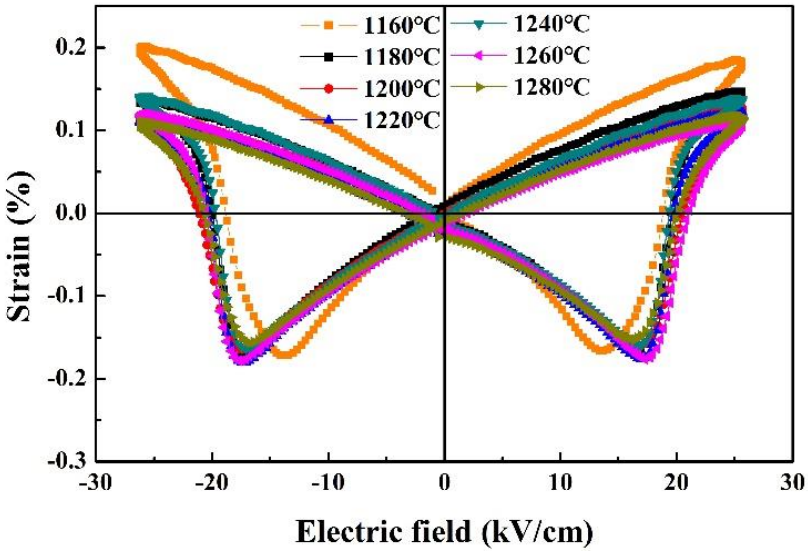

Figure 3.12 Bipolar strain-electric field (*S*-*E*) loops of $PSL(ZT)_{0.995}$-$Fe_{0.005}$ ceramics with different sintering temperatures.

Fig. 3.13 shows the bipolar strain of $PSL(ZT)_{0.990}$-$Fe_{0.010}$ ceramics with different sintering temperatures. All samples with different sintering temperatures show the non-negative strain which is indicative of the existence of pinning effect. The sintering temperatures did not alter the hard feature of $PSL(ZT)_{0.990}$-$Fe_{0.010}$ composition while the bipolar strain exhibits the highest value at high sintering temperatures of 1220 ℃.

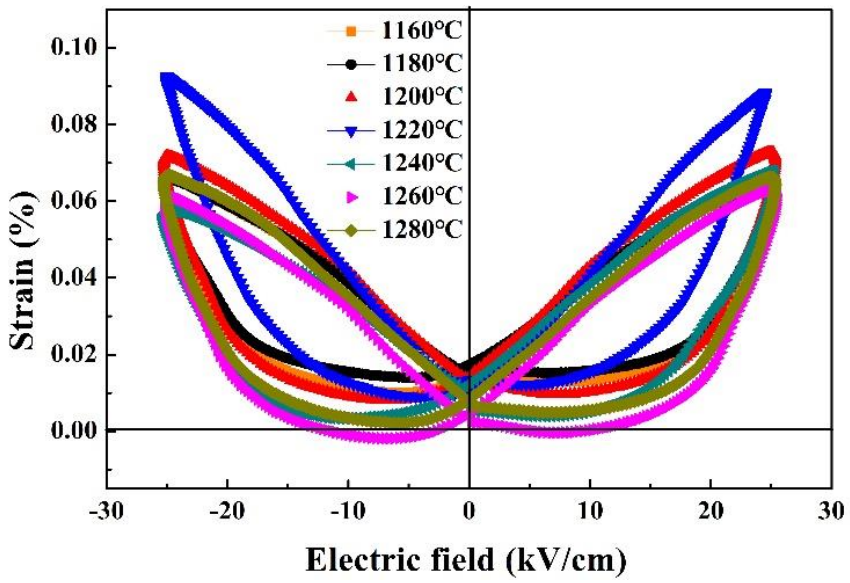

Figure 3.13 Bipolar strain-electric field (*S*-*E*) loops of PSL(ZT)$_{0.990}$-Fe$_{0.010}$ ceramics with different sintering temperatures.

3.4.3 Model of defect dipoles for hard PSLZT-Fe

The variations of the piezoelectric properties of doped materials depend on the nature of doping elements and on the structural defects involved in the host materials. The polarization-electric field (*P*-*E*) loops and the strain-electric field (*S*-*E*) loops reported in Fig 3.14(a)-(b) show similar characteristics in the poled and non-poled donor-doped samples. Thus, well-saturated *P*-*E* loops and large unipolar strains indicates the easy domain rotations favored by the occurrence of lead vacancies V''_{Pb}. Indeed, according to the defect equilibrium reaction:

$$La_2O_3 \xrightarrow{PZT} 2La^{\cdot}_{Pb} + V''_{Pb} + 3O^{\times}_{o} \qquad \ldots(3.3)$$

V''_{Pb} are expected to improve the piezoelectric properties in 'soft' PZT compounds by reducing the energy barriers for ferroelectric domain switching [99]. Thus lead vacancies is suggested to enhance the superior piezoelectric properties in 'soft' doped PZT compounds.

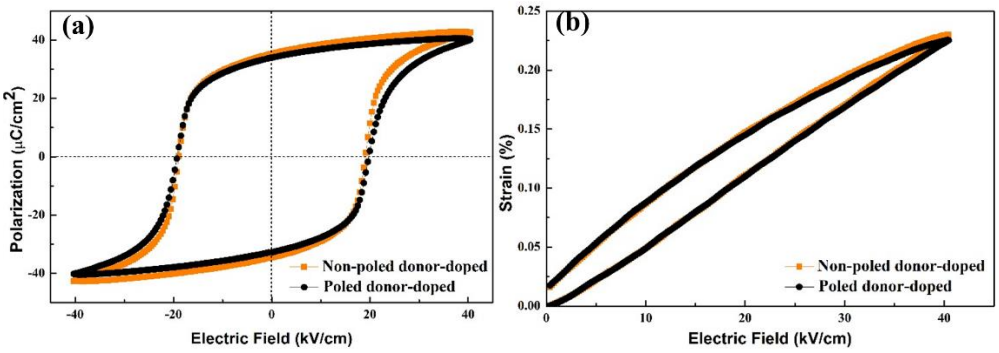

Figure 3.14 (a) Polarization-electric field (*P*-*E*) hysteresis loops, (b) Unipolar strain-electric field (*S*-*E*) loops for unpoled and poled acceptor-doped PSL(ZT)$_{0.995}$-Fe$_{0.005}$ samples.

Non-poled acceptor-doped sample exhibits a double hysteresis loop and a recoverable polarization in external electric field in Fig 3.15(a). It is also found that bipolar strain is small for non-poled acceptor-doped ceramics and the curve shows symmetric shape (Fig. 3.15(a)). Fig. 3.15(b)-(c) show the double hysteresis loop and the recoverable polarization for the poled acceptor-doped sample when the positive electric field is antiparallel and parallel to the direction of poling respectively. After poling the sample, the positive bipolar strain and P_r become very large for the same electric field and the curve of bipolar strain becomes asymmetric as shown in Fig. 3.15(b) and (c). The internal bias field E_i evaluated at 16 kV/cm is generated by the mechanism of realignment of defect dipoles [100], revealing the evolution of domain switching. Fig. 3.15(d) show the unipolar strain-electric field (*S*-*E*) loop for non-poled acceptor-doped sample, (e) for the poled acceptor-doped sample when the positive electric field is antiparallel to the direction of poling and (f) for the poled acceptor-doped sample when the positive electric field is parallel to the direction of poling. It is found that the unipolar strain of the poled acceptor-doped ceramic becomes as high as 0.13% compared with that of non-poled acceptor-doped ceramics (0.08%) with an electric field of 40 kV/cm (Fig. 3.15(d) and (f)). After poling, P_s and P_D align parallel to the external field in the acceptor-doped material. By applying the external field along the poling direction, the defect dipoles P_D reoriented to align along the direction of P_s under the electric field with less domain switching. The aligned defect dipoles formed the internal bias electric field E_i, and the internal bias

partially contributes to the large electric field induced strain in Fig. 3.15(e) and (f) [44]. There is also a small hysteresis of unipolar strain resulted from the less domain switching in Fig. 3.15(f), compared with that in Fig.3.15(d) and (e).

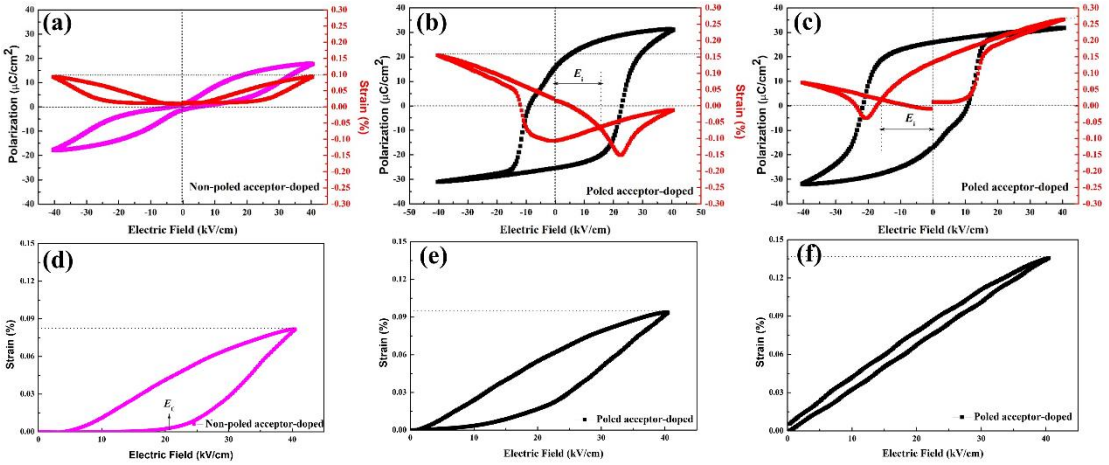

Figure 3.15 (a) Polarization-electric field (*P*-*E*) hysteresis loop and bipolar strain-electric field (*S*-*E*) loop, (b) unipolar strain-electric field (*S*-*E*) loop for unpoled acceptor-doped $PSL(ZT)_{0.985}$-$Fe_{0.015}$ sample. (c) *P*-*E* and bipolar *S*-*E* loops, (d) unipolar *S*-*E* loop for the poled sample where the direction of the electric field is antiparallel to the poled direction. (e) *P*-*E* and bipolar *S*-*E* loops, (d) unipolar *S*-*E* loop for the poled sample when the direction of the electric field is parallel to the poled direction.

The behavior of pinning in acceptor-doped ceramics was explained by the defect-symmetry model in Fig. 3.16. With the excess of Fe^{3+}, $(Fe'_{Zr,Ti} - V_o^{\cdot\cdot})^{\cdot}$ defect dipoles are formed in B sites of PZT systems following the defect equilibrium:

$$2Fe_2O_3 \xrightarrow{2TiO_2} 2(Fe'_{Zr,Ti} - V_o^{\cdot\cdot})^{\cdot} + 2Fe'_{Zr,Ti} + 6O_o^{\times} \quad \ldots(3.4)$$

$(Fe'_{Zr,Ti} - V_o^{\cdot\cdot})^{\cdot}$ defect dipoles are formed in the acceptor-doped sample. The polarization of defect dipoles P_D formed by defect dipoles are parallel to the P_s (spontaneous polarization) because of the diffusion of oxygen vacancies before applying an external electric field. During the application of an external electric field, the domain switching leads to the increase of the overall polarization. As the domain switching involves nucleation and growth, a multi-domain state is formed at an intermediate field before a new single-domain state with P_s perpendicular to the initial direction appears at a sufficiently high field [31]. The unchanged P_D stops the domain

from switching along the direction of the electric field. After removing the external field, the remnant polarization P_r approach the zero and we consequently observed a double *P-E* hysteresis loop because of the pinning of defect dipoles. The overall polarization is locked by the defects and their domain switching is difficult, leading to the decrease in remnant polarization (P_r) from 35.6 μC/cm^{-2} (donor-doped sample) to 2.4 μ C/cm^{-2} (acceptor-doped sample). During the poling process of the acceptor-doped sample, more and more polarization inversions take place and the number of dipoles increases since an external electric field accelerates diffusion of vacancies and thus increases the probability for the dipole formation including the $(Fe'_{Zr,Ti} - V_o^{\cdot\cdot})^{\cdot}$ defect dipoles. When the external electric field is parallel to the direction of poling electric field, the realignment of defect dipoles contributes to the polarization. As a result, the averaged polarization restores the original value. On the other hand, when the direction of electric field is antiparallel to the direction of poling, a rapid decrease occurs on the switchable polarization; the polarization is still pinned by the defect dipoles. It has been explained that the most part of the hysteresis loops is normal and the other is still pinned in Fig. 3.15(b) and (c) [101].

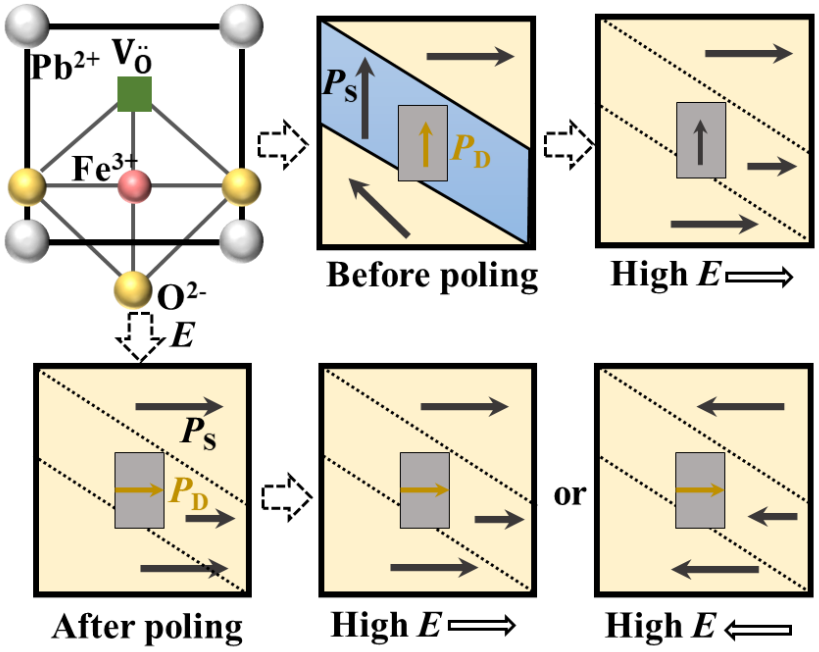

Figure 3.16 The switching model of defect dipoles P_D and spontaneous polarization P_s in the external electric field with poled and unpoled respectively.

3.5 Dielectric properties of PSLZT-Fe

3.5.1 Dielectric constants

The evolution of the dielectric constant (ε) with the temperature for $PSL(ZT)_{1-x}$-Fe_x ceramics is shown in Fig. 3.17. Samples were investigated by using a heating and cooling runs. The results illustrate the differences of Curie temperature (T_C) between heating curves (325 ℃) and cooling curves (305 ℃). However, different content of doping Fe^{3+} did not influence the value of T_C for all samples. The maximum ε at x = 0 and 0.005 is much higher than those of x = 0.010 and 0.015 around T_C. There are also a significant difference of ε between PSLZT-Fe_0 (1480) and $PSL(ZT)_{0.085}$-$Fe_{0.015}$ (1179) at room temperature, because the effect of defect dipoles in high-doped samples weaken the whole polarization.

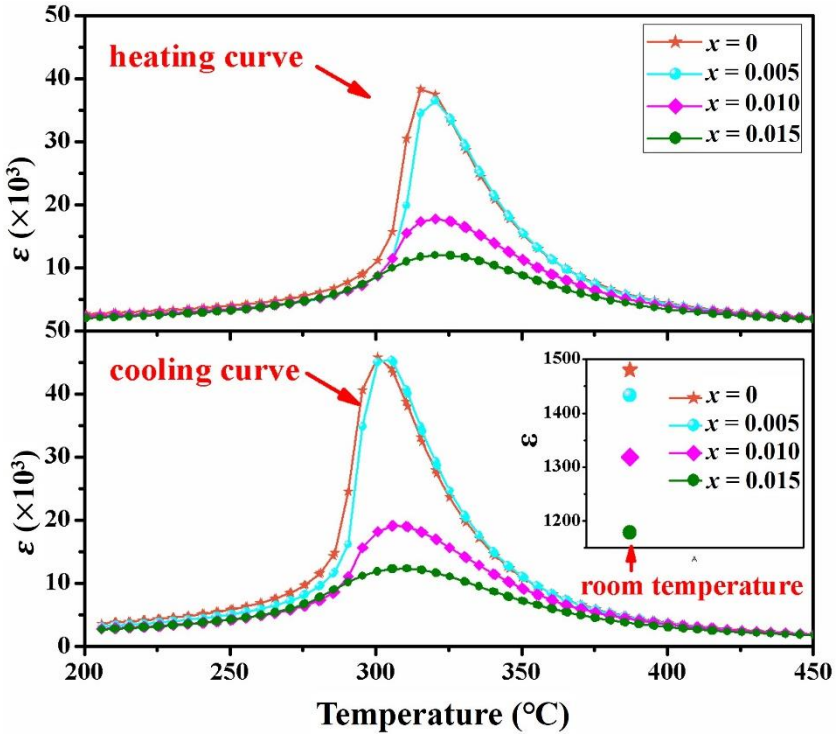

Figure 3.17 Temperature dependence of dielectric constants ε of $PSL(ZT)_{1-x}$-Fe_x ceramics on heating curves and cooling curves respectively.

3.5.2 Dielectric losses

The dielectric loss (tanδ) with temperature for $PSL(ZT)_{1-x}$-Fe_x is shown in Fig. 3.18. It can be seen that hard ceramics (La/Fe ≤ 1) exhibit much lower dielectric losses than

that of soft ceramics (La/Fe $>$ 1) at room temperature. The term "tanδ" of the hard PSLZT-Fe ceramics increases rapidly at high temperatures ($>$ 350 ^{o}C) and becomes higher than that of soft PSLZT-Fe ceramics. The high dielectric losses in piezoelectric ceramics originate from the motion of domain walls. There are more oxygen vacancies in hard PSLZT-Fe ceramics ($x \geq 0.010$) which pin the domain walls at room temperature. However, they exhibit the high mobility in ceramics and form the large leakage current at high temperatures. Therefore, the pinning of domain walls reduce the dielectric loss of hard PSLZT-Fe ceramics at room temperature, while the contribution from the leakage current dominates at high temperatures; hard PSLZT-Fe ceramics exhibit much higher dielectric losses above T_C.

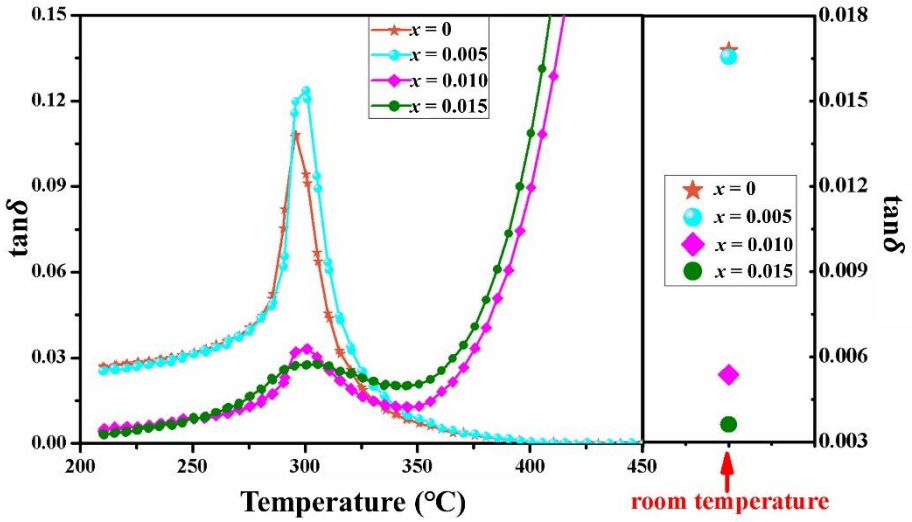

Figure 3.18 Temperature dependence of dielectric losses tanδ of PSL(ZT)$_{1-x}$-Fe$_x$ ceramics.

The anomalous dielectric constant and dielectric losses of acceptor-doped PSL(ZT)$_{0.995}$-Fe$_{0.005}$ and donor-doped PSL(ZT)$_{0.985}$-Fe$_{0.015}$ samples are shown in Fig. 3.19 (a) and (b). The dielectric constant of the donor-doped sample becomes larger originated from oscillating defect dipoles at low frequencies. The substitution of Zr^{4+} or Ti^{4+} by Fe^{3+} forms the oxygen vacancies. These defects are sufficiently mobile to form complex defects able to pin the overall polarization at room temperature. With increasing the temperature, oxygen vacancies become mobile, contributing to the ionic conductivity especially above T_C [86]. The dielectric constant and dielectric losses of the donor-doped sample at high temperature become high because of the

high leakage current in Fig. 3.19(b) [5].

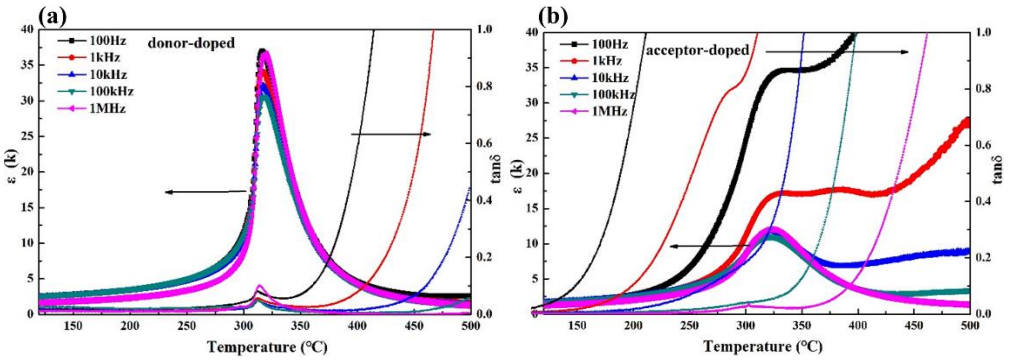

Figure 3.19 Temperature dependence of dielectric constants and dielectric losses of (a) acceptor-doped PSL(ZT)$_{0.995}$-Fe$_{0.005}$ sample and (b) donor-doped PSL(ZT)$_{0.985}$-Fe$_{0.015}$ sample.

3.6 Piezoelectric parameters of PSLZT-Fe

Fig. 3.20 shows the piezoelectric constant d_{33} at room temperature for the PSL(ZT)$_{1-x}$-Fe$_x$ ceramics annealed at different temperatures. It is apparent that higher d_{33} for soft-doping sample (x = 0, 0.005) can be achieved via suffering annealing at lower temperatures. The ideal annealing temperature for soft-doped samples lies below 1220 ℃. Conversely, higher annealing temperatures are relevant to obtain higher d_{33} for hard-doped samples (x = 0.010, 0.015), which implies the optimized annealing temperatures for hard-doped PSLZT-Fe ceramics above 1220 ℃.

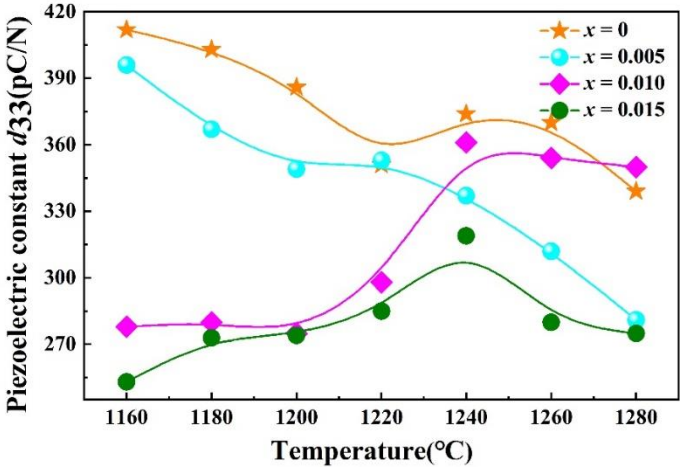

Figure 3.20 Piezoelectric constant d_{33} of PSL(ZT)$_{1-x}$-Fe$_x$ ceramics versus different sintering temperatures.

Fig. 3.21 illustrates the coupling coefficients and factor quality of PSL(ZT)-Fe$_0$ and PSL(ZT)$_{0.990}$-Fe$_{0.010}$ samples polarized at 1160 ℃. After effective poling, d_{33} for the

two samples are evaluated to be 412 pC/N and 240 pC/N, respectively. Furthermore, the piezoelectric stability is ensured with the temperature variation for low-doped sample (x = 0) while a variation is noticed in the highly doped sample (x = 0.010). Radial electromechanical coupling coefficient (K_p) and thickness electromechanical coupling coefficient (K_t) are determined to be respectively at 0.68 and 0.58 for PSL(ZT)-Fe_0. These values were almost unaltered in the temperature range -50 ℃ to 200 ℃. For $PSL(ZT)_{0.990}$-$Fe_{0.010}$, Kp and K_t have the values at 0.45, 0.42, respectively, for a temperature lower than 100 ℃ and undergo an affective decrease above 100 ℃. Mechanical quality factor Q_m which was obtained from LC equivalent circuit are highly dependent on the measurement temperature. Specifically, Q_m of high-doped ceramics are positively related to the applied temperatures, and the highest value at 400 was obtained at 160 ℃. The stability of phase angles for the high-doped sample is lower than the low-doped one.

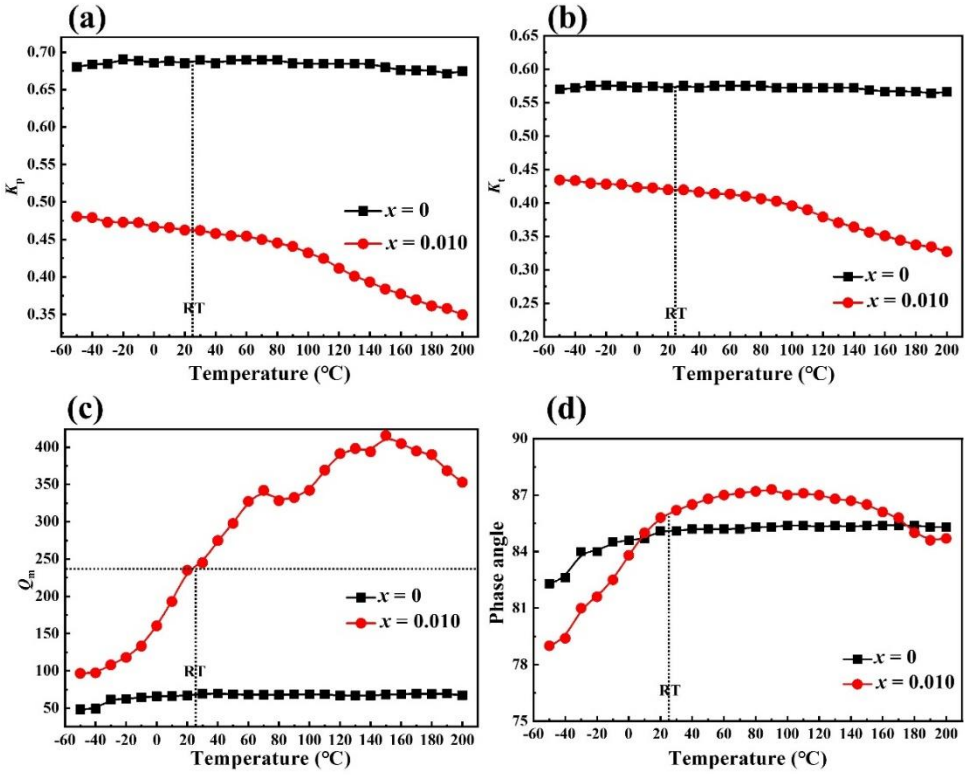

Figure 3.21 Temperature dependance of the planner electromechanical coupling factor k_p, the thickness electromechanical coupling factor k_t, the mechanical quality factor Q_m and the phase angle of PSL(ZT)-Fe_0 and $PSL(ZT)_{0.990}$-$Fe_{0.010}$ ceramics measured at different temperatures.

As mentioned above, the optimized sintering temperature are determined at 1260 ℃

for high-doped PSL(ZT)$_{0.990}$-Fe$_{0.010}$ sample. Average piezoelectric constants of PSL(ZT)$_{0.990}$-Fe$_{0.010}$ samples are 370 pC/N sintered at 1260 ℃, more than that sinterd at 1160 ℃. The d_{33} of PSL(ZT)$_{0.990}$-Fe$_{0.010}$ sample decreased slightly with increasing meseured temperatures shown in Fig. 3.22. When the sample was measured over Curie temperature, the value of d_{33} is still kept at the value of 82 pC/N. It may be attributed to the effect of space charges on the polarization.

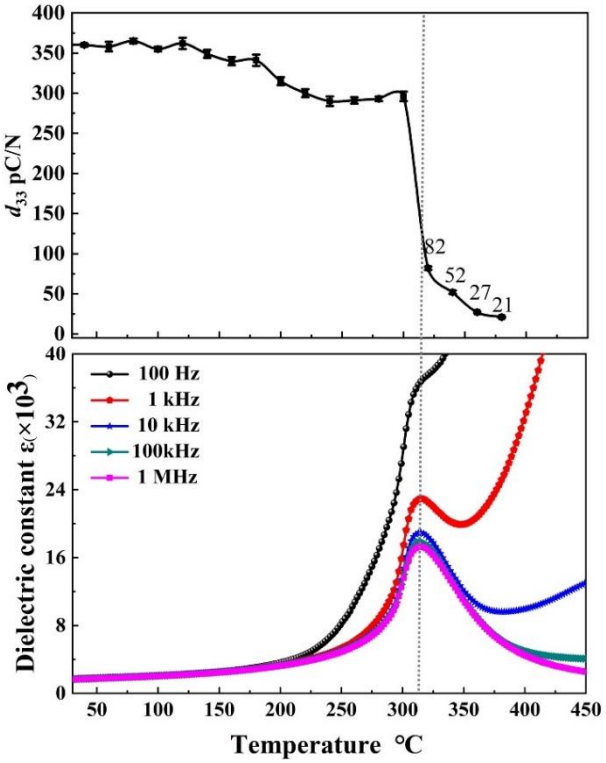

Figure 3.22 The piezoelectric constants of PSL(ZT)$_{0.990}$-Fe$_{0.010}$ ceramics dealed with different temperatures.

Fig. 3.23 presents the corresponding electromechanical coupling coefficient (K_p, K_t), mechanical quality factor (Q_m) and the phase angle of PSL(ZT)$_{0.990}$-Fe$_{0.010}$ sample sintered at 1260 ℃. K_p and K_t are stable at 0.70 and 0.58, respectively, when the testing temperature is below 80 ℃. But the electromechanical coupling coefficient drastically reduces for higher temperatures. Additionally, Q_m is about 150 at room-temperature and have tendency be improved for high temperatures. The evaluation of Q_m was made according to the equation given below:

$$Q_m = \frac{\beta}{4\pi|Z_m|(C_0+C_1)(f_a-f_r)} \quad \ldots(3.5)$$

Here β is Bessel correction factor, C_0 and C_1 are the total capacitance and active capacitance, respectively, in the equivalent circuit, f_a represents the anti-resonance frequency and f_r the resonance frequency. Z_m is the impedance of RLC circuit at the resonance frequency. As shown in Fig. 3.24, $|Z_m|$ at the resonance decreases with rising the temperature and contributes to the exceptionally enhanced Q_m. As for the hard materials, the migration of inner oxygen vacancies can be influenced by increasing the temperature, which leads to the significantly reduced impedance in the RLC curcuit, thus resulting in the sluggish stability.

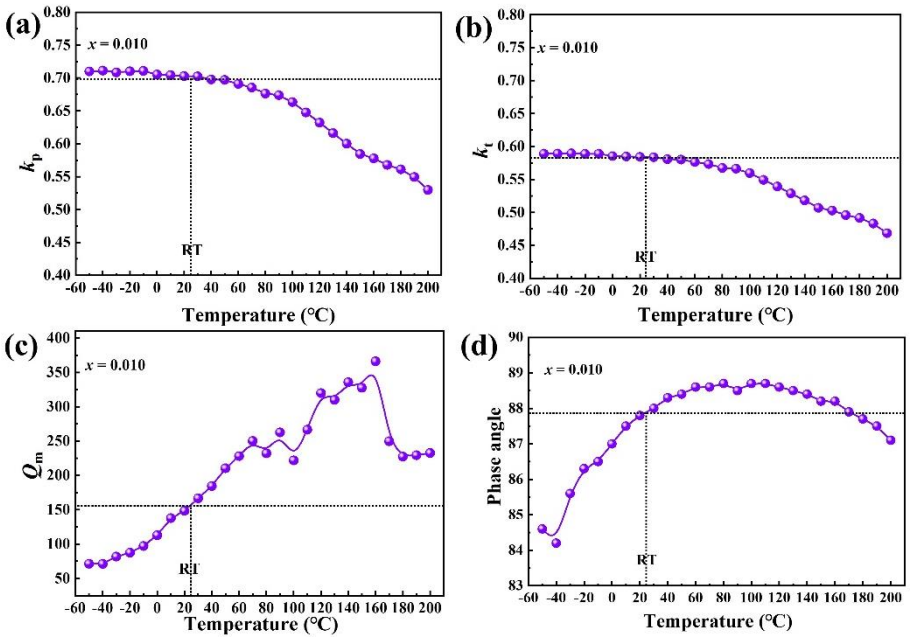

Figure 3.23 Temperature dependance of the planner electromechanical coupling factor k_p, the thickness electromechanical coupling factor k_t, the mechanical quality factor Q_m and the phase angle of $PSL(ZT)_{0.990}$-$Fe_{0.010}$ ceramics measured at different temperatures.

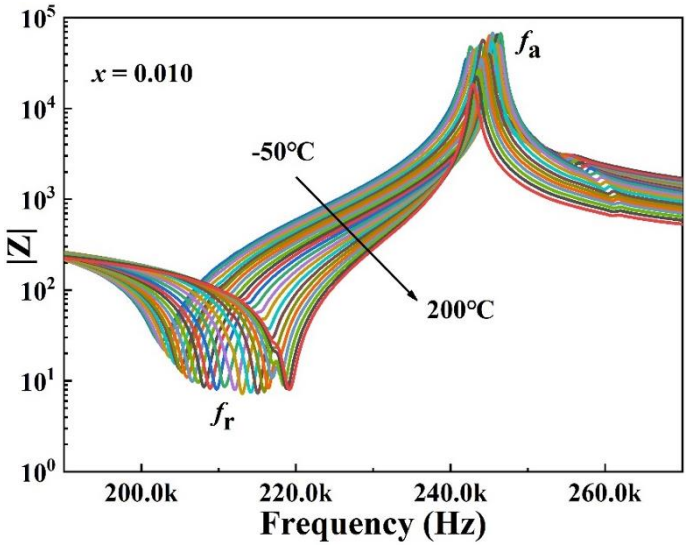

Figure 3.24 Frequency dependence of impedance |*Z*| of $PSL(ZT)_{0.990}$-$Fe_{0.010}$ ceramics measured at different temperatures.

3.7 Conclusions

In summary, the conventional solid-state reaction method was used to prepare series $PSL(ZT)_{1-x}$-Fe_x ceramics. The soft-hard characteristics can be well controlled by adjusting the La/Fe ratio. By using different annealing temperatures, the crystalline structure, microstructure, dielectric and piezoelectric properties were investigated systematically. The main results are summarized below:

(1) XRD results reveal a structural evolution from the tetragonal phase in low-doped samples to the coexistence of R-T phases in high-doped samples. The microstructure and grain sizes show a slight variation of grains with increasing Fe^{3+} content for $PSL(ZT)_{1-x}$-Fe_x ceramics.

(2) By comparing the polarization and strain, it was shown that the hysteresis-electric field loops present saturated shape for La/Fe > 1 which traduces apparent characteristics of soft-materials. This is also manifested from the large strain and the great hysteresis due to the easy mobility of domains. Moreover, soft samples show highest piezoelectric and dielectric coefficients of 412 pC/N and 1480 at room temperature, respectively. Oppositely, when the La/Fe ≤ 1, the hysteresis loop is similar to the case of antiferroelectric behavior marked by the small strain and limited hysteresis. These features are indicative of the limited motions of domains being

pinned by oxygen vacancy. However, the pinning effect at domain walls caused by defects was quite low. For Fe^{3+} concentrations at 0.010 and 0.015, the factor Q_m achieved its high value of 500 and exhibited hard feature, which was ascribed to the domain-wall pinning by oxygen vacancies in the system. Such a shift based on soft-hard doping was verified by the reduced S_{33}^{E} and the relevant mechanism for the soft-hard shift in $PSL(ZT)_{1-x}$-Fe_x was discussed in this section.

(3) The specific properties and the ferroelectric and dielectric performances of donor- and acceptor-doped were investigated systematically and analyzed in details. Comparative studies, based on the poled and unpoled samples, disclosed the influence of the polarization on the ferroelectric property of donor and acceptor-doped ceramics. For the unpoled sample, the defect dipole $(Fe'_{Zr,Ti} - V_o^{\cdot\cdot})^{\cdot}$ created by acceptor-doped contributed to the whole polarization pinning and then reducing the remnant polarization P_r. After samples being poled, polarization from defect dipoles P_D and the spontaneous polarization P_s rearranged under the applied electric field. The observed enhancement for the polarization and strain can be ascribed to low pinning effect on the domain walls. In addition, oxygen vacancies $V_o^{\cdot\cdot}$ involved in acceptor-doped samples favor the increase of dielectric constants and losses at low frequencies and high temperatures.

(4) Piezoelectric investigations were performed in the temperatures range [-50 ℃, 200 ℃]. The soft samples with high La/Fe ratios exhibit a better stability of their electromechanical coupling coefficients and mechanical quality factors under variable temperatures and frequencies. With respect to the samples doped by low La/Fe ratios, the unstable mechanical quality factor was caused by the instability of the low impedance in the equivalent circuit and its decrease with rising the temperature. As a consequence, hard-doped samples only showed excellent piezoelectric performances in a limited temperature range.

The investigations carried out on acceptor- and donor-doped PZT based ceramics pointed out the high performances achieved as function of the doping rates and their stability in wide temperature and frequency ranges. The developed approaches on such class of doped ceramics pave the way for improved ferroelectric responses

required for potential and innovative applications.

Chapter 4 Interplay of phases and ferroelectricity in Al doped $BiFeO_3$-$BaTiO_3$ (BFA-BT)

4.1 Introduction

Piezoelectric materials have contributed widely to improve the efficiency and sensitivity of sensors, actuators and transducers. In this frame, recent developments were dedicated to lead-free materials for their role in the environment preservation. As promising candidates for lead-free materials, $K_{0.5}Na_{0.5}NbO_3$ (KNN), $Bi_{0.5}Na_{0.5}TiO_3$ (BNT) and $BaTiO_3$ (BT) based ceramics are worthy of interest due to excellent piezoelectric responses [102, 103]. The low Curie temperature of BT and KNN based materials or the low depolarization temperature for BNT and BT based lead free systems, constitute a major drawback for the thermal stability of their electrical properties [104]. Therefore, bismuth ferrite ($BiFeO_3$) based ceramics with excellent multiferroic features and high Curie temperatures are promising systems.

Indeed, pure or doped $BiFeO_3$ are difficult to obtain as a single-phase structure with high piezoelectric responses and saturated polarization-electric (*P*-*E*) field hysteresis loops. The alternative challenge is then focused on the binary or ternary $BiFeO_3$ based systems able to achieve high piezoelectric performances. As examples, relevant domain-like structures were built based on $BiFeO_3$ and ABO_3-type perovskites such as $BaTiO_3$, $CaTiO_3$, $SrTiO_3$ and $Bi_{0.5}Na_{0.5}TiO_3$ [102, 105, 106]. Among them, $BiFeO_3$-$BaTiO_3$ with significantly enhanced piezoelectric activity is regarded as the most promising system. Also, $0.70BiFeO_3$-$0.30BaTiO_3$ was investigated as the optimal composition offering the highest remnant polarization along with high piezoelectric d_{33} coefficient [107]. Moreover, it was reported that Sc, Ga, Al, La, In, Co, Gd, Nd and Ni doping at B sites can promote the piezoelectric and ferroelectric properties of $BiFeO_3$-$BaTiO_3$ system as ABO_3 perovskite materials [108-110]. Among these elements, Al^{3+} is well adapted for the substitution in B-site, preserving the crystalline structure but modifying the electronic hybridization in the occupied sites. Thus, Al element would contribute to adjust the ferroelectric and piezoelectric

peculiarities of $BiFeO_3$ based systems.

In this chapter, Al doping $0.70BiFeO_3$-$0.30BaTiO_3$ ceramics were systematically investigated for their microstructures and electric properties. The dielectric constants show pronounced diffuse phase transition and the relaxation behaviors correlate with the content of Al^{3+}. Meanwhile, ^{57}Fe Mössbauer spectra point out the variation of the B-site Fe^{3+} content towards the Al doping in ABO_3 perovskite structure. The microstructure, crystalline features, ferroelectric behavior and dielectric constants were analyzed as function of Al doping. It afforded valuable approaches for the investigation of the inner interplay between doping effects, the ferroelectric behavior and the structural features of the Al doped $BiFeO_3$-$BaTiO_3$ (BFA-BT) host systems.

4.2 Synthesis of BFA-BT ceramics

In this chapter, the solid-state method was used for the synthesis of BFA-BT ceramics. Specifically, $0.70(Bi_{1.05}Fe_{1-x}Al_x)O_3$-$0.30BaTiO_3$ (BFA-BT) compositions with ($0.015 \leq x \leq 0.060$) were prepared by the conventional solid-state method. Bi element was added more 5 mol% against the excessive volatilization. High purity oxides powders of Bi_2O_3, TiO_2, Fe_2O_3, La_2O_3, MnO_2 and carbonate $BaCO_3$ were used as raw materials. For each composition, the oxides and carbonates were weighed accurately to ensure the stoichiometric ratio of $0.70(Bi_{1.05}Fe_{1-x}Al_x)O_3$-$0.30BaTiO_3$ ceramics. The defined compositions of powders were mixed thoroughly in ethanol using zirconia balls for 10 h, then dried and calcined at 720 ℃ for 2 h. Then the calcined powders were subsequently ball-milled and dried again. The obtained powders were pressed into pellet disks. After burning out the binder for 6 h at 550 °C, the disks were sintered in air at 1010 °C for 2 h. The characterizations were then performed on as-sintered samples but for the electrical and dielectric measurements, the pellets were coated by silver paste on both sides and annealed at 720 °C for 0.5 h.

The scanning electron microscopy (Carl Zeiss Auriga 60) was employed to characterize the microstructures of samples. The crystalline structures of samples were investigated by X-ray diffraction (XRD) analysis by using Empyrean-Panalytical diffractometer operating at 40 kV, 30 mA with Cu Kα1 (λ =

1.5406 Å) and Cu Kα2 ($\lambda = 1.5444$ Å) lines. ^{57}Fe Mössbauer spectra were recorded at 77 K without external applied field in a transmission geometry using ^{57}Co/Rh γ-ray source mounted on an electromagnetic drive with a triangular velocity form. The polarization-electric field (*P*-*E*) loops were measured at room temperature by ferroelectric analyzer (10 Hz, TF Analyzer 2000, aixACCT Systems GmbH, Aachen, Germany). The temperature dependence of dielectric properties was measured using a precision impedance analyzer from room temperature to 600 ℃ (Agilent 4192A). The imaginary modulus of samples versus frequency was obtained at different temperatures by Novocontrol Broadband dielectric spectrometer (Alpha, BETA Analyzer, Germany).

4.3 Structures and organization of BFA-BT phases

4.3.1 Microstructures

Fig. 4.1(a)-(d) shows the SEM images of the BFA-BT samples. Fig. 4.2 shows the grain size and relative densities of all samples. It exhibits the increasing porosity in highly doped ceramics ($x \geq 0.045$). Oppositely, the microstructures of BFA-BT materials with $x = 0.015$ and 0.030 show relatively high-density structures with large grain size of 5-7 μm. As reported in previous works on ferroelectric ceramics, high-density structures lower the leakage current [111, 112]. Also, the large grain sizes increase the domain sizes and reduce the pinning effect of domain walls. This contributes to the polarization switching under an extrinsic electric field. Thus, improved ferroelectric properties are expected to be realized in high-density BFA-BT ceramics where large grain sizes are involved.

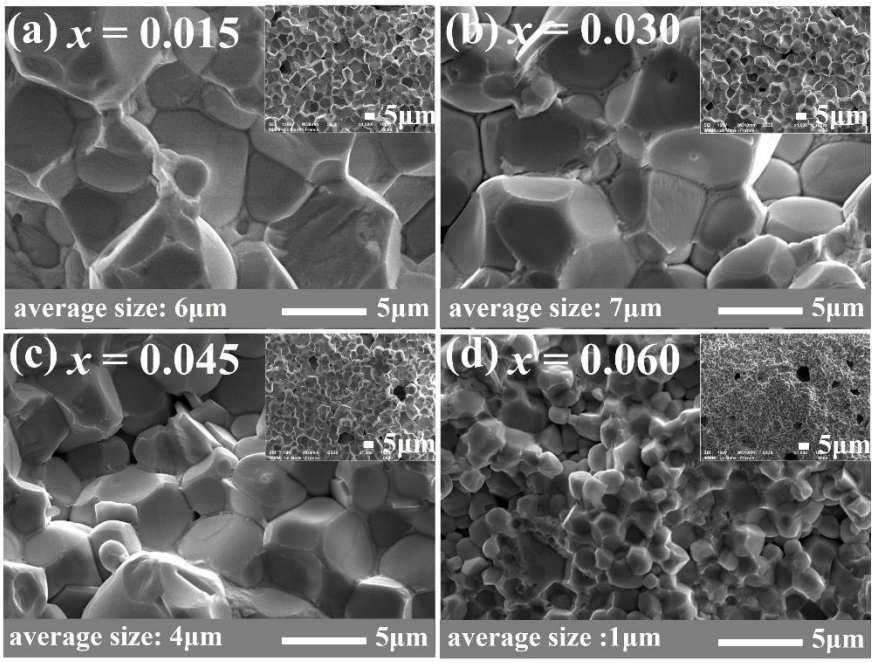

Figure 4.1 Fracture SEM images of $BiFe_{1-x}Al_xO_3$-$BaTiO_3$ ceramics, (a) x = 0.015, (b) x = 0.030, (c) x = 0.045, (d) x = 0.060.

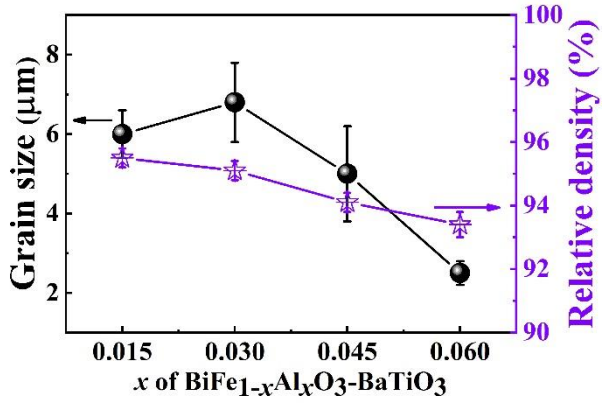

Figure 4.2 Grain sizes and relative densities of $BiFe_{1-x}Al_xO_3$-$BaTiO_3$ ceramics.

4.3.2 Structural properties of (R, T) phases

Fig. 4.3(a)-(d) shows the Rietveld refinement of XRD patterns in BFA-BT samples at room temperature. Attempts were made to consider space groups (*R*3c, *R*3m, *C*m and *P*4mm) relevant for the $BiFeO_3$-$BaTiO_3$ system with a mixture of phases such as *R*3c-*P*4mm or *R*3c-*C*m as reported elsewhere [107, 113]. In the present work, the optimal Rietveld refinement is achieved by using the coexistence of rhombohedral *R*3c and tetragonal *P*4mm phases with an error factor of $R_{wp} \approx 9.7\%$. All the compositions have the dominant perovskite structures with the coexistence of *R*3c and *P*4mm phase,

resulted from fitting the three peaks associated to (200) reflection in the range of 2θ = 45 °-46 °. Minor secondary phases account for the extra line at 28 ° emanating from $Bi_2Fe_4O_9$ and $Bi_{25}Fe_4O_{39}$ as impure structures involved in $BiFeO_3$ ceramics and difficult to eliminate from the network [114, 115].

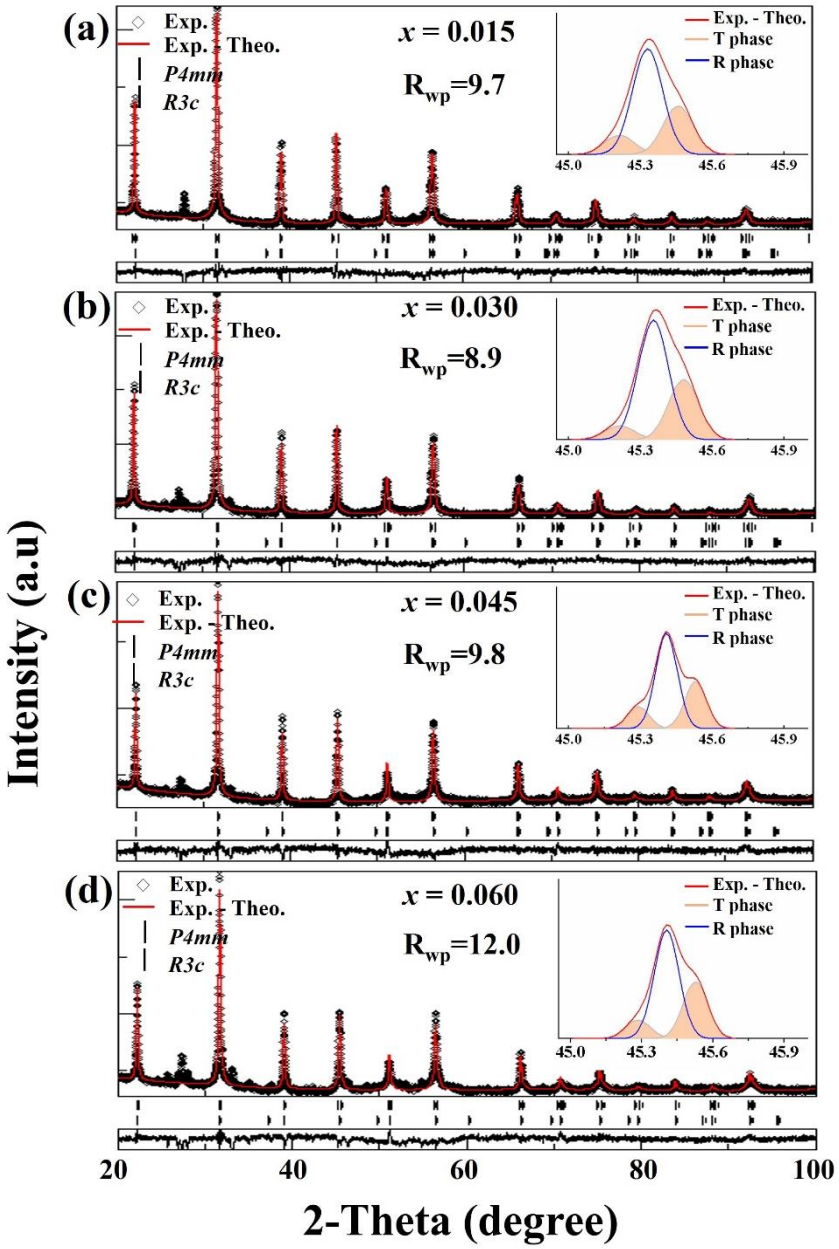

Figure 4.3 XRD patterns with Rietveld refinement for $BiFe_{1-x}Al_xO_3$-$BaTiO_3$ ceramics, (a) x = 0.015, (b) x = 0.030, (c) x = 0.045, (d) x = 0.060.

The parameters (c_T, a_T) from the Rietveld refinement, the ratio c_T/a_T of the tetragonal phase, the fraction and distortions of the rhombohedral phase are shown in Fig. 4.4 and Fig. 4.5 respectively. A slight structural contraction can be expected with

the few amount of Al doping, giving rise to a slight canting of the lattice parameters parameters (c_T, a_T). For low Al doping (x = 0.030), a high c_T/a_T is achieved (Fig. 4.4) as well as a high degree of rhombohedral distortions (60 °-α_R) in Fig. 4.5. These features enhance the distortion of the samples when they are polarized under extrinsic electric field and improve the ferroelectric response. Different fractions of the rhombohedral phase were induced in BFA-BT systems with different Al doping ratios (Fig. 4.5). The composition of x = 0.030 leads to the highest fraction of the rhombohedral phase with optimal values of the spontaneous and remnant polarization as discussed in forthcoming section.

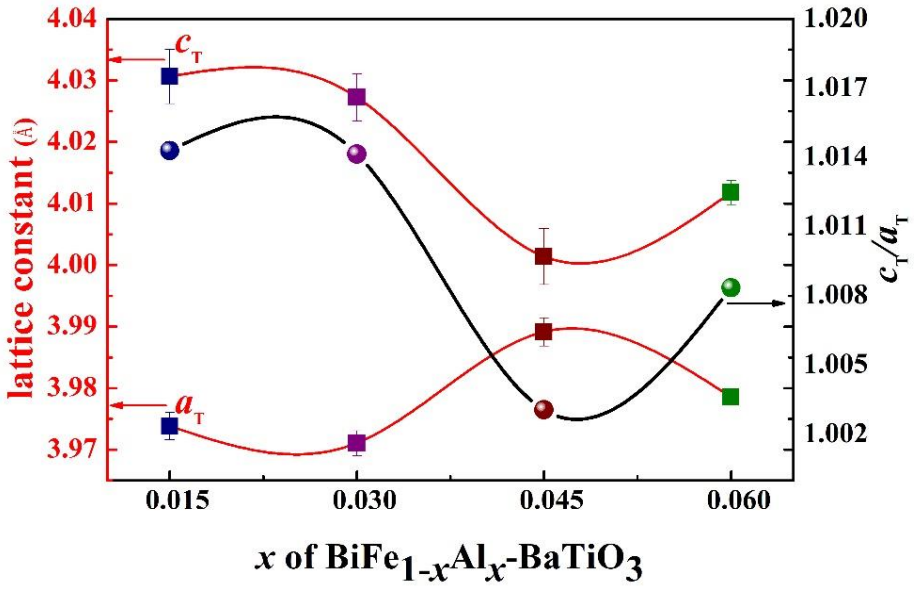

Figure 4.4 Lattice constants (c_T, a_T) and c_T/a_T for the tetragonal phase in $BiFe_{1-x}Al_xO_3$-$BaTiO_3$ ceramics.

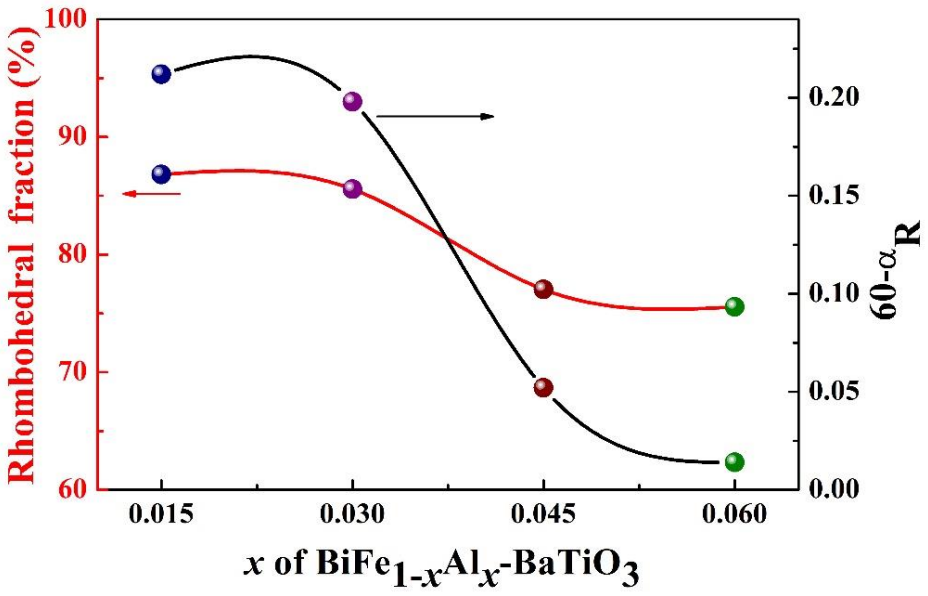

Figure 4.5 Fraction and distortions 60 °-α_R for the rhombohedral phase in $BiFe_{1-x}Al_xO_3$-$BaTiO_3$ ceramics.

4.3.3 Mössbauer probing of Fe disorder

To investigate structural features at the atomic scale, ^{57}Fe Mössbauer spectrometry measurements were carried out at 77 K. Indeed, ^{57}Fe Mössbauer spectrometry is a powerful technique to study the structural features of different iron species by analyzing the hyperfine interactions ^{57}Fe [116]. Mössbauer spectra of $BiFe_{1-x}Al_xO_3$-$BaTiO_3$ with x = 0.030, x = 0.060 obtained at 77 K are shown in Fig. 4.6. The spectra exhibit the shape of characteristic Zeeman sextets and the absence of a paramagnetic doublet, indicating that two samples have magnetically ordered spin structures at 77 K [113]. The Zeeman sextet is composed of asymmetrical lines, thus indicating the presence of at least two sites of iron (with different neighbors). Also, two main sub-spectra were necessary to account for the experimental results (Fig. 4.6). In both samples, the isomer shifts correspond to the valence state Fe^{3+} ions in Tab. 4.1. The first sub-spectrum with the asymmetrical shape correlated with the values of hyperfine parameters involves in the $BiFeO_3$ phase [117]. Indeed, the magnetic behavior is dominated by an antiferromagnetic G type superimposed to a long-range cycloidal modulation [117]. This sub-spectrum could be reproduced by a narrow distribution of the hyperfine parameters such as quadripolar shift or hyperfine field,

corresponding to random orientation of the spins. The second sub-spectrum is characterized by broad lines and a net decreasing on the value of the hyperfine field (49.4 T). This behavior could be attributed to the disorder nature of the super exchange interactions because of the random substitution of Fe^{3+} ions by nonmagnetic Al^{3+} ions. This second sub-spectra becomes more broadened and more pronounced (59%) in the sample with x = 0.060 indicating an important disorder of Fe^{3+} ions at B sites.

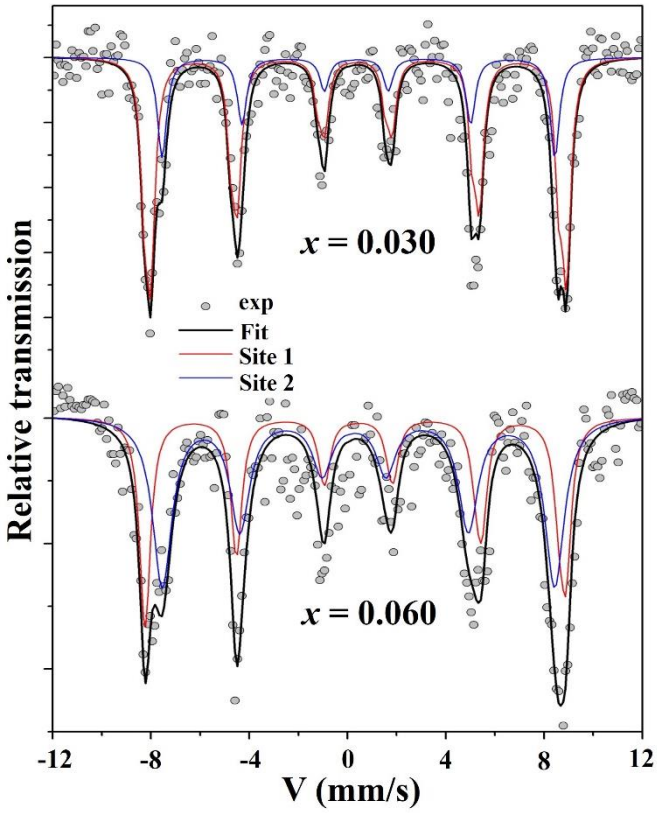

Figure 4.6 Mössbauer spectra at 77 K of $BiFe_{1-x}Al_xO_3$-$BaTiO_3$ ceramics with x = 0.030, 0.060.

Table 4.1 Mean refined values of hyperfine parameters obtained from Mössbauer spectra at 77 K of $BiFe_{1-x}Al_xO_3$-$BaTiO_3$ ceramics with x = 0.030, 0.060.

Sample	Site	isomer shift δ (mm/s) ± 0.01	quadripolar shift 2ε (mm/s) ± 0.01	hyperfine field B_{hf}(T) ± 0.5	Ratio (%) ± 2
x = 0.030	Sextet 1	0.52	0.01	52.3	74
	sextet 2	0.56	0.09	49.4	26
x = 0.060	sextet 1	0.52	-0.16	52.7	41
	sextet 2	0.51	0.18	49.3	59

4.4 Ferroelectric properties of BFA-BT

4.4.1 Polarization measurements

The Polarization of $BiFe_{1-x}Al_xO_3$-$BaTiO_3$ was measured under extrinsic electric field and reported in Fig. 4.7. The sample with x = 0.030 exhibits the highest spontaneous polarization P_s of 36.8 μC/cm^2 and remnant polarization P_r of 31.5 μC/cm^2 as shown in Tab. 4.2. The enhanced P_s and P_r polarization can be ascribed to the fact that the crystallographic orientation enables the alignment of the polar vectors more efficiently under applied electric field, contributing to the enhanced ferroelectric property. According to the analysis of XRD and SEM, a high ratio of c_T/a_T and large distortions of rhombohedral phase as well as high-density microstructures, contribute to the large polarization. However, with the further increase of Al^{3+} content (x = 0.045, 0.060), P_s and P_r of $BiFe_{1-x}Al_xO_3$-$BaTiO_3$ ceramics gradually decreased, and the ferroelectric properties gradually weakened. In addition, the coercive field of all $BiFe_{1-x}Al_xO_3$-$BaTiO_3$ samples is in the range of 33-38 kV/cm.

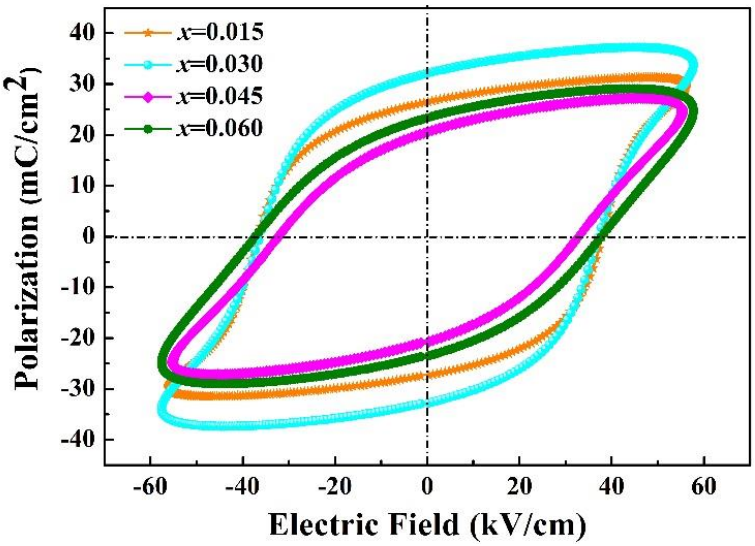

Figure 4.7 Polarization-electric field (*P*-*E*) loops of $BiFe_{1-x}Al_xO_3$-$BaTiO_3$ ceramics.

Table 4.2 Remnant polarization P_r, saturated polarization P_s, coercive field E_c of $BiFe_{1-x}Al_xO_3$-$BaTiO_3$ ceramics.

	***x* = 0.015**	***x* = 0.030**	***x* = 0.045**	***x* = 0.060**
Remnant polarization P_r	26.4	31.5	20.1	23.4
Saturated polarization P_s	30.8	36.8	26.5	25.3
Coercive field E_c	38.2	37.5	33.2	37.0

4.4.2 Electric field-induced strain

Strain of $BiFe_{1-x}Al_xO_3$-$BaTiO_3$ ceramics was measured under the extrinsic electric field and reported in Fig. 4.8. For low-doped samples (x = 0.015, 0.030), bipolar strain exhibits the characteristic butterfly shape with the high strain, at 0.12% and 0.11% respectively. For samples of $x \geq 0.045$, the bipolar strain decreased significantly to at 0.05%. It indicates that the ferroelectric performances of high-doped samples became weak, which is consistent with the behaviors of hysteresis loops.

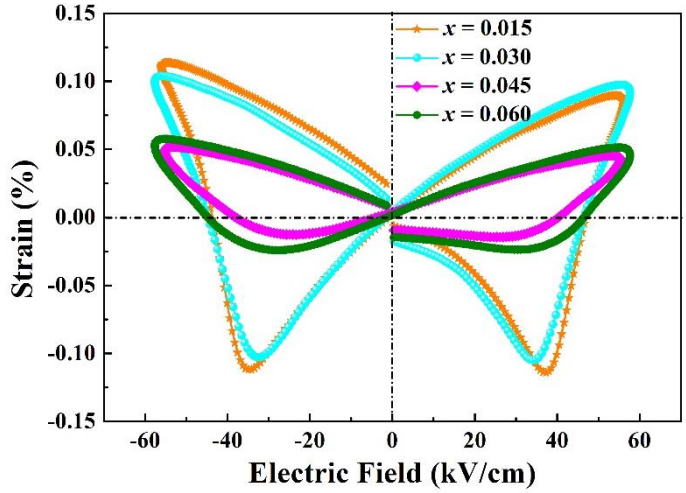

Figure 4.8 Bipolar strain-electric field (*S*-*E*) loops of $BiFe_{1-x}Al_xO_3$-$BaTiO_3$ ceramics.

4.4.3 Current curves

Fig. 4.9 exhibits the current curves of all BFA-BT samples shown. The current peaks are correlated with the switching of ferroelectric domains [118]. While for low Al-doped samples (x = 0.015, 0.030), the high value of the current peaks may indicate the large portions of ferroelectric domains switched under the electric field. The low value of the current peaks in high doping samples indicated that only small portion of domain switched. With the increasing content of Al^{3+}, the ferroelectricity of $BiFe_{1-x}Al_xO_3$-$BaTiO_3$ ceramics gradually became weak so that reduced densities of ferroelectric domains weaken the current peak.

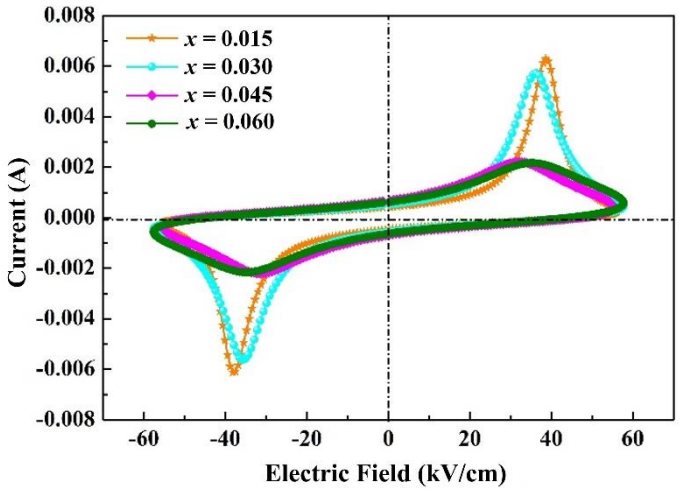

Figure 4.9 Current-electric field (*I*-*E*) loops of $BiFe_{1-x}Al_xO_3$-$BaTiO_3$ ceramics.

4.5 Dielectric properties of BFA-BT

4.5.1 Dielectric constants

Fig. 4.10 shows the dielectric constant ε at 10 kHz of $BiFe_{1-x}Al_xO_3$-$BaTiO_3$ in the temperature range from RT to 600 ℃. The Curie temperature (T_C) of samples slightly decreases with the addition of Al. The significant trend of the diffusive phase transition is observed in highly doped samples. The ionic radius of Al^{3+} (0.535 Å) is similar with Fe^{3+} (0.645 Å) and Ti^{4+} (0.605 Å) at B sites with the perovskite structure, compared with radius of Bi^{3+} (1.03 Å) and Ba^{2+} (1.35 Å) at A sites. The substitution of Al^{3+} contributes to the fluctuating occupation at B sites and then to more disordered structures. The Mössbauer spectrum in Fig. 4.6 and Tab. 4.1 also illustrates the more disorder structures of B sites because of the high Al^{3+} doping, contributing to the obvious diffuse phase transition.

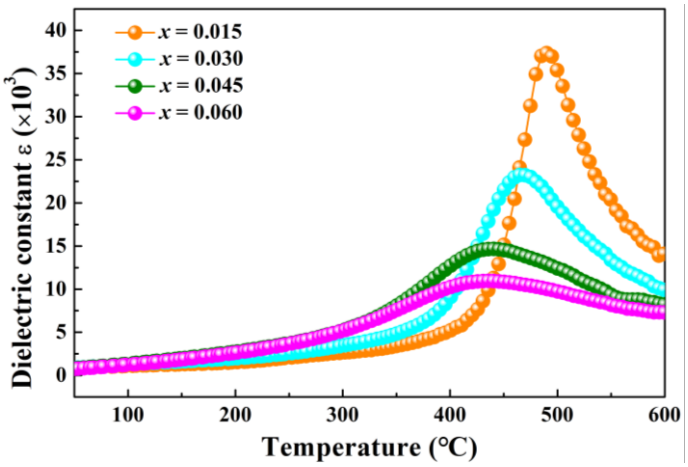

Figure 4.10 Temperature dependence of dielectric constants ε of $BiFe_{1-x}Al_xO_3$-$BaTiO_3$ ceramics at 10 kHz.

Fig. 4.11 shows the dielectric constant ε of $BiFe_{1-x}Al_xO_3$-$BaTiO_3$ as a function of temperatures at different frequencies with x = 0.015, 0.030, 0.045, 0.060. The increase of Al occupation at B sites contributes to a heterogeneous composition at the atomic scale. This leads to the obvious relaxation behavior because of the difference between the intrinsic dielectric effect which occurs from the lattice and the extrinsic dielectric effect emanating from the domains. Based on the previous analysis of microstructural characterization and ferroelectric performances, it can be considered that the disorder

degree of B sites in the $BiFe_{1-x}Al_xO_3$-$BaTiO_3$ sample also gradually increases with the increase of Al^{3+} content ($x \leqslant 0.030$), while the low disorder improves the distortion of lattices in the unit cell, which can improve the ferroelectricity of the materials. However, when the disorder degree of B sites is further increased ($x \geqslant 0.045$), not only will the growth of ceramic grains be inhibited, but the long-range ferroelectric ordered state in the ceramic will be destroyed (the macro ferroelectric domains gradually transfer to the nanodomains). Thus, normal ferroelectrics gradually change to relaxor ferroelectrics and the ferroelectricity of $BiFe_{1-x}Al_xO_3$-$BaTiO_3$ ceramics will gradually decrease with the increase of Al^{3+} content. Moreover, high-doped samples ($x \geqslant 0.045$) showing the significant diffuse phase transition and relaxation characteristics.

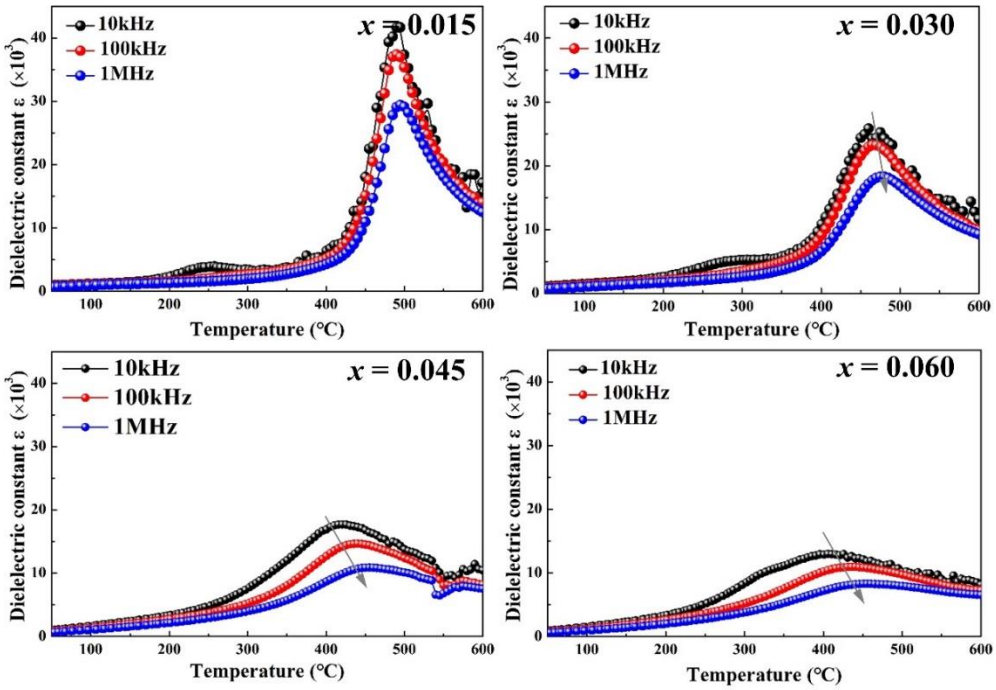

Figure 4.11 Temperature dependence of dielectric constants ε of $BiFe_{1-x}Al_xO_3$-$BaTiO_3$ with x = 0.015, 0.030, 0.045, 0.060 ceramics at 10 kHz, 100 kHz and 1 MHz.

4.5.2 Dielectric losses

Fig. 4.12 shows the dielectric loss tanδ of $BiFe_{1-x}Al_xO_3$-$BaTiO_3$ samples as a function of temperatures at 100 kHz with x = 0.015, 0.030, 0.045, 0.060. The dielectric loss tanδ in the low-doped samples (x = 0.015 and 0.030) showed a significant maximum

of losses around 400 ℃ at high temperature, which was related to the transition of the sample from the ferroelectric phase to the paraelectric phase. With the increase of Al^{3+} doping content ($x \geqslant 0.045$), the dielectric loss tanδ of $BiFe_{1-x}Al_xO_3$-$BaTiO_3$ samples gradually increases with the increasing temperature. There is no obvious maximum of losses for high-doped samples at high temperature. According to the analysis of the long-range ferroelectric state in the high-doped sample (that is, the macro ferroelectric domains gradually transfer to the nanodomains), the normal ferroelectric phase in the sample (x = 0.045 and 0.060) gradually transfers to the relaxor ferroelectric phase. Because of the relaxor structures in high-doped samples, the ferroelectric-paraelectric phase transition trend gradually weakens and the maximum of losses does not show obvious at high temperature shown in Fig. 4.12.

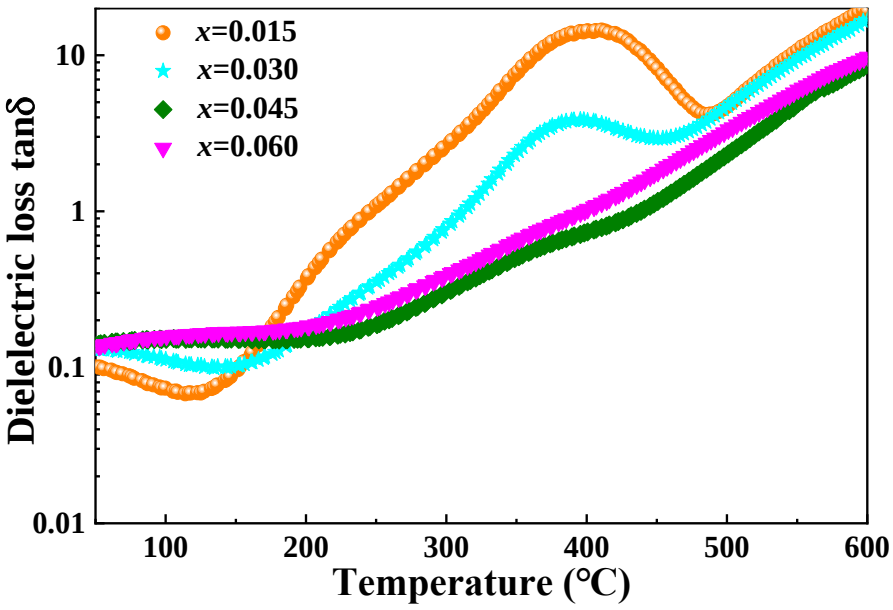

Figure 4.12 Temperature dependence of dielectric losses tanδ of $BiFe_{1-x}Al_xO_3$-$BaTiO_3$ ceramics at 100 kHz.

4.5.3 Relaxation behavior of BFA-BT

Imaginary modulus

Fig. 4.13 illustrates the imaginary modulus of $BiFe_{1-x}Al_xO_3$-$BaTiO_3$ ceramics as a function of frequencies and at different temperatures. According to phenomenological models, the relaxation behaviors involved in the modulus plots allow to evaluate smallest capacitances [119, 120]. For all samples, the imaginary modulus M''_{max} shifts

toward higher frequencies on increasing the temperature in agreement with thermally activated ionic motions. A continuous dispersion with increasing the frequency may be due to the short-range mobility of charge carriers, which indicates the obvious relaxation behavior in all samples. For low Al doping ($x \leq 0.030$) a single relaxation behavior is detected at low frequencies in the range of -60 ℃ - 200 ℃. For high Al^{3+} doped samples, two relaxation behaviors were observed on the whole measured temperature range. The microstructure of the samples as polycrystalline ceramics composed by grains and grain boundaries contribute to the electrical and dielectric behavior.

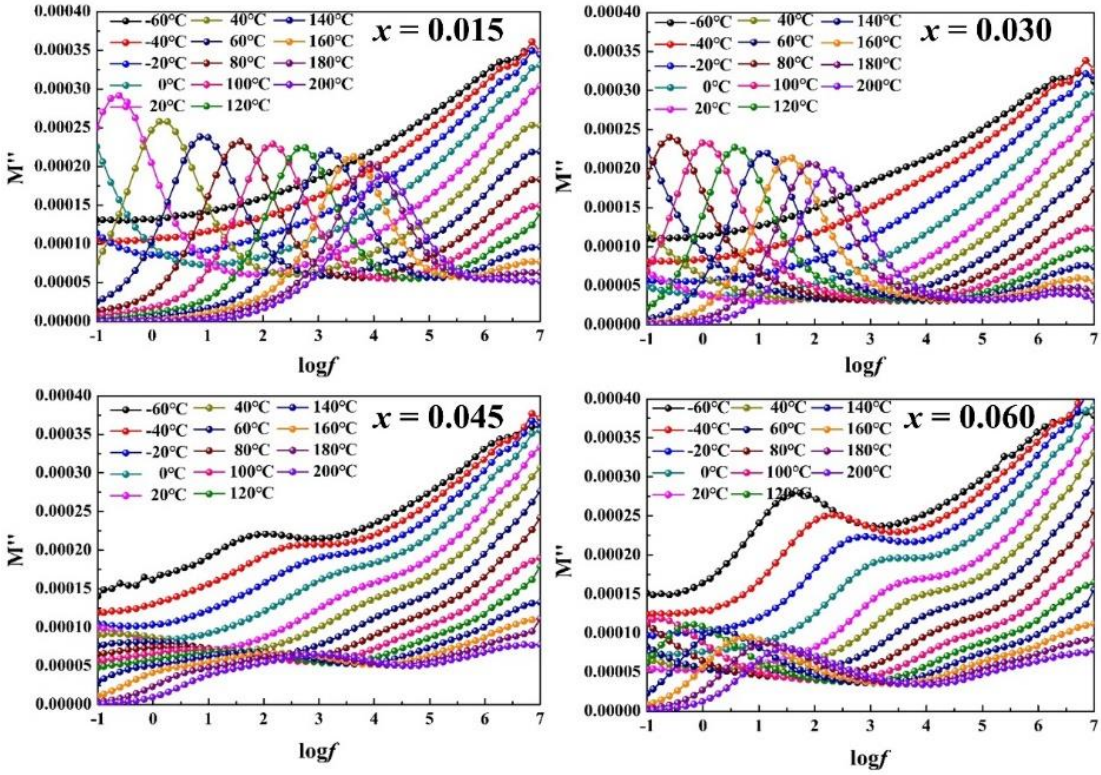

Figure 4.13 Imaginary modulus of $BiFe_{1-x}Al_xO_3$-$BaTiO_3$ ceramics as a function of frequencies measured at different temperatures with x = 0.015, 0.030, 0.045, 0.060.

Brick-wall model

According to brick-layer model, the contributions to dielectric functions are represented by combination of parallel resistor-capacitor RC elements which describe dipolar and charge carrier relaxations in Fig. 4.14 [121] [122]. In a system with two parallel RC circuits in Fig. 4.14, if two capacitances are relatively close, there will be

only one peak on the M'' plot. Or it will show two peaks when they are significantly different on the M'' plot. In general, the dielectric relaxation behaviors result from both the grain and grain boundaries as well. Thus, two different RC elements are required for samples with higher Al^{3+} content (x = 0.045, 0.060), which is consistent with the two different contributions. In general, the capacitance of ceramic grains and grain boundaries will be affected by the grain boundary thickness d and grain size D, the formula is as follows [156]:

$$\frac{C_{\mathrm{B}}}{C_{\mathrm{gb}}} = \frac{K_{\mathrm{B}}}{K_{\mathrm{gb}}}\frac{d}{D} \qquad \ldots(4.1)$$

Where C_B represents the capacitance of the bulks, C_{gb} represents the capacitance of the grain boundaries, K_B and K_{gb} are the constants related to the bulks and grain boundaries, respectively. It illustrates that the grain size and the thickness of grain boundaries in the ceramic will affect the capacitance of the grain boundaries and the grains, thereby affecting the dielectric relaxation response of the ceramics.

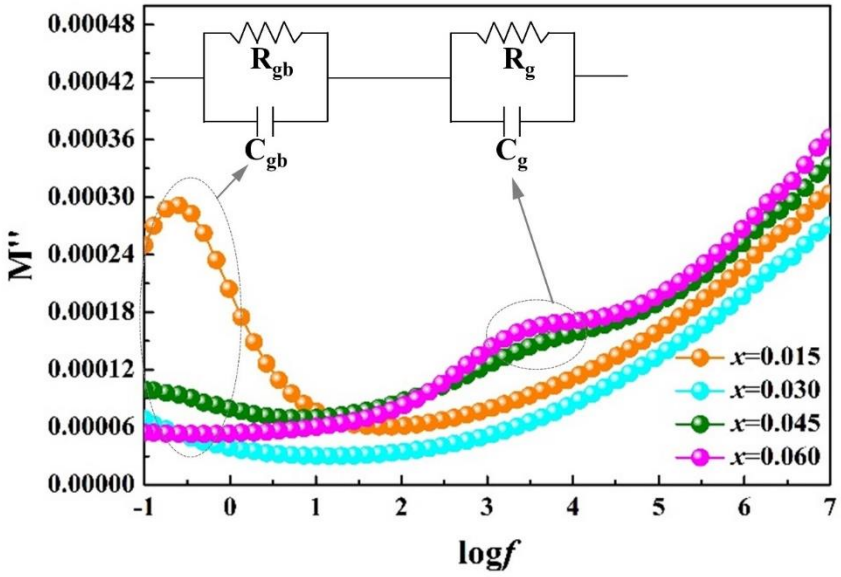

Figure 4.14 Imaginary modulus of $BiFe_{1-x}Al_xO_3$-$BaTiO_3$ ceramics versus different frequencies at room temperature and the model of parallel RC circuits.

In a former part, the "Brick-wall" model was utilized to account for two kinds of relaxation behaviours in $BiFe_{1-x}Al_xO_3$-$BaTiO_3$ ceramics. In order to further verify the difference of the capacitance between grains and grain boundaries, the EDS technique

is used. Fig. 4.15 depicts the EDS spectra of the samples with x = 0.015 and x = 0.045. Prior to the characterization, the samples were etched in order to prevent the impact from the thermal corrosion which is detrimental and can result in the rough surface of the tested samples. The element composition of spot 1 and spot 3 in grains of x = 0.015 and x = 0.045 were detected, which is close to the stoichiometric ratio of samples. However, the Bi element in spot 2 and spot 4 was higher than the stoichiometric ratio. It probably can be attributed to the formation of the second rich-Bi phase was formed surrounding grain boundaries, which then results in the difference of capacitance between grains and grain boundaries. In low Al-doped sample (x = 0.015), the portion of the second rich-Bi phase in grain boundaries was small, exhibiting one relaxation behavior. For the sample with higher Al-doped concentration (x = 0.045), the amount of the second rich-Bi phase in grain boundaries became high, which cannot be ignored. The sample exihibited two different dielectric relaxation behaviors, attributing to the effects of grains and grain boundaries.

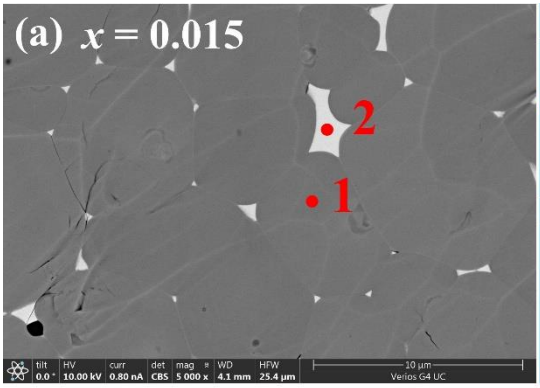

	Element	Weight %	Atomic %
Spot 1	Bi	45.41	14.55
	Fe	17.38	20.84
	Al	0.42	1.03
	Ba	19.89	9.70
	Ti	6.05	8.45
	O	10.85	45.42
Spot 2	Bi	83.21	36.00
	Fe	3.19	5.17
	Al	0.31	1.03
	Ba	2.59	1.70
	Ti	1.16	2.19
	O	9.54	53.91

	Element	Weight %	Atomic %
Spot 3	Bi	45.41	14.28
	Fe	17.35	20.41
	Al	0.34	0.83
	Ba	19.08	9.13
	Ti	6.53	8.95
	O	11.30	46.40
Spot 4	Bi	65.92	24.14
	Fe	8.99	12.31
	Al	0.62	1.76
	Ba	10.60	5.91
	Ti	3.29	5.25
	O	10.58	50.63

Figure 4.15 SEM patterns and distribution of grains and grain boundaries in $BiFe_{1-x}Al_xO_3$-$BaTiO_3$ ceramics, (a) x = 0.015, (b) x = 0.045.

Activation energy

The activation energies of the relaxation processes are shown in Fig. 4.16 and can be evaluated by using the Arrhenius law:

$$f_r = f_0 exp(-E_a/K_B T) \quad \ldots(4.2)$$

The pre-exponential factor is f_0, the Boltzmann constant K_B, the activation energy E_a for the hopping mechanism and the absolute temperature T. The activation energy E_a (0.68-0.81 eV) of the first relaxation behavior is attributed to the grain boundary effect at low frequencies [123]. The $BiFe_{1-x}Al_xO_3$-$BaTiO_3$ ceramics with x = 0.045 and 0.060 show a second relaxation process at high frequencies with an activation energy E_a (0.35-0.36 eV) attributed to the bulk (grain) effect of materials. Grain boundaries require higher activation energies than the grains for electrons hopping in the network. High-doped samples show the obvious segregation between grain and grain boundaries, contributing to significant differences in the dielectric relaxation related to the grain and grain boundaries.

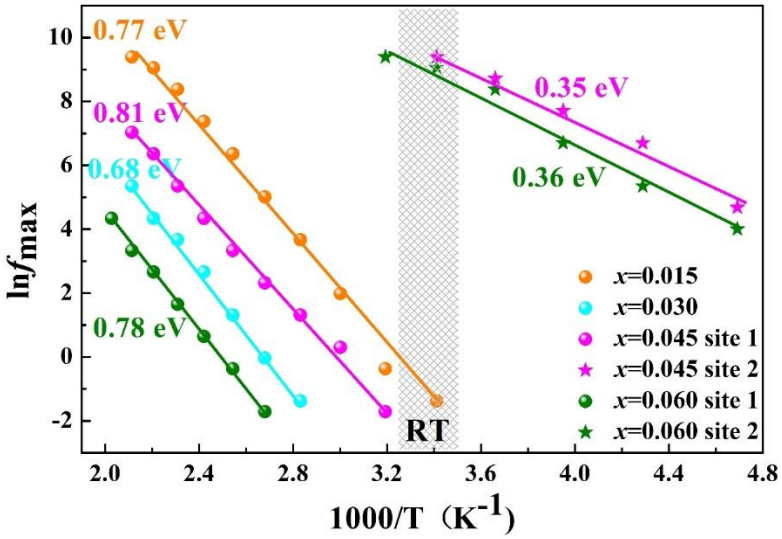

Figure 4.16 Activation energies of $BiFe_{1-x}Al_xO_3$-$BaTiO_3$ (x = 0.015, 0.030, 0.045, 0.060) ceramics.

4.6 Conclusions

In summary, conventional solid-state reaction was used to synthesize a series of Al-doped $BiFe_{1-x}Al_xO_3$-$BaTiO_3$ ceramic samples. The sample composition was optimized by tuning the Al content. With the doping content x = 0.030, a highest

spontaneous polarization and remnant polarization can be achieved at the values 36.8 μC/cm^2 and 31.5 μC/cm^2, respectively. The interplay of ferroelectric and dielectric properties were also studied in details and the main results are summarized below:

(1) A high-density microstructure decreases the leakage current of $BiFe_{1-x}Al_xO_3$-$BaTiO_3$. According to the XRD refinement results, a high c_T/a_T enhances the distortion of lattices under an applied electric field, which improves the polarization. We also found that the large distortion and the high fraction of the rhombohedral phase played essential role in the strength of the ferroelectric behavior.

(2) ^{57}Fe Mössbauer investigations indicated that the disorder of Fe^{3+} was increased after Al doping. By substitution of more nonmagnetic Al^{3+} in the crystalline host sites, a spectral component in the Mössbauer spectrum became broad due to increased disorder at B sites. Moreover, the valance state of Fe^{3+} was proved by the Mössbauer spectrum to be stable even if the Al ions are substituted in the near environment.

(3) The incorporation of Al ions in the host crystalline sites contributes to a diffuse phase transition $BiFe_{1-x}Al_xO_3$-$BaTiO_3$ as shown by the evolution of the dielectric constants versus temperatures. In particular, a high Al doping induces fluctuations of the occupation of B sites and then strengthen the disorder in the samples at atomic scale as inferred from Mössbauer spectra.

(4) Highly doped samples give rise to two distinct dielectric relaxation behaviors emanating from the effects of grains and grain boundaries. The element segregation was pointed out by EDS characterizations and correlates with a higher capacity difference between the grains and grain boundaries. Therefore, two kinds of dielectric relaxation behaviors are involved. Thus, the relevance of Al doping in BFA-BT structures is clearly demonstrated through the modulation of the crystalline phase, the microstructures of the ceramics and their ferroelectric responses. The potential application of the doped ceramics is a matter of further developments.

Chapter 5 Microstructures and properties of <001> textured Ga doped $BiFeO_3$-$BaTiO_3$ (BFG-BT)

5.1 Introduction

For several decades, the PZT (lead zirconate titanate) family has been the icon of a large class of technologically important piezoelectric materials. A wide set of investigations are currently developed on PZT in the piezoelectric scientific community irrespective to the environment concerns [1] [2] [77]. This is a serious drawback of PZT which faces nowadays to global restrictions due to toxic Pb element. Thus it is crucial to develop lead-free substitutes as technologically analogous alternative to PZT. In the light of such context, an extensive attention has been diverted to sustainable lead-free piezoelectric materials [108, 109, 124].

A relevant approach to achieve high piezoelectricity is to place the stoichiometry of the material to the morphotropic phase boundary (MPB). Liu et al. investigated the $Ba(Ti_{0.8}Zr_{0.2})O_3$-$(Ba_{0.7}Ca_{0.3})TiO_3$ compound possessing a giant piezoelectric coefficient d_{33} (620 pC/N) and analyzed the C-R-T (cubic-tetragonal-rhombohedral) triple point of the MPB [7]. However, an ultra-low Curie temperature (T_C = 93 ℃) within this system still hampered it to cope with practical applications. In particular, a large electromechanical strain at the high temperature is essential for high-temperature piezoelectric actuator applications. A recent report paid a great attention to the high-performance $BaTiO_3$-$Bi(Mg_{1/2}Ti_{1/2})O_3$-$BiFeO_3$ (BMT-BF) ceramics showing a highly effective piezoelectric constant d_{33}* of 799 pm/V for the V-doped samples and T_C remained more than 460 ℃ [125]. Nevertheless, V-doped BMT-BF has not attracted noticeable attention due to the environmental concern on the toxic vanadium based oxides. Recently, KNN-based materials showed a giant piezoelectric constant 570 pC/N, but the T_C remained less than 200 ℃ [102]. An improvement was achieved by Wu et al. with the formulae $(1-x-y)K_{1-w}Na_wNb_{1-z}Sb_zO_3-xBiFeO_3-yBi_{0.5}Na_{0.5}ZrO_3$ where a giant piezoelectric coefficient d_{33} of 550 pC/N and a higher T_C to 237 ℃ were realized [2]. Although a

high performance and T_C of lead-free materials were achieved, it is particularly difficult to ensure a mass production of such complex compositions for a practical application. For instance, a large piezoelectricity (d_{33} = 402 pC/N) together with a high T_C (454 ℃) have been reported in $BiFeGaO_3$–$BaTiO_3$ (BFG-BT) ceramics. This makes BFG–BT material systems as promising lead-free candidates [6]. However, lower piezoelectric performances (less than 200 pC/N) had also been noticed toward the same composition, which can be ascribed to the tiny difference of traditional solid-state method. Meanwhile, extensive studies have also been reported to improve the piezoelectric performance of lead-free materials by sol-gel [126-128], spark plasma [129-131], laser sintering [132, 133], two-step sintering method and so on [134-137]. However, the improvement of preparation methods was not significant to enhance the piezoelectric constant.

With the development of the processing route relative to <001> textured polycrystals, the electric-field-induced strain of lead-free ceramics was comparable to typical actuator-grade PZT. Crystallographic texturing of piezoelectric ceramics can be achieved by a reactive template grain growth (RTGG) process, which allows the utilization of inherent anisotropy in material properties. Meanwhile, the application of domain engineering is also potentially capable to address the aforementioned challenges in modified BT-based ceramics [138-141]. In light of the concept of domain engineering, a significantly enhanced piezoelectric response could be expected in the highly textured rhombohedral structure.

In this chapter, textured BFG-BT ceramics were studied for the microstructures and ferroelectricity via the reactive template grain growth method. Microstructures and nanodomains were systematically investigated by SEM, EDS, TEM measurement. The oriented grains and distortion of the rhombohedral phase contributed to the excellent ferroelectric properties of the textured sample. The BFG-BT textured sample exhibited superior electric-field induced strain at high temperature, the d_{33}* at 180 ℃ achieved 685 pm/V. This work provided the important guidance for the application of lead-free piezoelectric materials in the high temperature range.

5.2 Synthesis of textured and untextured BFG-BT ceramics

Templates preparation

Plate-like BT particles were synthesized by topochemical reaction method with the processing protocol described in previous reports [67, 69]. $Bi_4Ti_3O_{12}$ particles were first synthesized by reacting Bi_2O_3 with TiO_2 in NaCl/KCl flux at 1120 ℃ for 1 h. Second, $BaBi_4Ti_4O_{15}$ particles were formed by reacting the $Bi_4Ti_3O_{12}$, $BaCO_3$ and TiO_2 in $BaCl_2$/KCl molten salts at 1080 ℃ for 1 h. The compound $BaBi_4Ti_4O_{15}$ were washed with the deionized water and the pure plate-like $BaBi_4Ti_4O_{15}$ particles were then reacted with $BaCO_3$ in KCl flux at 950 ℃ for 3 h. The Aurivillus structures of plate-like $BaBi_4Ti_4O_{15}$ particles were transformed to the platelet $[001]_c$ BT templates in the molten-salt process. After removing the salt inside BT templates, the redundant Bi_2O_3 was also thoroughly removed by washing templates with 3 M HNO_3 solution. Finally, platelet-like BT templates were obtained with lengths/widths around 5-10 μm and thicknesses about 0.5-1.2 μm.

Preparation of BFG-BT ceramics

Textured $0.67Bi_{1.05}Fe_{0.97}Ga_{0.03}O_3$-$0.33BaTiO_3$ (BFG-BT) ceramics with 5 wt.% BT templates were synthesized by RTGG process. For blank comparison, randomly oriented BFG-BT ceramics without any BT templates (random-1 BFG-BT) were synthesized by a conventional solid-state method. Taking $BaTiO_3$ composition into consideration, randomly oriented BFG-BT ceramics with 5% BT templates (random-2 BFG-BT) were also prepared by the same solid-state method without tape casting. Powders of Bi_2O_3, Fe_2O_3, Ga_2O_3, $BaCO_3$ and TiO_2 were used as the raw materials, and 5% excess Bi_2O_3 was added into the composition for the compensation of bismuth loss during sintering. For the RTGG process, the calcined BFG-BT powders were mixed thoroughly with triethyl phosphate as a dispersant in a solution of an ethanol and methyl ethyl ketone (MEK) by ball milling for 0.5 h. Polyvinyl butyral as a binder and polyethylene glycol/diethyl-o-phthalate as a plasticizer were added to the mixtures and then ball milled again for 3 h. BT templates were added to the mixtures with 5 wt.% content to form tape casting slurry. This process led to a green sheet with

a blade height of 60 μm at a rate of 0.5 m/min. After drying, the tapes were cut, stacked, laminated at 75 ℃ and 70 MPa for 0.5 h to form disk-like samples of diameter 12 mm. The disk samples were de-waxed at 550 ℃ for 6 h and the organics were removed by heating the samples. Then the samples were sintered at 1010 ℃ for 5 h in air.

Material characterizations

The microstructures of the samples were examined with a FESEM (Hitachi S4800). The crystalline structures of samples were investigated by XRD using an Empyrean-Panalytical equipment in the 2θ range of 20°-100 °, operating at 40 kV, 30 mA with Cu Kα1 ($\lambda = 1.5406$ Å) and Cu Kα2 ($\lambda = 1.5444$ Å) lines. HR-TEM observations were carried out using a JEOL ARM200F instrument operated at 200 kV accelerating voltage. The polarization-electric field (*P*-*E*) hysteresis loops and the electric field-induced strain of textured and random BFG-BT ceramics were measured by a modified Sawyer-Tower circuit at different temperature (10 Hz, TF Analyzer 2000, aixACCT Systems GmbH, Aachen, Germany). The dielectric permittivity and loss (tanδ) of the ceramics were measured as a function of the temperature using an impedance analyzer (Agilent 4192A).

5.3 Structural and organization of BFG-BT phases

5.3.1 Microstructures

Fig. 5.1(a)-(c) show the backscattered electron microstructures (BSE) of fractured surface microstructures of random and textured ceramics. Fig. 5.1(d) shows the grain sizes and relative densities of these samples. The average grain size is about 7 μm for the random-1 sample. However, with the addition of BT templates, the grain size decreases rapidly down to 2 μm in random-2 and textured samples. In Fig. 5.1(a) and (b), the large grains like BT templates in random-2 and textured samples could be observed. As a result, the mass diffusion of Bi, Fe, Ga elements contributed to the reaction of BT templates and matrix powders, forming the large grains similar to templates. The size of large grains is close to that of BT templates shown in Fig. 5.1(b)

and (c), which is about 8 μm reported in the other literature [73]. As for textured sample, these matrix powders grew along to <001> orientation of BT templates, forming the oriented grains.

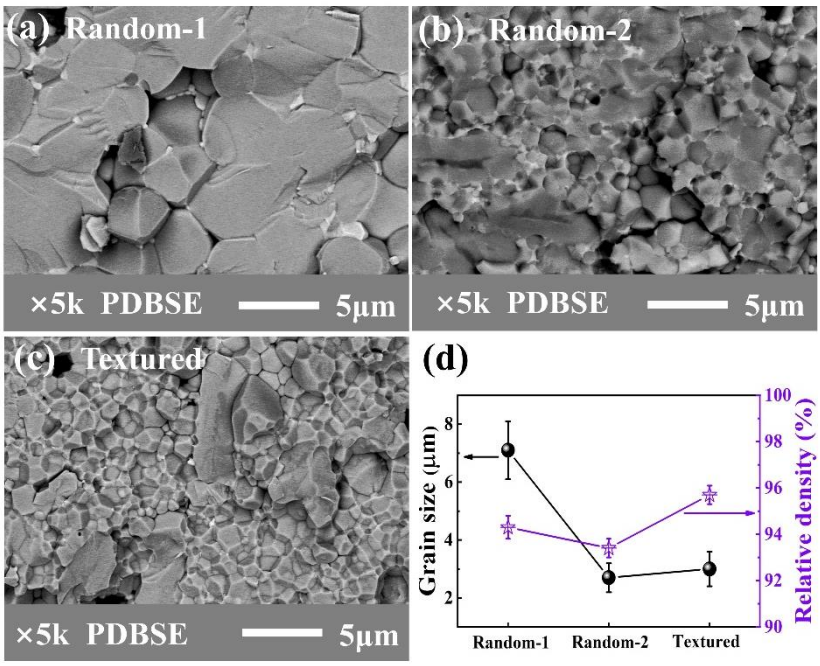

Figure 5.1 BSE microstructures of BFG-BT samples, (a) Random-1 sample, (b) Random-2 sample, (c) Textured sample. (d) Grain sizes and relative densities of BFG-BT samples.

Fig. 5.2 shows the EDS measurement to clarify the element distribution of abnormal large grains in textured samples. The contents of Ba^{2+} and Ti^{4+} elements are much higher in the 5th and 7th areas in Fig. 5.2, indicating that BT templates did not disappear completely in the grains after sintering. The growth of some matrix powders was reduced to 2 μm from large-size BT templates. For the textured system, although the growth of most grains was inhibited, these matrix powders still grew along <001> direction surrounding <001> templates, forming the oriented grains.

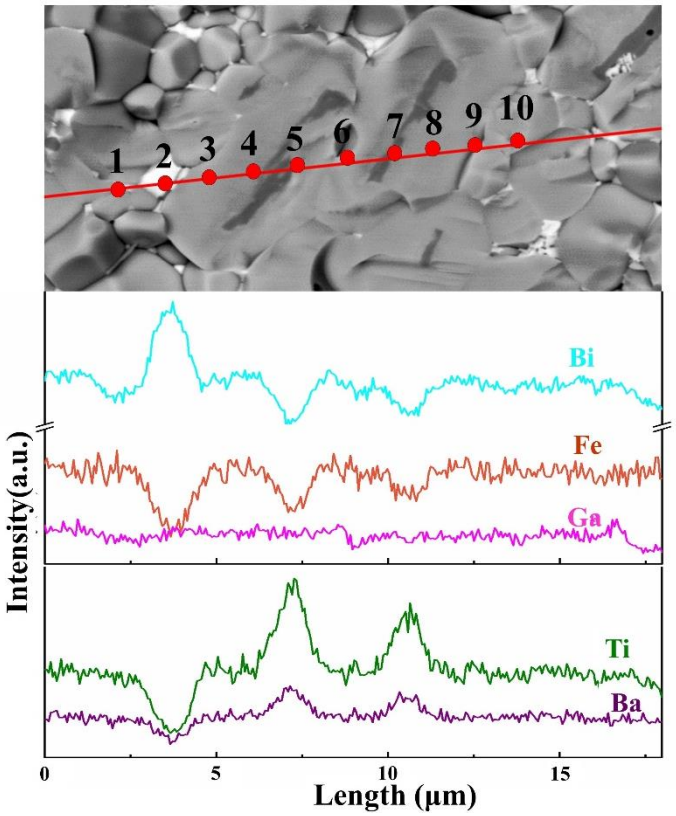

Figure 5.2 SEM patterns and distribution of elements of textured BFG-BT ceramics.

5.3.2 Structural features and thermal evolution

The XRD patterns of the textured samples, which were prepared with different sintering method, are presented in Fig. 5.3. Generally, sintering time should not be lower than 5 h as required time for a matrix to evolve the templates. It is noteworthy that the orientation factor of the samples will not show further increase, even if the sintering time is as high as 10 h. Therefore, the sintering time of 5 h is considered to be ideal to achieve the most oriented textured sample. The quenching process is also verified to be inoperative to enhance the orientation. By comparing the XRD patterns of the template and textured samples, one can see that the introduction of BT template contributes to the oriented crystal growth, but it does not alter the crystal structure of the samples. In the following study, the textured samples are investigated after being sintered for 5 h.

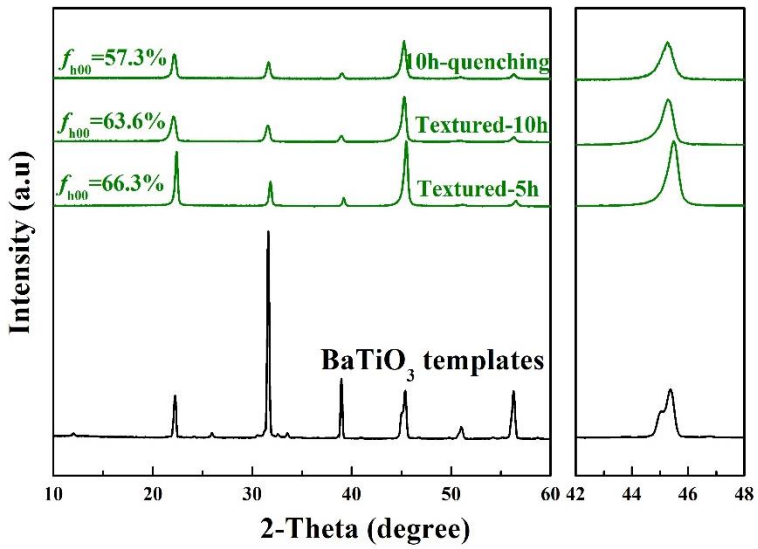

Figure 5.3 XRD patterns of textured BFG-BT with different sintering methods.

The Rietveld refinement of XRD patterns was conducted to clarify the crystalline phase features. It is obvious that textured BFG-BT materials show a <00*l*> orientation factor compared with randomly-oriented materials, reaching 66.3%, i.e. the textured degree computed by Lotgering factor method, in Fig. 5.4 [66]. The orientation grains contributed to the reduction of the misorientation angle in the textured sample. In agreement with our recent work [142], optimal fits of the XRD patterns were achieved using a combination of the space groups *R*3c and *P*4mm in Fig. 5.5(a)-(c). The reliability factor R_{wp} (the subscript "wp" means "weighted profile") for each composition is about 10%, indicating a high relevance of the refinement. The rhombohedral phase fraction of textured ceramics (98%) is higher than that of random-1 (87%) and random-2 samples (81%). The textured sample has the same components with the random-2 sample, however the arrangements of their templates were different. Templates reacted with the matrix of ceramic powders during the process of sintering.This reaction may be influenced by the arrangements of their templates. Finally, the portion of *R*3c phase in the textured ceramics was higher than that in randomly-oriented samples. It is known that the rhombohedral *R*3c phase is polar as it is also but weakly for the tetragonal phase is weakly polar phase. The high distortion and the high amount of the rhombohedral phase in textured ceramics enhancing the polarization.

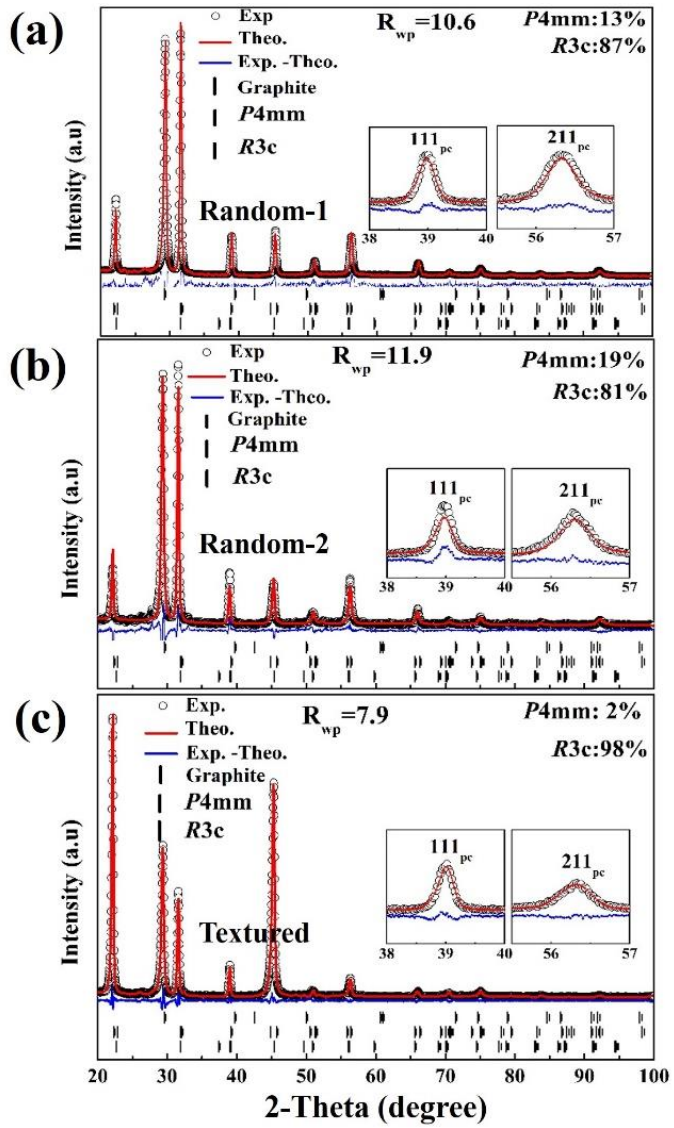

Figure 5.4 XRD patterns with Rietveld refinement of different BFG-BT samples, (a) Random-1 sample, (b) Random-2 sample, (c) Textured sample.

In order to explain the different fraction of the rhombohedral *R*3c phase in different BFG-BT samples, Fig. 5.5 shows the model of the grain growth process of different BFG-BT samples during the sintering process. For the random-1 sample without $BaTiO_3$ (BT) templates, there are certain different compositions from the other two samples with addition of BT templates, so that there is a certain different fraction of the *R*3c phase. As shown in Fig. 5.5(a), the grains in the random-1 powder grow up through absorbing small grains, eventually result in the large grain size. As shown in Fig. 5.5(b), the BT templates in random-2 powders are randomly arranged and the process of grain growth is hindered by BT templates, resulting in a smaller grain size

in the sample. And BT templates also reacted with some green powders, affecting the *R*3c phase of grains to a certain extent. As shown in Fig. 5.5(c), the BT templates in the textured powders are oriented by tape-casting. During the sintering process, the BT templates could sufficiently react with most BFG-BT powders. The grains could grow along the direction of the BT templates. The grain growth of textured powders in Fig. 5.5(c) is divided into two categories. The first type is that BT templates serves as a seed to provide driving force for the grain growth. Element diffusion occurs between the powders and the BT templates. The grain grows along the <001> orientation of the templates with the smaller size, the grain growth of the textured BFG-BT sample belongs to the first category. The second type is that powder grows epitaxially along the templates to form larger grains than templates. Such large-sized grains can be observed in textured PMN-PT ceramics [65]. Although the random-2 sample maintains the same composition as the textured sample, the reactive degree between BT templates and the powders leads to a certain different fraction of the rhombohedral *R*3c phase.

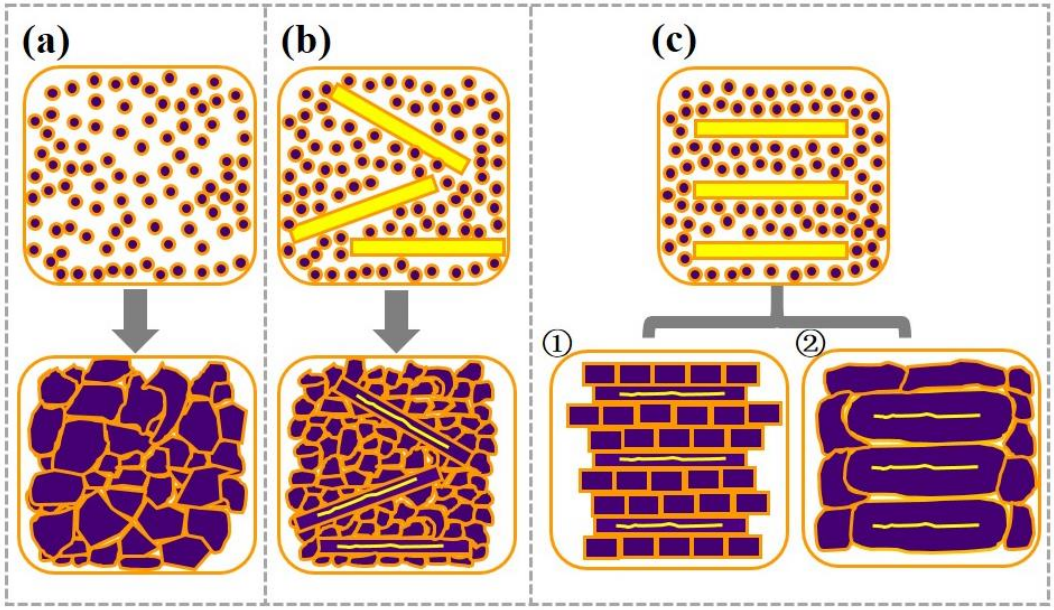

Figure 5.5 Model of the grain growth process of different BFG-BT samples, (a) Random-1 sample, (b) Random-2 sample, (c) Textured sample.

Figure 5.6 shows the XRD patterns of the textured and untextured (random-1) BFG-BT samples. Compared to the random-1 sample, the XRD of the textured

sample shows the different intensity. According to the Lotgering method, the <001> orientation degree of the textured sample is 66.3% [66]. The oriented grains in the textured sample help to reduce the angle between the external electric field and the direction of spontaneous polarization and reduce the stress difference between adjacent grains, which is more conducive to domain switching under the electric field. Thus, oriented grains further improve the ferroelectric properties of textured samples [25].

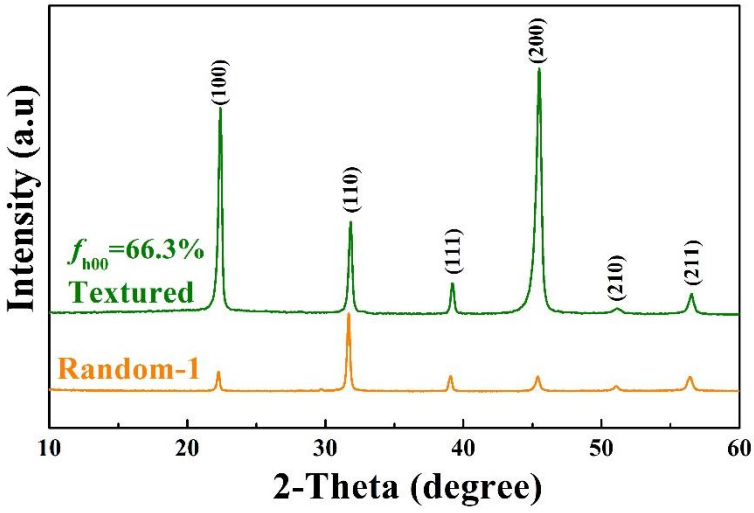

Figure 5.6 XRD patterns of textured BFG-BT and Random-1 samples.

There is no phase transition from ferroelectric phase with *R*3c and *P*4mm phases to paraelectric phase with cubic structure up to 300 ℃ as supported in Fig. 5.7(a)-(c). The ferroelectric response of samples is well ensured at high temperature. In Fig. 5.8, the XRD results at different temperatures indicate only a slight increase of the structural parameters (a_R, a of the unit cell in the rhombohedral phase) because of the thermal expansion.

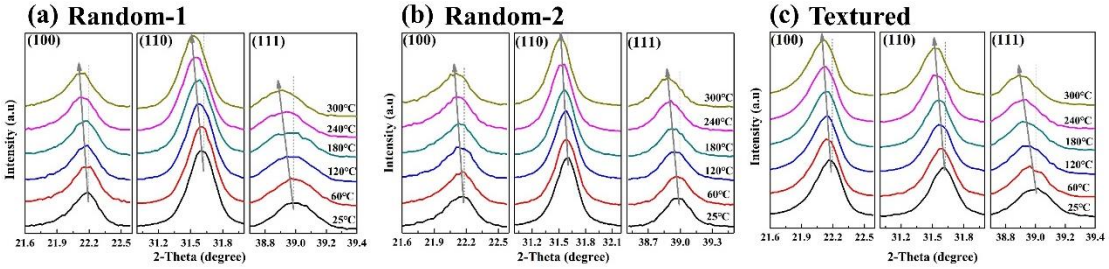

Figure 5.7 Evolution of (100), (110), (111) peak position of all samples from room temperature to 300 ℃

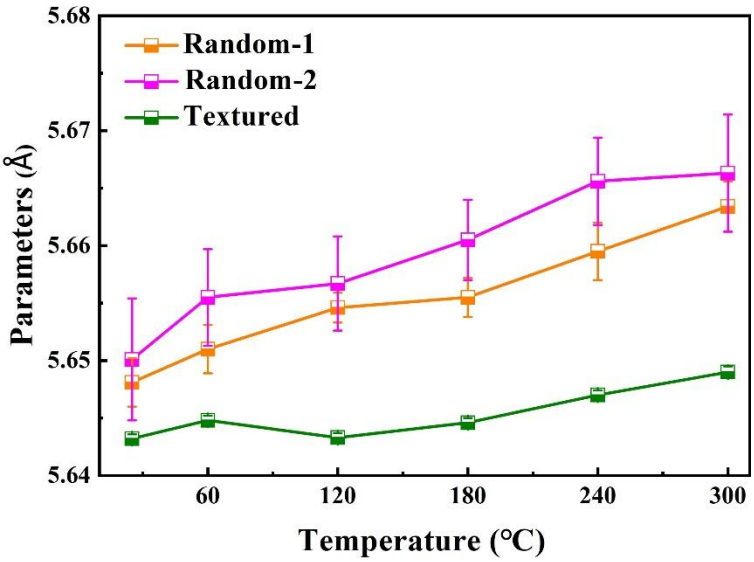

Figure 5.8 Variation of *a* as a function of temperature of the rhombohedral phase in random and textured BFG-BT samples.

The magnitude of the thermal expansion coefficients were calculated by the following relation:

$$\alpha_T^a = \frac{1}{a_0}\frac{da}{dT} \quad \ldots(5.1)$$

Here a_0 is the initial lattice parameter, which can be used to estimate the thermal expansion coefficient α_T^a at different temperatures shown in Fig. 5.9. In general, the linear thermal expansion coefficient of lead piezoelectric ceramics is located at the 10^{-6} order of magnitude, whereas it can approach 10^{-5} for some $BiFeO_3$-based ceramics [143, 144]. More precisely, α_T^a was estimated to be lower than 3×10^{-5} for all the considered samples.

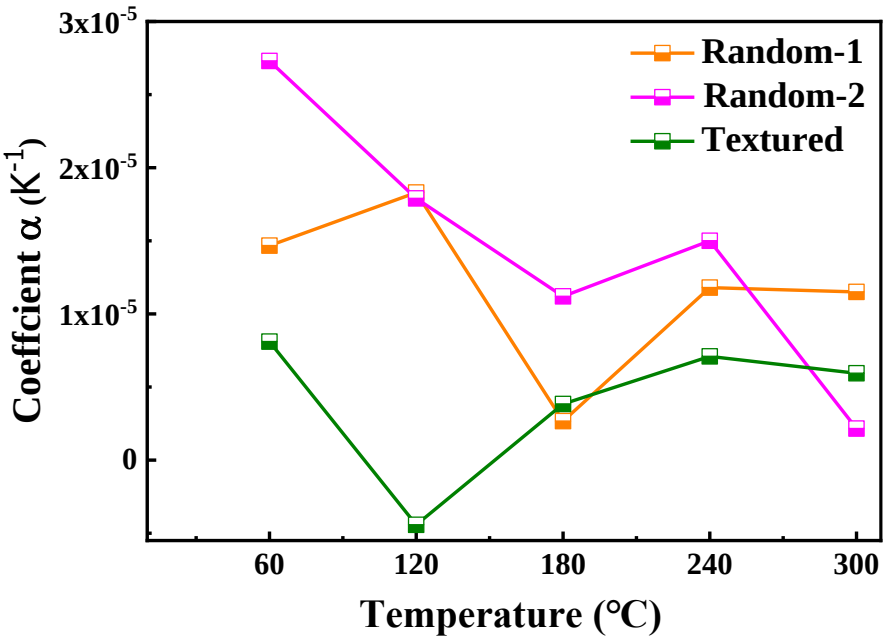

Figure 5.9 Thermal expansion of lattice parameter a as a function of temperature in random and textured BFG-BT samples

5.3.3 The structure of nanodomains

Fig. 5.10 reports TEM bright field images showing the domain configurations of textured ceramics. Stripe-like domains, composed of high-density nanodomains with the size about 2.4 nm, are clearly observed in textured sample. The high-resolution transmission electron microscopy (HR-TEM) image of lattice fringes in Fig. 5.11(a) demonstrates a good crystalline quality of textured sample at the nanoscale. Fig. 5.11(b) shows the SAED patterns taken from the grain in Fig. 5.11(a). Lattice planes (128), (10$\bar{2}$), (226) and interplanar distances are consistent with the standard PDF card (*R*3c phase). It also confirms the rhombohedral phase structure of the textured sample, which is in accordance with the Rietveld refinement result of the XRD patterns.

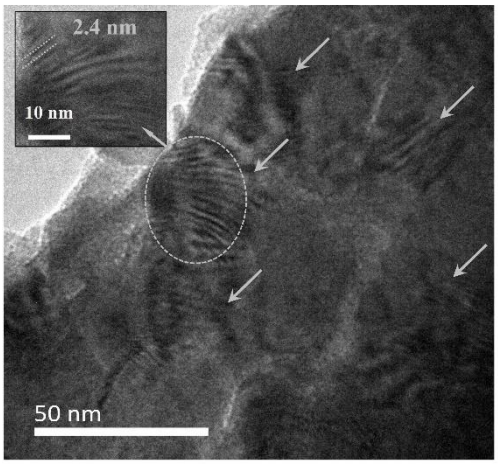

Figure 5.10 TEM bright field images of domain configurations of textured BFG-BT sample.

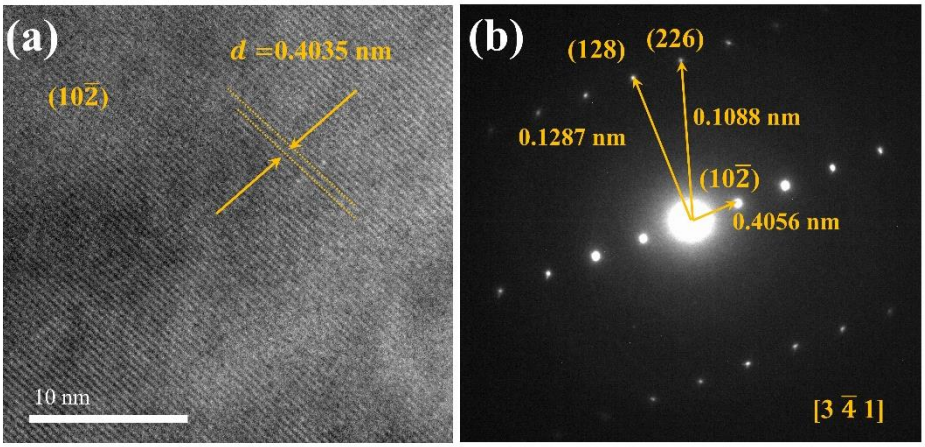

Figure 5.11 The HR-TEM image of textured BFG-BT sample, (a) lattice fringes, (b) SAED patterns from lattice fringes.

The distribution of nanodomains in all samples are shown in Fig. 5.12 where untextured samples exhibit few nanodomains in the unit area. It has been reported that the high-density nanodomains in textured sample is adequate to enhance the electric field-induced strain [25, 102]. Since the nanodomains with low domain wall energies are favorable for domain wall motions under an applied electric field.

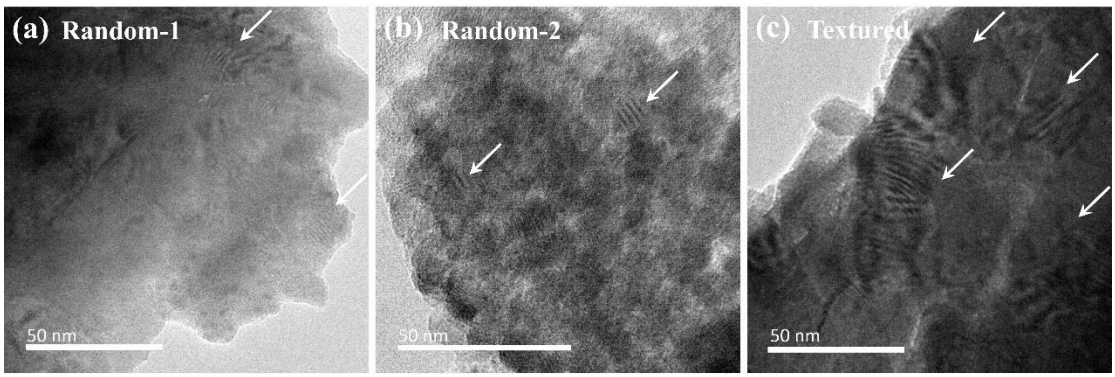

Figure 5.12 TEM bright field images of domain configurations of BFG-BT samples at room temperature, (a) Random-1 sample, (b) Random-2 sample, and (c) Textured sample.

5.4 Ferroelectric properties versus temperatures in BFG-BT

5.4.1 Polarization measurements

Fig. 5.13 illustrates the polarization-electric field (*P*-*E*) hysteresis loops at different temperatures at 10 Hz. Random-1 sample showed higher remnant polarization (P_r) and coercive field (E_c) than other two samples below 90 ℃. The high leakage current in random-1 sample resulted in the breakdown at high temperature.

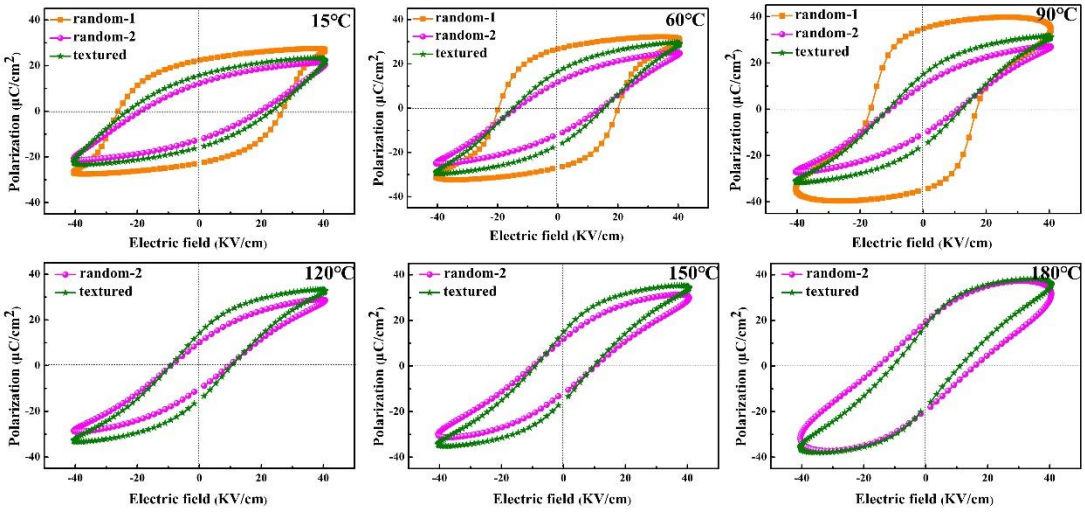

Figure 5.13 Polarization-electric field (*P*-*E*) hysteresis loops of BFG-BT ceramics measured at different temperatures.

Fig. 5.14 shows the remnant polarization P_r of three sample at different temperatures. As for textured sample, the stable remnant polarization (17 μC/cm^2) is maintained with increasing the temperature, higher than that of random-2 sample (12 μC/cm^2).

The stable ferroelectric domains contribute to the stable remnant polarization at different temperatures. The configuration of nanodomains enhances the polarization of textured sample under an extrinsic electric field with increasing temperature, compared with random-2 sample. On the other hand, an easy movement of nanodomains in textured ceramics lowers the coercive field with increasing the temperature. The hysteresis loop of random-2 sample becomes unusual at 180 ℃ because of the high leakage current. For perovskite materials, the major intrinsic defect is the oxygen vacancy which supplies the charge carrier for the leakage current under applied field [145]. However, polarization of textured samples could retain stable until 180 ℃ as a consequence of a low leakage current, which means that oxygen vacancies get decreased.

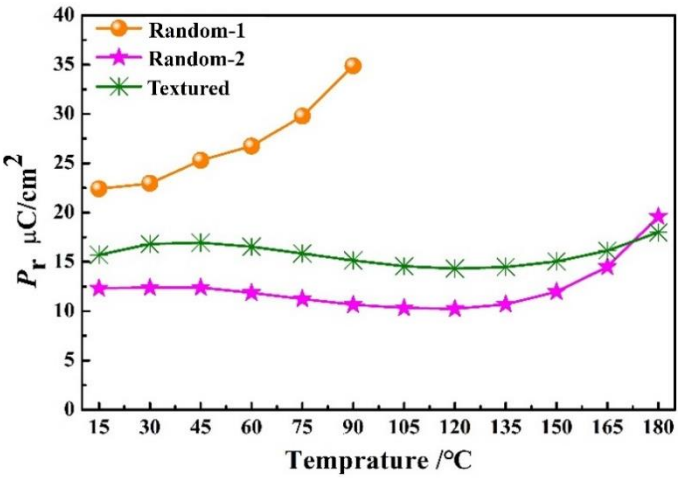

Figure 5.14 Different remnant polarizations P_r of BFG-BT samples with increasing temperatures.

5.4.2 Electric field-induced strain

Fig. 5.15(a)-(c) show the unipolar strain and d_{33}* as a function of the temperature of random BFG-BT and textured BFG-BT. The latter sample shows a unipolar strain reaching 0.27 % under 40 kV/cm and 180 ℃. Fig. 5.15(d) shows the effective piezoelectric coefficient d_{33}^* from the results in Fig. 5.15(a)-(c). The effective piezoelectric coefficient d_{33}* increases with increasing the temperature and remains rather high at 690 pm/V from 150 ℃ to 180 ℃, manifesting substantial piezoelectricity. It is shown that the unipolar strain of textured sample doubles that of random-2 sample in Fig. 5.15(a), which was reported by <001> textured PMN-PT

ceramics at room temperature [146]. Usually, the high strain of ferroelectric materials originates from the intrinsic piezoelectric strain caused by the lattice distortion and the extrinsic piezoelectric strain caused by domain switching [147, 148]. As for the textured sample, the high distortion of the rhombohedral phase as well as the easy rotation of oriented domains contributes to the large displacement in the external electric field with increasing temperature. But for random-1 and random-2 samples, the configuration with low fraction of rhombohedral phase and random domains leads the small displacement. The nanodomains of textured samples are also favorable for the domain motion, providing an enhanced electrostrain [6].

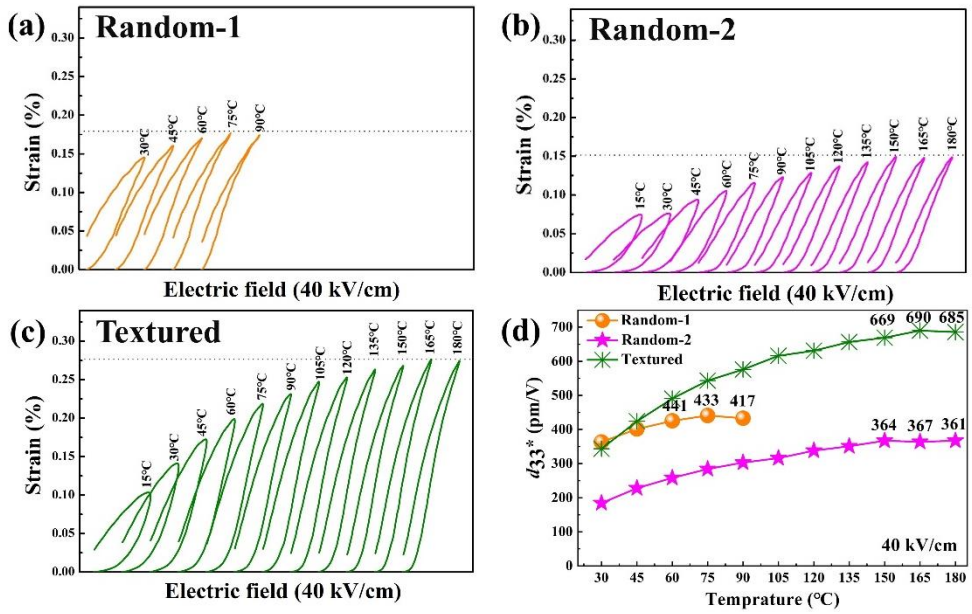

Figure 5.15 Bipolar strain-electric field (S-E) loops of BFG-BT samples, (a) Random-1 sample, (b) Random-2 sample, (c) Textured sample. (d) Effective piezoelectric coefficient d33* of BFG-BT samples with increasing temperatures.

Fig. 5.16 shows the P_{max}^2-P_r^2 of BFG-BT samples recorted at different temperatures at 40 kV/cm. We could obtain the unipolar strain S_{uni} from the remnant and maximum polarization as follows:

$$S_{uni} = S_{max} - S_r = QP_{max}^2 - QP_r^2 = Q(P_{max}^2 - P_r^2) \quad \ldots(5.2)$$

Where P_{max} is the maximum electric-field-induced polarization and P_r is the remnant polarization which remains stable with the temperature variation in textured ceramics. However, the value of P_{max} increases with increasing the temperature resulting in the

high S_{uni}, which is consistent with a high electromechanical strain d_{33}*. It is found that the $(P_{\mathrm{max}}^2 - P_{\mathrm{r}}^2)$ in Fig. 5.16 follows the same tendency as the d_{33}* in Fig. 5.15(d). Thus, the configuration of nanodomains enhanced the polarization P_{max} under an extrinsic electric field with increasing temperature.

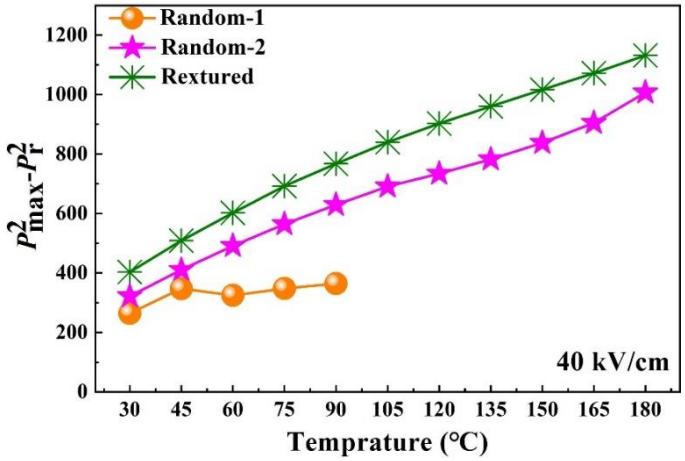

Figure 5.16 P_{max}^2-P_r^2 of BFG-BT samples recorted at different temperatures at 40 kV/cm.

As shown in Fig. 5.17, the d_{33}* of textured sample at 10 kV/cm was close to that in Fig. 5.15(d) at 40 kV/cm, since nanodomains and oriented grains contributed to easy domain wall motion even under a low electric field. The domains switching and domain wall motion for random-1 and random-2 samples were more difficult at lower electric field which limit the piezoresponse.

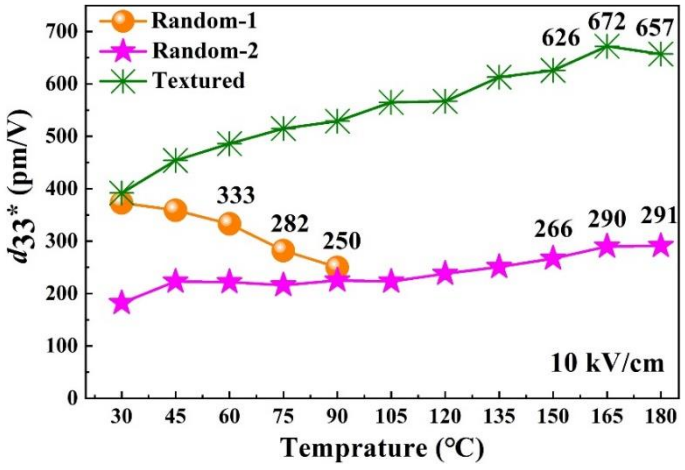

Figure 5.17 Effective piezoelectric coefficient d_{33}* and P_{max}^2-P_r^2 of BFG-BT samples recorted at different temperatures.

5.5 Dielectric properties of BFG-BT

5.5.1 Dielectric constants

Fig. 5.18(a)-(c) show the temperature dependence of the dielectric losses in the random and textured BFG-BT materials from 100 Hz to 100 kHz. The random-1 sample exhibited the highest dielectric losses, that is, tanδ increased quickly when the measurement temperature was above 100 ℃. The first peak of the dielectric constants in random-1 sample, is consistent with the involvement of oxygen vacancies as reported in other random $BiFeO_3$-$BaTiO_3$ systems [142]. The second dielectric peak demonstrates a dielectric relaxation features with a wide distribution of relaxation frequencies in all samples. With the introduction of BT templates, the first peak is absent in random-2 and textured materials attributing its origin to the weak contribution of oxygen vacancies, which was consistent with the hysteresis loops. It is worth noting that the dielectric constant peak at T_m of all samples increases to the high temperature as frequencies increase, which especially shows the typical relaxor ferroelectric nature with the addition of BT templates in Fig. 5.18(b)-(c). Such behavior can be attributed to the disorder of the composition with the addition of BT templates.

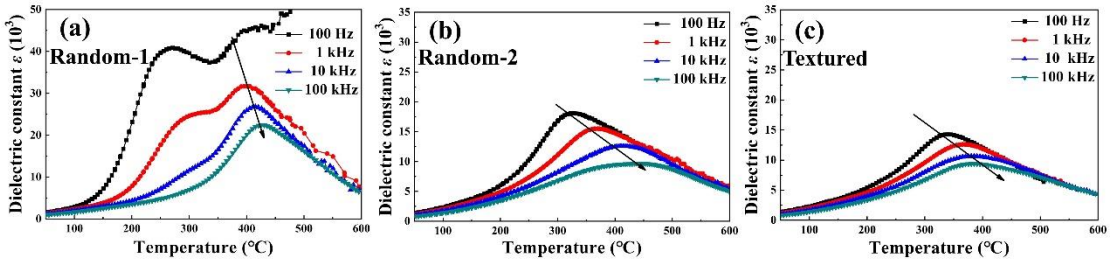

Figure 5.18 The temperature dependence of the dielectric constant as a function of frequencies of three samples

Fig. 5.19 shows the temperature dependence of the dielectric constant of random and textured BFG-BT ceramics as 10 kHz. Random-1 sample exhibits the high value of maximum dielectric constants (T_m). With the addition of BT templates, T_m of random-2 and textured samples declines due to the disorder of lattices with the addition of BT templates.

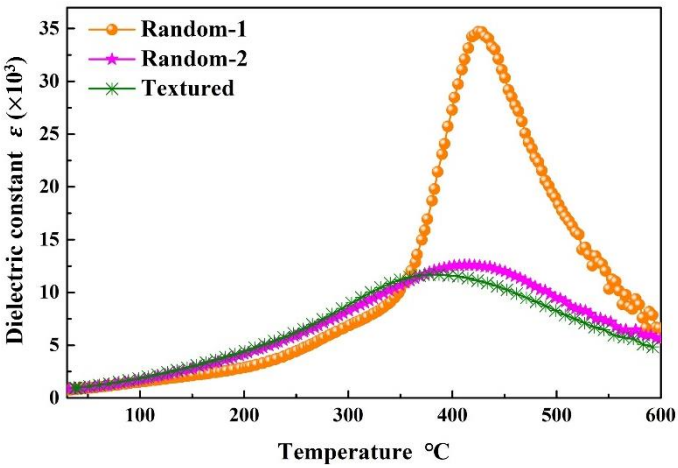

Figure 5.19 The temperature dependence of the dielectric constant of random and textured BFG-BT ceramics as 10 kHz

Fig. 5.20(a)-(c) show the temperature dependences of the inverse of the relative dielectric permittivity for the random and textured BFG-BT materials. At temperatures above their Burn temperatures (T_B), the dielectric responses of three samples obey the Curie-Weiss law, corresponding to a paraelectric phase. For the textured sample, T_B = 480 ℃ is higher than that of random-1 (449 ℃) and random-2 sample (465 ℃). The high density nanodomains in textured sample may shift T_B to higher values. However, the dielectric constant of all samples could not obey the normal Curie-Weiss behavior below T_B.

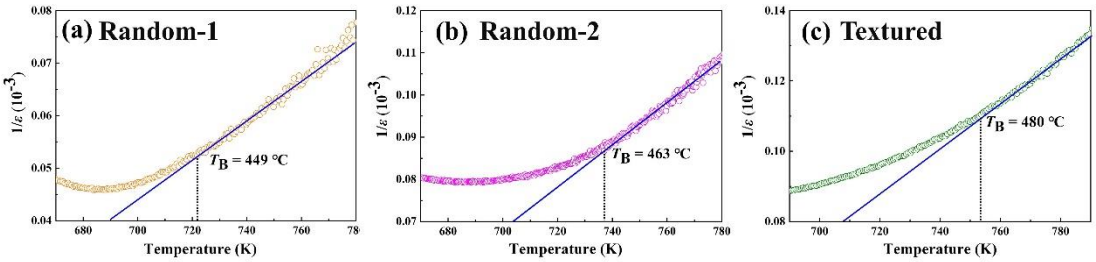

Figure 5.20 Temperature dependence of the reciprocal of relative dielectric permittivity of BFG-BT samples, (a) Random-1 sample, (b) Random-2 sample, (c) Textured sample.

The diffuseness which obeys to a scaling law with a universal critical exponent could be estimated as function of the sample features in Fig. 5.21. The modified empirical expression proposed by Uchino and Nomura [149] is as follows:

$$\left(\frac{1}{\varepsilon_r}\right) - \left(\frac{1}{\varepsilon_m}\right) = A(T - T_m)^{\gamma} \quad \ldots(5.3)$$

Where ε_m is the maximum value of the dielectric constant and T_m, A is assumed to be Curie-like constant, γ represents the critical exponent of diffuseness and ranges from 1 for a normal ferroelectric to 2 for an ideal relaxor ferroelectric. The degree of random-2 sample (γ = 1.98) and textured sample (γ = 1.88) were higher than that from the random-1 sample (γ = 1.63). The incorporation of BT templates increases the disorder of the host lattice and induces a diffuse character to the phase transition. The broadening of the dielectric peak was also related to the use of BT templates which enhanced the short-range lattice structures.

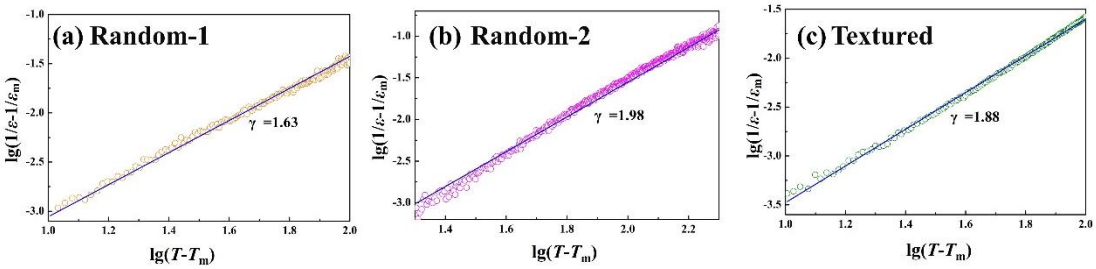

Figure 5.21 The $\log(1/\varepsilon - 1/\varepsilon_m)$ versus $\log(T - T_m)$ curves at temperatures above T_m of BFG-BT samples, (a) Random-1 sample, (b) Random-2 sample, (c) Textured sample.

5.5.2 Dielectric losses

Fig. 5.22(a)-(c) show the temperature dependence of the dielectric losses of random and textured BFG-BT materials from 100 Hz to 100 kHz. It was observed that the random-1 sample exhibits the highest dielectric losses, that is, tanδ increased quickly above 100 ℃. As the first peak of dielectric constants was attributed to oxygen vacancies as reported in other random $BiFeO_3$-$BaTiO_3$ systems [142], this assignment is also consistent with the behavior of high dielectric losses in random-1 sample.

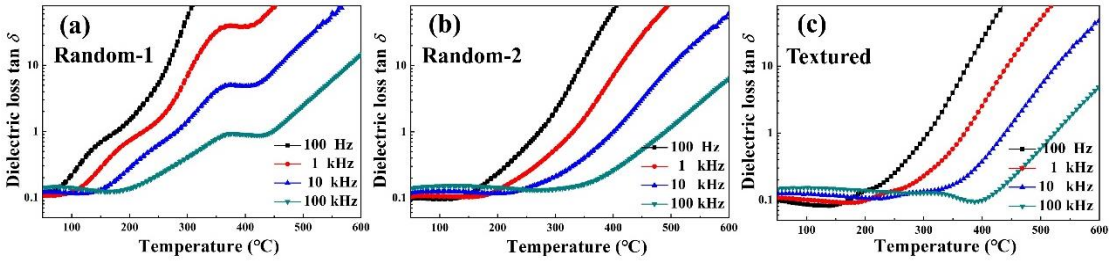

Figure 5.22 Temperature dependence of dielectric losses tanδ at different frequencies of BFG-BT samples, (a) Random-1 sample, (b) Random-2 sample, and (c) Textured sample.

5.6 Conclusions

In summary, the microstructures and performances were systematically investigated over the randomly oriented samples doped with BT template and the textured sample. The BFG-BT textured sample exhibited superior electric-field induced strain at high temperature, i.e. d_{33}* = 685 pm/V at 180 ℃. This value is twice high compared to that in the untextured sample in the same measurements conditions. Detailed conclusions are summarized below:

(1) The oriented rhombohedral phase and the high-density of nanodomains play essential roles in upgrading the strain of the textured products. In addition, the low energy barrier induced by nanodomains was found also prone to reduce the coercive field. The remnant polarization of the textured sample was stable at 17 μC/cm^2 at the temperature from room-temperature to 180 ℃.

(2) Extra configuration of nanodomains enhanced the polarization P_{max} in the extrinsic electric field with increasing the temperature. The d_{33}* of textured sample at 10 kV/cm was close to that at 40 kV/cm, indicating that nanodomains and oriented grains contributed to easy domain wall motion even under low electric fields. Thus, textured sample shows the high electric-field induced strain compared to untextured samples.

(3) The introduction of BT templates enhanced the diffuse degree of the ceramic, and the Burn temperature of the textured sample reaching 480 ℃ due the involved high-density of nanodomains. The dielectric losses decrease in the textured ceramic which provides more stable performances at high temperature compared to the

pristine sample.

This study revealed that the novel textured system is a promising solution to enhance efficiently the ferroelectric properties for promising applications in piezoelectric actuators working at high temperatures.

Chapter 6 General Conclusions and Perspective

6.1 Conclusions

The first part of the presented work was dedicated to PSL$(ZT)_{1-x}$-Fe_x ceramics with different compositions and fabricated by the conventional solid-state reaction method. The ferroelectric performances with softening-hardening features were also realized by modulating the La/Fe ratio. By adjusting the sintering temperature, phase structures, microstructures and electric properties were systematically analyzed in PSL$(ZT)_{1-x}$-Fe_x samples with an emphasis on the softening-hardening transition and the specific features at different doping ratios.

In a second contribution, $BiFeAlO_3$-$BaTiO_3$ (BFA-BT) systems were investigated for their ferroelectric performances along with environmental friendly lead-free materials. The synthesis was performed by the conventional solid-state method. Doping was carried out by using Al^{3+} ions to ensure the optimized performance in lead-free BFA-BT materials. Exhaustive investigations and their analysis were performed to shed light on the microstructures, dielectric and ferroelectric properties of the doped BFA-BT systems. On the other hand, the reactive templated grain growth method (RTGG) was utilized to synthesize textured $BiFeGaO_3$-$BaTiO_3$ (BFG-BT) lead-free ceramics. The realized textured samples revealed better performances illustrated by an enhanced electric field-induced strain twice high compared to that in untextured materials. The main achievements of this PhD thesis work are summarized below:

(1) PSL$(ZT)_{1-x}$-Fe_x ceramics were investigated in details with respect to microstructures and piezoelectric properties highly dependent on the Fe^{3+} doping ratio. The structural features phase of samples with the features of a tetragonal phase and a coexistence of the tetragonal and rhombohedral phase with increasing Fe^{3+} concentration. Specifically, when La/Fe ratio surpassed 1 (soft doping), the polarization-electric field (*P*-*E*) hysteresis loop shows apparent highly saturated, being indicative of soft materials. In this situation, the strain of the sample was larger and revealed the high hysteresis because of the easy switching of ferroelectric

domains. It is noteworthy that the sample (x = 0) revealed the optimized piezoelectric constant of 412 pC/N and dielectric constant up to 1480. By increasing the Fe^{3+} content as La/Fe $\leq$ 1, the polarization shows pinning effects which manifests through the double *P*-*E* hysteresis loop with low strain and hysteresis. This behavior is indicative of hard materials. Meanwhile, mechanical quality factor Q_m achieved its high value at 500. Compared with the strain induced by switching of domains in soft materials, the strain in hard materials exhibits low values. After poling hard materials, defect dipoles P_D and spontaneous polarization P_s aligned along the electric field leading to higher polarization and strain.

(2) The temperature dependence of piezoelectric properties in PSL$(ZT)_{1-x}$-Fe_x, high-ratio La/Fe (soft) samples evidences the temperature-stable electromechanical coupling coefficient K_p and Q_m. The latter factor in hard samples, increases substantially at high temperature as a consequence of the impedance decrease at the resonance. The proposed mechanism is based on the mobility of oxygen vacancies which minimizes the impedance of hard samples at high temperatures. This approach open the way for piezoelectric actuators required for applications at high temperatures.

(3) For $BiFe_{1-x}Al_xO_3$-$BaTiO_3$ (BFA-BT) system, the spontaneous P_s and remnant polarization P_r of x = 0.030 reach their highest values at of 36.8 μC/cm^2 and 31.5 μC/cm^2, respectively. The corresponding sample shows a high distortion of the rhombohedral phase as well as a high c_T/a_T ratio when an electric field upraises the polarization. Mössbauer investigations revealed that a high Al doping could induce enhanced disorder of atoms at the B sites. As consequence, the second Mössbauer sub-spectrum broaden with increasing nonmagnetic Al doping ratios and then increases the disorder in B sites. Meanwhile, the samples with high Al^{3+} doping revealed significantly the diffused phase transition in agreement with the analysis of Mössbauer spectra. From dielectric measurements, the sample with high Al doping ratios shows two distinct dielectric relaxation behaviors. The “Brick-wall” model was used to analyze the different relaxation profiles by contributions from grains and grain boundaries.

(4) <001> textured $BiFeGaO_3$-$BaTiO_3$ (BFG-BT) ceramics were fabricated by the reactive templated grain growth. The textured materials show superior ferroelectric performances in high-temperature compared with untextured ceramics. Efficient piezoelectric constants d_{33}* of 685 pm/V at 180 ℃ was achieved in the textured sample. For the textured samples, nanodomains lower the energy barriers of domain walls and favors the easy switch of domains. Moreover, textured samples revealed temperature-stable polarization, which almost retained at 17 μC/cm^2 from room-temperature to 180 ℃. At high temperature, the easy mobility of nanodomains contributed to a partial P_{max} in the textured sample along with a low coercive field in textured ceramics. The high fraction of the rhombohedral phase contributed to large displacement in the samples. Thus, d_{33}* of the textured sample revealed the same tendency versus temperature in the low electric field and high electric field. Meanwhile, <001> orientation of textured samples reduced angles between the electric field and spontaneous polarization, and decreased stress among grains. Owing to effects of microstructures, novel textured samples revealed excellent ferroelectric properties at high temperature. This research opens the development window for the application in high-temperature ferroelectric actuators.

6.2 Perspective

PZT and BF-BT ceramics were investigated and innovative ferroelectric properties were achieved. The approaches combine hard and soft doping through the ratios La/Fe for PZT and Al doping along with the use of templates to realize textured ceramics. The microstructures, crystalline phases and sintering conditions were modified to modulate the ferroelectric responses. Consistent analyses were developed and discussed on the two families of efficient ferroelectrics but some relevant issues are also deserved to further focus on the considered systems.

(1) “Defect dipoles” model was discussed on the PZT doped systems based on the analysis of electrical properties in poled and unpoled states. To define the local coordination, the concentration and the local electronic structure of defects such as Fe_{Ti} or Fe_{Ti}-V_O, EPR technique is a powerful method to determine the above features.

Moreover, polarized Raman microprobe spectroscopy is also an attractive tool for assessing microscopic domain orientation in unpoled and poled PZT ceramics. The results of electric properties will be more convincing through the direct detection of domain switching by polarized Raman method.

(2) In BF-BT lead-free system, it is relevant to analyze whether other ion doping can cause the diffused phase transition and relaxation behaviors. Therefore, doping engineering by selected species may optimize the performance of BF-BT systems. Moreover, Raman spectra are sensitive to the lattice structure and structural defects of ferroelectric ceramics. In the future, Raman spectra can be used to analyzing phase structures and structural disorder induced by defects in doped ferroelectric ceramics.

(3) Since ferroelectric performances and their stability at high temperatures depend highly on the synthesis route to realize textured samples, the structural and morphology of BT templates and the sintering process are worthy of interest . The optimization of the piezoelectric responses can be achieved by increasing the densities of textured ceramics. The dielectric relaxation behaviors in textured BFG-BT systems are relevant as well as their analysis in correlation with the microstructure and grain morphology of the ceramics. Finally, it is expected that the optimized lead-free BFG-BT systems can be applied into high-temperature actuators.

Finally the valorization of textured systems in terms of innovative applications must be explored based on the achieved knowledge from the present work.

Bibliography

[1] Rubio-Marcos F, Lopez-Juarez R, Rojas-Hernandez R E, et al. Lead-Free Piezoceramics: Revealing the Role of the Rhombohedral-Tetragonal Phase Coexistence in Enhancement of the Piezoelectric Properties [J]. ACS Applied Materials & Interfaces, 2015, 7(41): 23080-8.

[2] Wu B, Wu H, Wu J, et al. Giant Piezoelectricity and High Curie Temperature in Nanostructured Alkali Niobate Lead-Free Piezoceramics through Phase Coexistence [J]. Journal of the American Chemical Society, 2016, 138(47): 15459-64.

[3] Zhou J E, Yan Y, Priya S, et al. Computational study of textured ferroelectric polycrystals: Texture development during templated grain growth [J]. Journal of Applied Physics, 2017, 121(6): 064108-18.

[4] Yan Y, Yang L, Zhou Y, et al. Enhanced temperature stability in <111> textured tetragonal $Pb(Mg_{1/3}Nb_{2/3})O_3$-$PbTiO_3$ piezoelectric ceramics [J]. Journal of Applied Physics, 2015, 118(10): 104101-11.

[5] Yan Y, Zhou J E, Maurya D, et al. Giant piezoelectric voltage coefficient in grain-oriented modified $PbTiO_3$ material [J]. Nature Communications, 2016, 7(0): 13089-97.

[6] Lee M H, Kim D J, Park J S, et al. High-Performance Lead-Free Piezoceramics with High Curie Temperatures [J]. Advanced materials, 2015, 27(43): 6976-82.

[7] Liu W, Ren X. Large piezoelectric effect in Pb-free ceramics [J]. Physical Review Letter, 2009, 103(25): 257602-05.

[8] Pandey D, Singh A K, Baik S. Stability of ferroic phases in the highly piezoelectric $Pb(Zr_xTi_{1-x})O_3$ ceramics [J]. Acta Crystallographica Section A: Foundations of Crystallography, 2008, 64(1): 192-203.

[9] Matsubara M, Yamaguchi T, Sakamoto W, et al. Processing and Piezoelectric Properties of Lead-Free (K,Na) (Nb,Ta)O_3 Ceramics [J]. Journal of the American Ceramic Society, 2005, 88(5): 1190-6.

[10] Zhang S, Xia R, Shrout T R, et al. Piezoelectric properties in perovskite $0.948(K_{0.5}Na_{0.5})NbO_3$-$0.052LiSbO_3$ lead-free ceramics [J]. Journal of Applied Physics, 2006, 100(10): 104108.

[11] Wu J, Xiao D, Zhu J. Potassium-sodium niobate lead-free piezoelectric materials: past, present, and future of phase boundaries [J]. Chemical Review, 2015, 115(7): 2559-95.

[12] Liu W, Ren X. Large piezoelectric effect in Pb-free ceramics [J]. Physical Review Letters, 2009, 103(25): 257602.

[13] T. T, K. M, K. S. $(Bi_{1/2}Na_{1/2})TiO_3$-$BaTiO_3$ System for Lead-Free Piezoelectric Ceramics. [J]. Japanese Journal of Applied Physics, 1991, 30(9B): 2236-9.

[14] Sasaki A, Chiba T, Mamiya Y, et al. Dielectric and Piezoelectric Properties of $(Bi_{0.5}Na_{0.5})TiO_3$-$(Bi_{0.5}K_{0.5})TiO_3$ Systems [J]. Japanese Journal of Applied Physics, 1999,

38(9): 5564-7.

[15] Shrout T R, Zhang S J. Lead-free piezoelectric ceramics: Alternatives for PZT? [J]. Journal of Electroceramics, 2007, 19(1): 113-26.

[16] Rödel J, Jo W, Seifert K T P, et al. Perspective on the Development of Lead-free Piezoceramics [J]. Journal of the American Ceramic Society, 2009, 92(6): 1153-77.

[17] Zeng W, Zhou C, Xiao J, et al. Correlation between temperature-dependent permittivity dispersion and depolarization behaviours in Zr^{4+}-modified $BiFeO_3$–$BaTiO_3$ piezoelectric ceramics [J]. Bulletin of Materials Science, 2015, 38(7): 1737-41.

[18] N. Murayama, K. Nakamura, H. Obara, et al. The strong piezoelectricity in polyvinylidene fluroide (PVDF) [J]. Ultrasonics, 1976, 14(1): 15-24.

[19] Ueberschlag P. PVDF piezoelectric polymer [J]. Sensor Review, 2001, 21(2): 117-25.

[20] Eom C-B, Trolier-McKinstry S. Thin-film piezoelectric MEMS [J]. MRS Bulletin, 2012, 37(11): 1007-17.

[21] Chang Y, Wu J, Sun Y, et al. Enhanced electromechanical properties and phase transition temperatures in [001] textured $Pb(In_{1/2}Nb_{1/2})O_3$-$Pb(Mg_{1/3}Nb_{2/3})O_3$-$PbTiO_3$ ternary ceramics [J]. Applied Physics Letters, 2015, 107(8): 082902-7.

[22] Duran C, Dursun S, Akça E. High strain, <001>-textured $Pb(Mg_{1/3}Nb_{2/3})O_3$–$Pb(Yb_{1/2}Nb_{1/2})O_3$–$PbTiO_3$ piezoelectric ceramics [J]. Scripta Materialia, 2016, 113(0): 14-7.

[23] Raevskaya S I, Zakharov Y N, Lutokhin A G, et al. Critical nature of the giant field-induced pyroelectric response in $Pb(Mg_{1/3}Nb_{2/3})O_3$–$xPbTiO_3$ single crystals [J]. Applied Physics Letters, 2008, 93(4): 042903-6.

[24] Kumar A, Bhanu Prasad V V, James Raju K C, et al. Ultra high strain properties of lanthanum substituted PZT electro-ceramics prepared via mechanical activation [J]. Journal of Alloys and Compounds, 2014, 599(0): 53-9.

[25] Li P, Zhai J, Shen B, et al. Ultrahigh Piezoelectric Properties in Textured $(K,Na)NbO_3$-Based Lead-Free Ceramics [J]. Advanced materials, 2018, 30(8): 1705171-9.

[26] Li F, Zhai J, Shen B, et al. Influence of structural evolution on energy storage properties in $Bi_{0.5}Na_{0.5}TiO_3$-$SrTiO_3$-$NaNbO_3$ lead-free ferroelectric ceramics [J]. Journal of Applied Physics, 2017, 121(5): 054103-12.

[27] Gao J, Xu Z, Li F, et al. The hydrostatic pressure dependence of the piezoelectric properties for the barium titanate and lead titanate crystals: Thermodynamic analysis [J]. Journal of Applied Physics, 2011, 109(11): 114111-7.

[28] Li F, Lin D, Chen Z, et al. Ultrahigh piezoelectricity in ferroelectric ceramics by design [J]. Nature materials, 2018, 17(4): 349-54.

[29] Chandrasekaran A, Damjanovic D, Setter N, et al. Defect ordering and defect-domain-wall interactions in $PbTiO_3$: A first-principles study [J]. Physical Review B, 2013, 88(21): 214116.

[30] Lv J, Lou X, Wu J. Defect dipole-induced poling characteristics and ferroelectricity of quenched bismuth ferrite-based ceramics [J]. Journal Materials Chemistry C, 2016, 4(25): 6140-51.

[31] Zhang L, Ren X. Aging behavior in single-domain Mn-doped $BaTiO_3$ crystals: Implication for a unified microscopic explanation of ferroelectric aging [J]. Physical Review B, 2006, 73(9): 094121-26.

[32] Pereira M P A G, Gomes M J M Effect of Nb doping on the microstructural and electrical properties of the PZT ceramics [J]. Journal of the European Ceramic Society, 2001, 21(10-11): 1353-6.

[33] Hammer M H M J. Detailed X-ray Diffraction Analyses and Correlation of Microstructural and Electromechanical Properties of La-doped PZT Ceramics [J]. Journal of Electroceramics, 1998, 2(2): 75-84.

[34] Pramila C G T C, Pillai P K C. Piezoelectric, pyroelectric and dielectric properties of La- and Sm-doped PZT ceramics [J]. Journal of Materials Science Letters, 1993, 12(21): 1657-8.

[35] Y C S, Y C T, T T I. Effects of Sintering Temperature on the Dielectric and Piezoelectric Properties of Nb-Doped PZT Ceramics and Their Applications [J]. Integrated Ferroelectrics, 2010, 58(1): 1293-303.

[36] Robels U, Arlt G. Domain wall clamping in ferroelectrics by orientation of defects [J]. Journal of Applied Physics, 1993, 73(7): 3454-60.

[37] Garc á J E, P érez R, Ochoa D A, et al. Evaluation of domain wall motion in lead zirconate titanate ceramics by nonlinear response measurements [J]. Journal of Applied Physics, 2008, 103(5): 054108.

[38] Ren X. Large electric-field-induced strain in ferroelectric crystals by point-defect-mediated reversible domain switching [J]. Nature materials, 2004, 3(2): 91-4.

[39] Warren W L, Pike G E, Vanheusden K, et al. Defect-dipole alignment and tetragonal strain in ferroelectrics [J]. Journal of Applied Physics, 1996, 79(12): 9250-7.

[40] Keeble D J, Loyo-Menoyo M, Booq Z I Y, et al. Fe^{3+}defect dipole centers in ferroelectric $PbTiO_3$ studied using electron paramagnetic resonance [J]. Physical Review B, 2009, 80(1): 014101.

[41] Gao Y, Uchino K, Viehland D. Effects of thermal and electrical histories on hard piezoelectrics: A comparison of internal dipolar fields and external dc bias [J]. Journal of Applied Physics, 2007, 101(5): 054109.

[42] Takahashi S. Effects of impurity doping in lead zirconate-titanate ceramics [J]. Ferroelectrics, 2011, 41(1): 143-56.

[43] Zhang L, Liu W, Chen W, et al. Mn dopant on the “domain stabilization” effect of aged $BaTiO_3$ and $PbTiO_3$-based piezoelectrics [J]. Applied Physics Letters, 2012, 101(24): 242903-7.

[44] Zeng J, Zhao K, Shi X, et al. Large strain induced by the alignment of defect dipoles in (Bi^{3+},Fe^{3+}) co-doped Pb(Zr,Ti)O_3 ceramics [J]. Scripta Materialia, 2018, 142(0): 20-2.

[45] Gao Y, Kenji. U, Dwight V. Effects of thermal and electrical histories on hard piezoelectrics: A comparison of internal dipolar fields and external dc bias [J]. Journal of Applied Physics, 2007, 101(5): 054109-14.

[46] Setter N, Cross L E. The role of B-site cation disorder in diffuse phase transition behavior of perovskite ferroelectrics [J]. Journal of Applied Physics, 1980, 51(8): 4356-60.

[47] Uchino K, Nomura S. Critical exponents of the dielectric constants in diffused-phase-transition crystals [J]. Ferroelectrics, 2011, 44(1): 55-61.

[48] Li F, Zhang S, Damjanovic D, et al. Local Structural Heterogeneity and Electromechanical Responses of Ferroelectrics: Learning from Relaxor Ferroelectrics [J]. Advanced Functional Materials, 2018, 28(37): 1801504.

[49] Samara G A. The relaxational properties of compositionally disordered ABO_3 perovskites [J]. Journal of Physics: Condensed Matter, 15(R367-R411.

[50] Bokov A A, Ye Z G. Recent Progress in Relaxor Ferroelectrics With Perovskite Structure [J]. Journal of Materials Science, 2006, 41(0): 31-52.

[51] Srivastava N, Weng G J. A dual-phase homogenization theory for the hysteresis and butterfly-shaped behavior of ferroelectric single crystals [J]. Mechanics of Materials, 2006, 38(8-10): 945-57.

[52] Wang K, Yao F Z, Jo W, et al. Temperature-Insensitive (K,Na)NbO_3-Based Lead-Free Piezoactuator Ceramics [J]. Advanced Functional Materials, 2013, 23(33): 4079-86.

[53] Uchino K, Nomura S, Cross L E, et al. Electrostrictive effect in lead magnesium niobate single crystals [J]. Journal of Applied Physics, 1980, 51(2): 1142-5.

[54] K U. Ferroelectric Devices [M]. New York: Marcel Dekker, 2000.

[55] Li P, Liu B, Shen B, et al. Mechanism of significantly enhanced piezoelectric performance and stability in textured potassium-sodium niobate piezoelectric ceramics [J]. Journal of the European Ceramic Society, 2018, 38(1): 75-83.

[56] Zhen Y H, Li J F. Abnormal grain growth and new core-shell structure in (K,Na)NbO_3-based lead-free piezoelectric ceramics [J]. Journal of the American Ceramic Society, 2007, 90(11): 3496-502.

[57] Matsuzawa S, Mase S. Method for producing a single crystal of ferrite [M]. Google Patents. 1982.

[58] Brandon D, Chen D, Chan H. Control of texture in monolithic alumina [J]. Materials Science and Engineering: A, 1995, 195(0): 189-96.

[59] Messing G L, Suvaci E. Method for fabricating textured ceramics [M]. Google Patents. 2001.

[60] Harmer M P, Chan H M, Gorzkowski E P, et al. LEHIGH UNIV BETHLEHEM PA: DTIC Document, 2003.

[61] Seno Y, Tani T. TEM observation of a reactive template for textured $Bi_{0.5}(Na_{0.87}K_{0.13})_{0.5}TiO_3$ polycrystals [J]. Ferroelectrics, 1999, 224(1): 365-72.

[62] Takeuchi T, Tani T, Saito Y. Unidirectionally textured $CaBi_4Ti_4O_{15}$ ceramics by the reactive templated grain growth with an extrusion [J]. Japanese Journal of Applied Physics, 2000, 39(9S): 5577.

[63] Takenaka T, Sakata K. Grain orientation effects on electrical properties of bismuth layer-structured ferroelectric $Pb_{(1-x)}(NaCe)_{x/2}Bi_4Ti_4O_{15}$ solid solution [J]. Journal of applied physics, 1984, 55(4): 1092-9.

[64] Saito Y, Takao H, Tani T, et al. Lead-free piezoceramics [J]. Nature, 2004, 432(7013): 84-7.

[65] Yan Y, Cho K-H, Priya S. Piezoelectric properties and temperature stability of Mn-doped $Pb(Mg_{1/3}Nb_{2/3})$-$PbZrO_3$-$PbTiO_3$ textured ceramics [J]. Applied Physics Letters, 2012, 100(13): 132908.

[66] Yan Y, Wang Y U, Priya S. Electromechanical behavior of [001]-textured $Pb(Mg_{1/3}Nb_{2/3})O_3$-$PbTiO_3$ ceramics [J]. Applied Physics Letters, 2012, 100(19): 192905.

[67] Kržmanc M M, Jančar B, Uršič H, et al. Tailoring the Shape, Size, Crystal Structure, and Preferential Growth Orientation of $BaTiO_3$ Plates Synthesized through a Topochemical Conversion Process [J]. Crystal Growth & Design, 2017, 17(6): 3210-20.

[68] Su S, Zuo R, Lv D, et al. Synthesis and characterization of (001) oriented $BaTiO_3$ platelets through a topochemical conversion [J]. Powder Technology, 2012, 217(0): 11-5.

[69] Poterala S F, Chang Y, Clark T, et al. Mechanistic Interpretation of the Aurivillius to Perovskite Topochemical Microcrystal Conversion Process [J]. Chemistry of Materials, 2010, 22(6): 2061-8.

[70] Chen W, Kinemuchi Y, Watari K, et al. Grain-Oriented $Bi_4Ti_3O_{12}$ Ferroelectric Ceramics Prepared by Magnetic Alignment [J]. Journal of the American Ceramic Society, 2006, 89(2): 490-3.

[71] Kimura T, Takahashi T, Tani T, et al. Preparation of crystallographically textured $Bi_{0.5}Na_{0.5}TiO_3$–$BaTiO_3$ ceramics by reactive-templated grain growth method [J]. Ceramics International, 2004, 30(7): 1161-7.

[72] Cao Z, Sassa K, Asai S. The orientation mechanism of $(Ca,Sr)Bi_4Ti_4O_{15}$ ceramics prepared by slip casting in high magnetic field and subsequent sintering [J]. Journal of the European Ceramic Society, 2007, 27(7): 2591-6.

[73] Zeng J T, Kwok K W, Tam W K, et al. Plate-Like $Na_{0.5}Bi_{0.5}TiO_3$ Template Synthesized by a Topochemical Method [J]. Journal of the American Ceramic Society, 2006, 89(12): 3850-3.

[74] Huang Q-W, Xu J, Zhu L-H, et al. Molten Salt Synthesis of Acicular $Ba_2NaNb_5O_{15}$ Seed Crystals [J]. Journal of the American Ceramic Society, 2005, 88(2): 447-9.

[75] Maurya D, Zhou Y, Yan Y, et al. Synthesis mechanism of grain-oriented lead-free piezoelectric $Na_{0.5}Bi_{0.5}TiO_3$–$BaTiO_3$ ceramics with giant piezoelectric response [J]. Journal of Materials Chemistry C, 2013, 1(11): 2102.

[76] Zhou Y, Zhao W, Ruan W, et al. Abnormal electric-field-induced light scattering in $Pb(Mg_{1/3}Nb_{2/3})O_3$-$PbTiO_3$ transparent ceramics [J]. Applied Physics Letters, 2015, 106(12): 122904.

[77] Zhang M H, Wang K, Du Y J, et al. High and Temperature-Insensitive Piezoelectric Strain in Alkali Niobate Lead-free Perovskite [J]. Journal of the American Chemical Society, 2017, 139(10): 3889-95.

[78] Wang X, Wu J, Xiao D, et al. Giant piezoelectricity in potassium-sodium niobate lead-free ceramics [J]. Journal of the American Chemical Society, 2014, 136(7): 2905-10.

[79] Maurya D, Zhou Y, Wang Y, et al. Giant strain with ultra-low hysteresis and high temperature stability in grain oriented lead-free $K_{0.5}Bi_{0.5}TiO_3$-$BaTiO_3$-$Na_{0.5}Bi_{0.5}TiO_3$ piezoelectric materials: supplementary information [J]. Scientific Reports, 2015, 5(0): 8595.

[80] Team N: Annual report: Introduction to Mossbauer Spectroscopy, Royal Society of Chemistry,Thomas Graham House, Science Park, Milton Road, Cambridge, 2014.

[81] Cross E. Materials science: Lead-free at last [J]. Nature, 2004, 432(7013): 24-5.

[82] Kalem V, Cam I, Timu çin M. Dielectric and piezoelectric properties of PZT ceramics doped with strontium and lanthanum [J]. Ceramics International, 2011, 37(4): 1265-75.

[83] Boni A G, Pintilie I, Pintilie L, et al. Electronic transport in (La,Sr)MnO_3-ferroelectric-(La,Sr)MnO_3 epitaxial structures [J]. Journal of Applied Physics, 2013, 113(22): 224103.

[84] Kalem V, Timucin M. Structural, piezoelectric and dielectric properties of PSLZT–PMnN ceramics [J]. Journal of the European Ceramic Society, 2013, 33(1): 105-11.

[85] Durruthy-Rodr íguez M D, Costa-Marrero J, Hern ández-Garc á M, et al. Photoluminescence in “hard” and “soft” ferroelectric ceramics [J]. Applied Physics A, 2010, 98(3): 543-50.

[86] Jakes P, Erdem E, Eichel R d-A, et al. Position of defects with respect to domain walls in Fe^{3+}-doped $Pb[Zr_{0.52}Ti_{0.48}]O_3$ piezoelectric ceramics [J]. Applied Physics Letters, 2011, 98(7): 072907.

[87] Ramam K, Lopez M. Microstructure, dielectric and electromechanical properties of PLSZFT nanoceramics for piezoelectric applications [J]. Journal of Materials Science: Materials Electron, 2008, 19(0): 1140-5.

[88] Ramam K, Bell A J, Bowen C R, et al. Investigation of dielectric and piezoelectric properties of niobium-modified PLSZFT nanoceramics for sensor and actuator applications [J]. Journal of Alloys and Compounds, 2009, 473(1-2): 330-5.

[89] Cao Z, Li G, Zeng J, et al. Improving the piezoelectric thermal stability by tailoring phase transition behavior in the new $(1-x)[0.65PbMg_{1/3}Nb_{2/3}O_3–0.35PbTiO_3]–xBiZn_{1/2}Ti_{1/2}O_3$ perovskite solid solutions [J]. Journal of Alloys and Compounds, 2011, 509(36): 8907-11.

[90] Kalyani A K, Garg R, Ranjan R. Competing A-site and B-site driven ferroelectric

instabilities in the (1−x)$PbTiO_3$-x$BiAlO_3$ system [J]. Applied Physics Letters, 2009, 94(20): 202903.

[91] Noheda B, Cox D, Shirane G, et al. A monoclinic ferroelectric phase in the $Pb(Zr_{1-x}Ti_x)O_3$ solid solution [J]. Applied physics letters, 1999, 74(14): 2059-61.

[92] Jaffe B. Piezoelectric ceramics [M]. Elsevier, 2012.

[93] Ciuchi I V, Craciun F, Mitoseriu L, et al. Preparation and properties of La doped PZT 90/10 ceramics across the ferroelectric–antiferroelectric phase boundary [J]. Journal of Alloys and Compounds, 2015, 646(0): 16-22.

[94] Kamel T M, de With G. Poling of hard ferroelectric PZT ceramics [J]. Journal of the European Ceramic Society, 2008, 28(9): 1827-38.

[95] Takagi K, Kikuchi S, Li J F, et al. Ferroelectric and Photostrictive Properties of Fine-Grained PLZT Ceramics Derived from Mechanical Alloying [J]. Journal of the American Ceramic Society, 2004, 87(8): 1477-82.

[96] James A, Subrahmanyam J, Yadav K. Structural and electrical properties of nanocrystalline PLZT ceramics synthesized via mechanochemical processing [J]. Journal of Physics D: Applied Physics, 2006, 39(10): 2259.

[97] Zhu F, Qiu J, Ji H, et al. Comparative investigations on dielectric, piezoelectric properties and humidity resistance of PZT-SKN and PZT-SNN ceramics [J]. Journal of Materials Science-Materials in Electronics, 2015, 26(5): 2897-904.

[98] Tsurumi T, Kumano Y, Ohashi N, et al. 90 °domain reorientation and electric-field-induced strain of tetragonal lead zirconate titanate ceramics [J]. Japanese journal of applied physics, 1997, 36(9S): 5970.

[99] Eichel R A, Kungl H, Jakes P. Defect structure of non-stoichiometric and aliovalently doped perovskite oxides [J]. Materials Technology, 2013, 28(5): 241-6.

[100] Genenko Y A. Space-charge mechanism of aging in ferroelectrics: An analytically solvable two-dimensional model [J]. Physical Review B, 2008, 78(21): 214103.

[101] Pöykkö S, Chadi D J. Dipolar Defect Model for Fatigue in Ferroelectric Perovskite [J]. Physical review letters, 1999, 83(6): 1231-4.

[102] Xu K, Li J, Lv X, et al. Superior Piezoelectric Properties in Potassium–Sodium Niobate Lead-Free Ceramics [J]. Advanced materials, 2016, 28(38): 8519-23.

[103] Ganguly M, Rout S K, Sinha T P, et al. Characterization and Rietveld Refinement of A-site deficient Lanthanum doped Barium Titanate [J]. Journal of Alloys and Compounds, 2013, 579(0): 473-84.

[104] Dercz J, Starczewska A, Dercz G. Dielectric and Structural Properties of $Bi_5Ti_3FeO_{15}$ Ceramics Obtained by Solid-State Reaction Process from Mechanically Activated Precursors [J]. International Journal of Thermophysics, 2011, 32(4): 746-61.

[105] Jin L, Huo R, Guo R, et al. Diffuse Phase Transitions and Giant Electrostrictive Coefficients in Lead-Free Fe^{3+}-Doped $0.5Ba(Zr_{0.2}Ti_{0.8})O_3$-$0.5(Ba_{0.7}Ca_{0.3})TiO_3$

Ferroelectric Ceramics [J]. ACS Applied Materials & Interfaces, 2016, 8(45): 31109-19.

[106] Zhang S-T, Yang B, Cao W. The temperature-dependent electrical properties of $Bi_{0.5}Na_{0.5}TiO_3$–$BaTiO_3$–$Bi_{0.5}K_{0.5}TiO_3$ near the morphotropic phase boundary [J]. Acta Materialia, 2012, 60(2): 469-75.

[107] Kim J S, Cheon C I, Lee C H, et al. Weak ferromagnetism in the ferroelectric $BiFeO_3$–$ReFeO_3$–$BaTiO_3$ solid solutions (Re = Dy,La) [J]. Journal of Applied Physics, 2004, 96(1): 468-74.

[108] Zheng T, Ding Y, Wu J. Bi nonstoichiometry and composition engineering in $(1-x)Bi_{1+y}FeO_{3+3y/2}-xBaTiO_3$ ceramics [J]. RSC Adv, 2016, 6(93): 90831-9.

[109] Zheng T, Jiang Z, Wu J. Enhanced piezoelectricity in (1-x)$Bi_{1.05}Fe_{1-y}AyO_3$-x$BaTiO_3$ lead-free ceramics: site engineering and wide phase boundary region [J]. Dalton transactions, 2016, 45(28): 11277-85.

[110] Wang D, Khesro A, Murakami S, et al. Temperature dependent, large electromechanical strain in Nd-doped $BiFeO_3$-$BaTiO_3$ lead-free ceramics [J]. Journal of the European Ceramic Society, 2017, 37(4): 1857-60.

[111] Shimizu H, Kobayashi K, Mizuno Y, et al. Advantages of Low Partial Pressure of Oxygen Processing of Alkali Niobate: $NaNbO_3$ [J]. Journal of the American Ceramic Society, 2014, 97(6): 1791-6.

[112] Lee S Y, Ahn C W, Kim J S, et al. Enhanced piezoelectric properties of Ta substituted-$(K_{0.5}Na_{0.5})NbO_3$ films: A candidate for lead-free piezoelectric thin films [J]. Journal of Alloys and Compounds, 2011, 509(20): L194-L8.

[113] Gotardo R A M, Viana D S F, Olzon-Dionysio M, et al. Ferroic states and phase coexistence in $BiFeO_3$-$BaTiO_3$ solid solutions [J]. Journal of Applied Physics, 2012, 112(10): 104112.

[114] Zhou C, Yang H, Zhou Q, et al. Dielectric, ferroelectric and piezoelectric properties of La-substituted $BiFeO_3$–$BaTiO_3$ ceramics [J]. Ceramics International, 2013, 39(4): 4307-11.

[115] Azough F, Freer R, Thrall M, et al. Microstructure and properties of Co-, Ni-, Zn-, Nb- and W-modified multiferroic $BiFeO_3$ ceramics [J]. Journal of the European Ceramic Society, 2010, 30(3): 727-36.

[116] Greneche J-M. The contribution of ^{57}Fe Mössbauer spectrometry to investigate magnetic nanomaterials [M]//YOSHIDA Y, LANGOUCHE G. Mössbauer spectrometry. New York; Springer-Verlag New York Dordrecht London Heidelberg. 2013: 187-241.

[117] Escobar Castillo M, Shvartsman V V, Gobeljic D, et al. Effect of particle size on ferroelectric and magnetic properties of $BiFeO_3$ nanopowders [J]. Nanotechnology, 2013, 24(35): 355701.

[118] Calisir I, Amirov A A, Kleppe A K, et al. Optimisation of functional properties in lead-free $BiFeO_3$–$BaTiO_3$ ceramics through La^{3+} substitution strategy [J]. Journal of Materials Chemistry A, 2018, 6(13): 5378-97.

[119] Gao S, Yao Z, Ning L, et al. Enhanced Bipolar Strain Response in Lithium/Niobium

Co-Doped Sodium-Barium Bismuth Titanate Lead-Free Ceramics [J]. Advanced Engineering Materials, 2017, 19(11): 1700125.

[120] Tirupathi P, Kumar N, Pastor M, et al. Diffused phase transitions in $Pb(Zr_{0.65}Ti_{0.35})O_3$-$Pb(Fe_{2/3}W_{1/3})O_3$ multiferroics [J]. Journal of Applied Physics, 2015, 117(7): 074105.

[121] Ihlefeld J F, Harris D T, Keech R, et al. Scaling Effects in Perovskite Ferroelectrics: Fundamental Limits and Process-Structure-Property Relations [J]. Journal of the American Ceramic Society, 2016, 99(8): 2537-57.

[122] Amorín H, Jiménez R, Deluca M, et al. Nanostructuring Effects in Piezoelectric $BiScO_3$-$PbTiO_3$ Ceramics [J]. Journal of the American Ceramic Society, 2014, 97(9): 2802-9.

[123] Nobre M A L, Lanfredi S. Ferroelectric state analysis in grain boundary of $Na_{0.85}Li_{0.15}NbO_3$ ceramic [J]. Journal of Applied Physics, 2003, 93(9): 5557-62.

[124] Liu Y, Chang Y, Li F, et al. Exceptionally High Piezoelectric Coefficient and Low Strain Hysteresis in Grain-Oriented (Ba, Ca)(Ti, Zr)O_3 through Integrating Crystallographic Texture and Domain Engineering [J]. ACS Applied Materials & Interfaces, 2017, 9(35): 29863-71.

[125] Fujii I, Mitsui R, Nakashima K, et al. Effect of sintering condition and V-doping on the piezoelectric properties of $BaTiO_3$-$Bi(Mg_{1/2}Ti_{1/2})O_3$-$BiFeO_3$ ceramics [J]. Journal of the Ceramic Society of Japan, 2013, 121(1416): 589-92.

[126] Xu Y, Liu D W, Lai F P, et al. Fabrication of (K,Na)NbO_3 lead-free piezoceramic microrod arrays by sol-gel processing with micromachined silicon templates [J]. Journal of the American Ceramic Society, 2008, 91(9): 2844-7.

[127] Huan Y, Wang X H, Li L T. Low-Temperature Sintering and Enhanced Piezoelectric Properties in KNN-LTS Nanopowder Prepared via a Low-Cost Water-Based Sol-Gel Method [M]//PAN W, GONG J. High-Performance Ceramics Viii. Trans Tech Publications Ltd. 2014: 795-9.

[128] Yu Q, Li J F, Chen Y N, et al. Effect of Pyrolysis Temperature on Sol-Gel Synthesis of Lead-free Piezoelectric (K,Na)NbO_3 Films on Nb:$SrTiO_3$ Substrates [J]. Journal of the American Ceramic Society, 2014, 97(1): 107-13.

[129] Wang K, Zhang B P, Li J F, et al. $Na_{1-x}K_xNbO_3$ (x = 0.2 similar to 0.8) lead-free piezoelectric ceramics prepared by spark plasma sintering [M]//PAN W, GONG J H. High-Performance Ceramics IV, Pts 1-3. 2007: 224-7.

[130] Shen Z Y, Li J F, Wang K, et al. Electrical and Mechanical Properties of Fine-Grained Li/Ta-Modified (Na,K)NbO_3-Based Piezoceramics Prepared by Spark Plasma Sintering [J]. Journal of the American Ceramic Society, 2010, 93(5): 1378-83.

[131] Zhen Y H, Li J F, Wang K, et al. Spark plasma sintering of Li/Ta-modified (K,Na)NbO_3 lead-free piezoelectric ceramics: Post-annealing temperature effect on phase structure,

electrical properties and grain growth behavior [J]. Materials Science and Engineering B-Advanced Functional Solid-State Materials, 2011, 176(14): 1110-4.

[132] Ji L, Du X, Zhao Y, et al. Physical Properties and Structure Characteristics of Laser Prepared $(Na_{0.5}K_{0.5})NbO_3$-$LiNbO_3$ Ceramics [J]. Ferroelectrics, 2010, 400(1): 104-12.

[133] Tian X, Dittmar A, Melcher J, et al. Sinterability studies on $K_{0.5}Na_{0.5}NbO_3$ using laser as energy source [J]. Applied Surface Science, 2010, 256(20): 5918-23.

[134] Meng W Q, Zuo R Z, Su S, et al. Two-step sintering and electrical properties of sol-gel derived $0.94(Bi_{0.5}Na_{0.5})TiO_3$-$0.06BaTiO_3$ lead-free ceramics [J]. Journal of Materials Science-Materials in Electronics, 2011, 22(12): 1841-7.

[135] Li Y, Dai Y J, Wang H Q, et al. Microstructures and electrical properties of $KNbO_3$ doped (Li,Ta,Sb) modified $(K,Na)NbO_3$ lead-free ceramics by two-step sintering [J]. Materials Letters, 2012, 89(0): 70-3.

[136] Gao R L, Chu X C, Huan Y, et al. $(K,Na)NbO_3$ based piezoceramics prepared by a two-step calcining and ball milling route [J]. Materials Letters, 2014, 123(0): 242-5.

[137] Wei N, Wang J, Li B, et al. Improvement of the piezoelectric and ferroelectric properties of $(K,Na)_{0.5}NbO_3$ ceramics via two-step calcination-milling route [J]. Ceramics International, 2015, 41(8): 9555-9.

[138] Hu G, Xu B, Yan X, et al. Fabrication and electrical properties of textured $Ba(Zr_{0.2}Ti_{0.8})O_3$–$(Ba_{0.7}Ca_{0.3})TiO_3$ ceramics using plate-like $BaTiO_3$ particles as templates [J]. Journal of Materials Science: Materials in Electronics, 2014, 25(4): 1817-27.

[139] Messing G L, Sabolsky E M, Kwon S, et al. Templated Grain Growth of Textured Piezoelectric Ceramics [J]. Key Engineering Materials, 2002, 206(0): 1293-6.

[140] Rafiq M A, Costa M E, Vilarinho P M. Pairing High Piezoelectric Coefficients, d_{33}, with High Curie Temperature (T_C) in Lead-Free $(K,Na)NbO_3$ [J]. ACS Applied Materials & Interfaces, 2016, 8(49): 33755-64.

[141] Ye S K, Fuh J Y H, Lu L. Structure and electrical properties of 〈001〉 textured $(Ba_{0.85}Ca_{0.15})(Ti_{0.9}Zr_{0.1})O_3$ lead-free piezoelectric ceramics [J]. Applied Physics Letters, 2012, 100(25): 252906.

[142] Peng J, Zeng J, Zheng L, et al. The interplay of phases, structural disorder and dielectric behavior in Al doped $BiFeO_3$-$BaTiO_3$ ceramics [J]. Journal of Alloys and Compounds, 2019, 796(0): 221-8.

[143] Chen J, Xing X, Deng J, et al. Thermal expansions of ceramics in the system $Pb_{1-x}(La_{1/2}K_{1/2})_xTiO_3$ [J]. Journal of Alloys and Compounds, 2004, 372(1-2): 259-66.

[144] Cheng G F, Ruan Y J, Liu W, et al. Effect of temperature on structural expansion for $Bi_{0.8-x}Pr_xBa_{0.2}FeO_3$ ($x \leq 0.1$) ceramics [J]. Thermochimica Acta, 2015, 602(0): 74-7.

[145] Yao M, Li Q, Li F, et al. Leakage current and breakdown behavior of bismuth-doped amorphous strontium titanate thin film [J]. Materials Chemistry and Physics, 2018, 206(0): 48-55.

[146] Kwon S, Sabolsky E M, Messing G L, et al. High Strain, <001> Textured $0.675Pb(Mg_{1/3}Nb_{2/3})O_3$-$0.325PbTiO_3$ Ceramics: Templated Grain Growth and Piezoelectric Properties [J]. Journal of the American Ceramic Society, 2005, 88(2): 312-7.

[147] Aschauer U, Pfenninger R, Selbach S M, et al. Strain-controlled oxygen vacancy formation and ordering in $CaMnO_3$ [J]. Physical Review B, 2013, 88(5): 054111.

[148] Liu H R, Li Q, Li Y Y, et al. Structure Evolution and Electrical Properties of Y^{3+}-Doped $Ba_{1-x}Ca_xZr_{0.07}Ti_{0.93}O_3$ Ceramics [J]. Journal of the American Ceramic Society, 2014, 97(7): 2076-81.

[149] Cheon C I, Choi J H, Kim J S, et al. Role of $(Bi_{1/2}K_{1/2})TiO_3$ in the dielectric relaxations of $BiFeO_3$-$(Bi_{1/2}K_{1/2})TiO_3$ ceramics [J]. Journal of Applied Physics, 2016, 119(15): 154101.

List of Figures

List of Tables